Uniwersytet Jagielloński
Wydział Fizyki Astronomii i Informatyki Stosowanej
Instytut Fizyki

Cold quantum gases in optical lattices

Autor:
mgr Mateusz Łącki

Supervisor:
prof. dr hab. Jakub Zakrzewski

Referees:
prof. dr hab. Jacek Dziarmaga
prof. dr hab. Marek Trippenbach

A thesis submitted for the degree of Doctor of Philosophy

Kraków, 2014

Contents

Thesis is based on the results published in the following works.

1. Mateusz Łącki, Simone Paganelli, Veronica Ahufinger, Anna Sanpera, Jakub Zakrzewski, *Disordered spinor Bose-Hubbard model*, Phys. Rev. A **83**, 013605, (2011).

2. Simone Paganelli, Mateusz Łącki, Veronica Ahufinger, Jakub Zakrzewski, Anna Sanpera, *Spin effects in Bose-Glass phases*, Journal of Low Temperature Physics 165, 5-6, 227-238, (2011).

3. Mateusz Łącki, Dominique Delande, Jakub Zakrzewski, *Extracting information from non adiabatic dynamics: excited symmetric states of the Bose-Hubbard model*, Acta Physica Polonica A 12A/2011, (2012).

4. Mateusz Łącki, Dominique Delande, Jakub Zakrzewski, *Numerical computation of dynamically important excited states of many-body systems*, Phys. Rev. A 86, 013602, (2012).

5. Mateusz Łącki, Dominique Delande, Jakub Zakrzewski, *Dynamics of cold bosons in optical lattices: effects of higher Bloch bands*, New Journal of Physics 15, 013062, (2013).

6. Mateusz Łącki, Jakub Zakrzewski, *Fast Dynamics for Atoms in Optical Lattices*, Phys. Rev. Lett. 110, 065301, (2013).

7. Mateusz Łącki , Bogdan Damski, Jakub Zakrzewski, *Numerical studies of ground state fidelity of the Bose-Hubbard model*, Phys. Rev. A 89, 033625, (2014).

List of key symbols

$\mathcal{H}_{BH}, \mathcal{H}_{MBH}, \mathcal{H}_X$	many-body Hamiltonians: Bose-Hubbard, Multiband Bose-Hubbard, position space second quantized Hamiltonian for gas of ultracold atoms
$\mathcal{H}_{tun}$	tunnelling part of Bose-Hubbard or Multiband Bose-Hubbard Hamiltonian
$\mathcal{H}_{loc}$	single site part of Bose-Hubbard or Multiband Bose-Hubbard Hamiltonian (atomic limit)
V_{int}	interaction potential of pair of atoms
V_{latt}	optical lattice 3D potential atoms
V_{trap}	external trapping potential
L	linear size of a finite lattice
N	total number of particles in the lattice
g	contact interaction coupling constant in position representation
E_i^α	single particle energy of atom in Wannier function mode localised in site i and band α
J_d^α	tunnelling coupling constant in the Multiband Bose-Hubbard model (within band α) for d-site long particle jump)
$U_{ijkl}^{\alpha\beta\gamma\delta}$	interaction coupling constant in the Multiband Bose-Hubbard model
μ	chemical potential
E_R	Energy recoil unit
F	Fidelity function (2.1)
χ	Fidelity susceptibility defined in Eq. (2.1) or the bond dimension in the MPS representation Eq. (1.20)
$U(t_2, t_1)$	evolution operator from time t_1 to t_2, for time-independent Hamiltonian $U(t_2, t_1) = U(t_2 - t_1)$
BEC	Bose-Einstein Condnsate
BG	Bose-Glass
BH	Bose-Hubbard (model)
DMRG	Density Matrix Renormalization Group
MBH	Multiband Bose-Hubbard (model)
LDA	Local Density Approximation
METTS	Minimally Entangled Typical Thermal States (see Chapter 7)

MI	Mott Insulator
MPS, MPS_χ	Matrix Product States, MPS with bond dimension χ
OBC	Open Boundary Conditions
PBC	Periodic Boundary Conditions
QMC	Quantum Monte Carlo
QPT	Quantum Phase Transition
SF	Superfluid
TEBD	Time-Evolving Block Decimation
tDMRG	real time Density Matrix Renormalization Group algorithm

Chapter 1

Introduction

This thesis is concerned with developing and using theoretical tools and numerical methods to describe physics of many body quantum systems formed by ultracold atoms in optical lattice potentials. This chapter gives motivation for the use of ultracold atoms to study physics of quantum complex systems, discusses basic setting, major achievements of the field especially relevant to the content of this thesis. It also introduces most important theoretical tools that are strongly used in the subsequent chapters. Tools that are necessary to obtain the results but in-depth analysis of their construction is not vital have been presented in Appendices.

1.1 Ultracold atoms

Physics of ultracold atoms [1–4] experiences at least 20 years of spectacular progress. Doubtlessly the milestone achievement was the realisation of Bose-Einstein condensation [5, 6] which was possible by steady progress in trapping and cooling techniques. Adding external periodic potential of so-called optical lattice, enabled implementing models developed in last 50 years in the field of condensed matter physics. This is particularly spectacular in the field of strongly-correlated electronic models such as quantum magnetism models or Hubbard model for electrons in the solid. Using the experimental realizations of lattice models, an analogue of metal-insulator phase transition, a Mott-Insulator Superfluid phase transition of Bose-Hubbard model was observed [7]. Since then ultracold atoms have become a setting for parallel experimental and theoretical research for example, but not limited to, in the field of disordered systems [8–11], gases with internal spin structure [12–16], thermalisation and non-equilibrium dynamics [17–19], topological order and fractional quantum Hall effects [20, 21], artificial gauge fields [22].

1.1.1 Ultracold, experimental setup

The term "temperature of a gas" is described by the average kinetic energy of the atoms in the equilibrium state. Achieving experimentally low temperatures posed an experimental challenge as soon as scientists realized that matter can not be arbitrarily cold. This realization was due to constant volume air-thermometers in which gas pressure was directly proportional to the temperature. In the 19th century a field of cryogenic was born, technological and theoretical progress in field of thermodynamics allowed for liquefaction of oxygen (Cailletet, 1877 [23]), hydrogen (Dewar, 1898 [24]), helium (Kamerlingh Onnes, 1908 [25]). Achieving ultracold temperatures was a key to the discovery of superfluidity in 1937 by cooling helium-4 to temperature of 2.2 K [26]. Post-war low temperature research saw two important breakthroughs: experimental realization of laser-cooling [27] and evaporative cooling. In laser cooling moving atoms are subjected to two counter propagating lass beams. The atoms absorb photons which forces them to lower their speed in the laboratory frame of reference, as net momentum transfer is opposite to the atom's velocity due to the Doppler effect. For alkali atoms, finite energy level widths limit this technique to cooling the gas at most 300 mK. The evaporative cooling, used on a initially laser-cooled sample, works by removing from the atom sample those atoms which have the highest kinetic energy and allowing for rethermalization of the remainder of sample in lowest temperature. In the end as many as 1% of the original number of atoms is kept. This approach enabled to achieve atomic density high enough and temperatures of tens of nanokelvins low enough and to observe experimentally Bose-Einstein condensation of atoms in 1995 [5, 6, 28].

1.1.2 Interaction of an atom with an EM field

An atom in the oscillating electric field is described by the Hamiltonian [29, 30]:

$$H = \frac{p^2}{2m} + V + e\mathcal{E}_z z \cos \omega t. \tag{1.1}$$

Looking for solutions one uses an ansatz:

$$\psi(t) = \exp(i/\hbar\epsilon t)\psi_\epsilon(t), \tag{1.2}$$

with ψ_ϵ — $\frac{2\pi}{\omega}$ -periodic function. From the time-dependent Schrödingier equation, one obtains an equation:

$$(H - i\hbar\partial_t)\psi_\epsilon = \epsilon\psi_\epsilon, \tag{1.3}$$

which may be considered a time-independent Schrödingier equation in extended space: $S = \mathbb{R}^3 \times [0, T]$. The value ϵ is called a *quasi energy*. Multiplying the state ψ_ϵ by $\exp(i\omega t)$, one may shift the quasi energy of ψ_ϵ by

$\hbar\omega$, and preserve the ansatz form (1.2). To solve the time-dependent problem in (1.1) one starts with time independent solution for $\mathcal{E}_z = 0$, which clearly satisfies (1.2) and applies the time-independent perturbation theory for states defined over the extended domain S. The lowest energy correction comes from a second order term of the perturbation expansion:

$$\Delta E = (e\mathcal{E}_z)^2 \sum_{E_{m,k} \neq E_n} \frac{\langle \psi_0 | z \cos \omega t | \psi_m, k \rangle}{E_n - E_m - k\omega\hbar}. \tag{1.4}$$

Thus the potential felt by the atom is proportional to $\frac{\mathcal{E}_z^2}{E_n - E_m - \hbar\omega}$. To be significant, at least one denominator of (1.4) has to be near-resonant. However, to avoid absorption of the photon and subsequent heating, one may not approach the resonance too closely.

1.2 Many-body Hamiltonian: from a continuous to a discretized model

A Hamiltonian describing the gas of ultracold atoms in the optical lattice potential can be expressed within the second-quantization framework as:

$$\begin{aligned} \mathcal{H}_X &= \int d^3\vec{r}\hat{\psi}^\dagger(\vec{r}) \left(-\frac{\hbar^2}{2m}\nabla^2 + V_{latt.}(\vec{r}) + V_{trap}(\vec{r}) \right) \hat{\psi}(\vec{r}) \\ &+ \int d^3\vec{r} d^3\vec{r}' \hat{\psi}^\dagger(\vec{r})\hat{\psi}^\dagger(\vec{r}') V_{int}(\vec{r} - \vec{r}')\hat{\psi}(\vec{r})\hat{\psi}(\vec{r}') - \int d^3\vec{r}\mu\psi^\dagger(\vec{r})\hat{\psi}(\vec{r}), \end{aligned} \tag{1.5}$$

where V_{int} is atom pair interaction potential. Low density of the gas allows to neglect multiparticle interaction. We will consider only simple cubic lattices for which the lattice potential is just $V_{latt.}(x, y, z) = s_x \cos^2(k_x x) + s_y \cos^2(k_y y) + s_z \cos^2(k_z z)$. In the case of external harmonic confinement, $V_{trap} = \frac{1}{2}m\omega^2(r)^2$. The optical lattice may be made effectively one (or two) dimensional by increasing lattice depth s_y and s_z (or only s_z) so that excited states in that directions become very highly energetic and therefore not achievable by the energy conservation. In the end one gets a family of disconnected systems – either an array of one-dimensional tubes, or a stack of two dimensional pancake-shaped 2D lattices (Figure 1.1) as tunnelling in the transverse directions occurs in timescales much longer than the experiment duration. Let us stress an important difference: atoms in 1D and 2D lattices scatter (for a typical scattering length value negligible compared to the potential well size) according to 3D scattering theory. It is the spatial arrangement of accessible potential well that is linear or planar.

In the absence of long range interactions, in low-energy, dilute regime the s-wave scattering is a dominant way of two particle interaction. In that limit the scattering properties are described by just one parameter — the scattering length a [31]. Description of the scattering may be performed by the

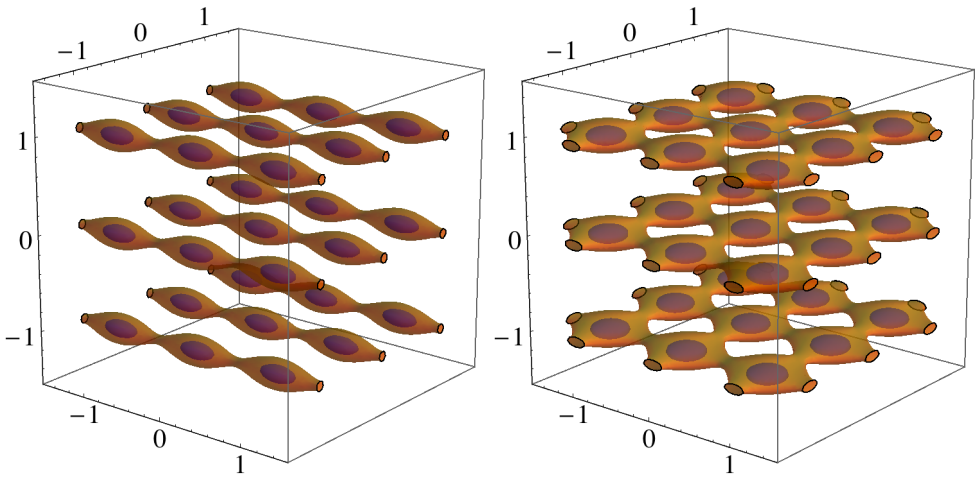

Figure 1.1: Isopotential surfaces for potential $V(x,y,z) = s_x \cos^2(k_x x) + s_y \cos^2(k_y y) + s_z \cos^2(k_z z)$ for model 1D optical lattice situation ($s_z = s_y = 5s_x$) — left panel, and 2D optical lattice ($s_z = 5s_y = s_x$) — right panel. Integer numbers denote integer lattice sites coordinates. Blue surfaces denote value of potential V for energy close to energy minimum, orange surface denote energy above classical tunnelling threshold along main directions of the optical lattice (x for 1D, and x, y for 2D optical lattice).

interaction potential. For mathematically 1D systems the interaction potential V_{int} may be taken as $V_D(x_1 - x_2) = g\delta(x_1 - x_2)$, where $g = \frac{4\pi\hbar a}{m}$. This leads to a correct self-adjoint Hamiltonian. In three dimensional systems however, use of the pure Dirac delta potential leads to unwanted mathematical consequences: the resulting Hamiltonian is not a self-adjoint operator. To amend it one may use the so called Fermi-Huang pseudopotential [32] $V_{HF}(x_1 - x_2) = \delta(x_1 - x_2)\frac{\partial}{\partial|x_1 - x_2|}|x_1 - x_2|$ as V_{int}. With that choice of V_{int} the Hamiltonian (1.5) is self adjoint. Moreover $\langle\psi|V_D|\psi\rangle = \langle\psi|V_{HF}|\psi\rangle$ when $|\psi\rangle$ is any smooth function. Although it is possible to choose an orthonormal basis consisting solely of smooth functions, one may not conclude from this fact that $V_{HF} = V_D$. Indeed, as operators V_D and V_{HF} are not bounded and therefore not continuous. As a result they are not defined uniquely by their values on a orthonormal basis. In fact the domain of the Hamiltonian (1.5) with V_{HF} contains not only smooth functions, but also functions that poses a simple $|x_i - x_j|^{-1}$ as $x_i \to x_j$. These singular functions do not belong to the domain of the kinetic energy operator, but they do belong to the full Hamiltonian domain (with V_{HF} as V_{int}) [33]. These subtleties are related to short range physics (equivalently: large momenta). They are predicted to be relevant for large scattering amplitude and large interaction potential range [34, 35]. Neither of this conditions is satisfied in applications considered in this thesis. It is worth to point out that full systematic, theoretical

description of interparticle interactions for realistic systems encountered in ultracold atoms experiments is still an open problem.

The most common is description of many-body states in terms of discrete lattice modes defined by the lattice potential's Wannier functions. Substituting field operators $\hat{\psi}(x)$ in (1.5) with their Wannier function expansion: $\hat{\psi}(\vec{r}) = \sum_{i,\alpha} W_i^\alpha(\vec{r})\hat{a}_i^\alpha$, where i number lattice sites, and α — enumerates Bloch bands leads to the following, Multiband Bose-Hubbard (MBH) model:

$$\mathcal{H}_{MBH} = \underbrace{-\sum_{i\neq j,\alpha} J_{i-j}^\alpha((a_i^\alpha)^\dagger a_j^\alpha + H.c.) +}_{\mathcal{H}_{tun}}$$
$$\sum_{i,\alpha} E_i^\alpha n_i^\alpha + \underbrace{\frac{1}{2}\sum_{\alpha,\beta,\gamma,\delta}\sum_{ijkl} U_{ijkl}^{\alpha\beta\gamma\delta}(a_i^\alpha)^\dagger(a_j^\beta)^\dagger a_k^\gamma a_l^\delta}_{\mathcal{H}_{int}}, \tag{1.6}$$

here a_i satisfy canonical commutation relations, and are typically interpreted as annihilation operator for a particle at site i. However, particles situated at different sites (in the sense defined by operators a_i^α) do interact, as Wannier functions do poses tails which span over neighboring sites. In the above, the summation is performed over the lattice sites denoted by roman letters i, j, k, l. They are 3-indices (for example $i = (i_x, i_y, i_z)$) that range over $\mathbb{Z}^3$, as the original physical system was defined over $\mathbb{R}^3$.

The parameters $E_i^\alpha, J_{i-j}^\alpha, U_{ijkl}^{\alpha\beta\gamma\delta}$ are defined by:

$$J_{i-j}^\alpha = \int W_i^\alpha(\vec{r})\left(-\frac{\hbar^2}{2m}\nabla^2 + V_{latt.}(\vec{r})\right)W_j^\alpha(\vec{r})\mathrm{d}^3\vec{r}, \quad E_i^\alpha = J_{i-i}^\alpha \tag{1.7}$$

$$U_{ijkl}^{\alpha\beta\gamma\delta} = \int \mathrm{d}^3\vec{r}\mathrm{d}^3\vec{r}' W_i^\alpha(\vec{r})W_j^\beta(\vec{r}')V_{int}(\vec{r}-\vec{r}')W_k^\gamma(\vec{r})W_l^\delta(\vec{r}'), \tag{1.8}$$

where W_i^α are Wanner functions of the lattice. The natural energy unit for this model is a recoil energy unit $E_R = \frac{\hbar^2 k^2}{2m}$, where $k = \frac{2\pi}{\lambda}$.We adopt this unit in this thesis whenever possible. Typically all parameters of the BH (and alike) models are expressed in the recoil energy units.

The summation over index α includes, infinite number of Bloch bands. However, often the considered lattice depth is high. This makes the energy gap between Bloch bands dominate other energy scales appearing in the model. This is an argument for restriction of a multiband model (1.6) just to the first Bloch band. Additionally, by estimating values of J_{i-j} and U_{ijkl} for the lowest Bloch band, one may assume that values of J_{i-j} and U_{ijkl} for i, j, k, l describing the same or neighboring sites. In case of the U parameters it may be assumed that only all parameters i, j, k, l denote the same site.

This forms a classical Bose-Hubbard model introduced first by Jaksch and Zoller [36]:

$$\mathcal{H}_{BH} = -J \sum_{\langle i,j \rangle} a_i a_j^\dagger + H.c. + \frac{U}{2} \sum_i n_i(n_i - 1) - \mu \sum_i n_i. \tag{1.9}$$

Recently corresponding to U_{iiij}, for i, j denoting neighboring sites have started being included. The are w associated with additional $a_j, a_i^\dagger, n_i$-type couplings. These are interpreted as density-dependent tunnellings and are sometimes included as a correction [37]. For lattice dephts s between $s = 4E_R$ and $s = 40E_R$ value of U_{iiij} is between 5%-10% of the tunnelling coupling constant J. Multiplied by $n_i + n_j - 1$ the additional are important contribution. Other terms such as U_{iijj} are orders of magnitude smaller [38].

Although energy scales defined by J and U were determined to be insignificant compared to the interband gap, rates of changes of this parameters $\dot{J}, \dot{U}$ for typical optical lattice parameters may become dominant (this requires microsecond-scale dynamics). This notion will be explored further in Section 5 where dynamical couplings of different Bloch bands will be taken into account. See also [39].

A single-band model has the advantage of relative computational simplicity as compared to the Multiband Bose-Hubbard model (1.6). Using the latter for realistic systems is unfeasible. Recently a method of constructing an effective model for static problems has been proposed [38, 40, 41]. It consists of creating a single-band like BH model but using interacting n particle ground states as a onsite Hilbert space. Section 4 will show our contribution to this approach (efficient numerical diagonalization and dynamical simulation).

1.2.1 The disorder

The disorder and more generally imperfections of experimental systems are inherit part of the Nature. Study of disordered systems in which disorder may be controlled, prepared repetitively is possible with ultracold atoms.

One of first important example were crystalline structure imperfections [42] which affect both electric resistivity and may even be used in engineering applications such as material strain hardening. The optical lattice potential does not admit imperfections of this kind.

The nontrivial, quantum effects of the disorder in condense matter systems were introduced in the seminal contribution of Anderson [43], predicting an exponential localization of all energy eigenstates of a single particle in a periodic potential when additional random impurities are added to it. The special kind of disorder in the system, a quenched disorder (in which the disordered medium does not evolve during the typical timescale of the experiment) models correctly a multitude of disorder effects in matters such

as transport, localization effects [44, 45], spin glass [46], percolation [47], quantum chaos [48, 49].

In order to characterize the disordered system, one should either average over different realizations of disorder which is usually a hard task or consider systems large enough so that they become self-averaged. This is largely beyond scope of current numerical algorithms and for self-averaged systems only approximate methods (such as mean field methods variants) are available. Moreover disorder effects make minimization of energy troublesome as typically many local minima of the energy functional appear. Reaching the true ground state is then challenging.

In recent years, it has become clear that ultracold atoms offer a new paradigm of disordered systems study, due to the fact that *random* or *quasi random* disorder may be produced in these systems in a *controlled* and *reproducible* way. Standard methods to achieve such controlled disorder are the use of speckle patterns [50, 51] which can be added to the confining potential, or simultaneous presence of additional optical lattice of incommensurate frequency [9, 52, 53]. Other methods include using an admixture of different atomic species randomly trapped in sites distributed across the sample and acting as impurities [54, 55], or the use of inhomogeneous magnetic fields. Indeed, if an average value of such a field is close to the Feshbach resonance, then even small fluctuations of the field translate to noticeable spatial variation of the scattering length [56, 57].

In the Florence experiment [10] an optical lattice potential which would allow the studies of disorder has been prepared by switching on an additional optical lattice potential of height $s_2 \ll s_1$ with wave length λ_2 incommensurate with the main optical lattice length λ (see also [58]). All in all inclusion of these potentials leads to adding to the tight binding Hamiltonian (1.9) a local chemical potential term of the form $\sum_i \epsilon_i n_i$ with

$$\epsilon_j = s_2 E_{R,1} \sin^2\left(\frac{\pi j \lambda}{\lambda_2} + \phi\right). \tag{1.10}$$

1.2.2 Bose-Hubbard model solutions

The Bose-Hubbard model Hamiltonian (1.9) is a sum of single site Hamiltonians coupled by the tunnelling terms coupling nearest neighbour sites. The underlying lattice may be arbitrary, however in this thesis we restrict ourselves to simplest cases: linear chain, planar square lattice, simple cubic lattice.

The general solution of the Bose-Hubbard model (also its multiband variants) is not known analytically. Typically each lattice site is occupied by up to a few bosons. Hilbert space dimension of any realistic lattice (consisting of ~ 100 lattice sites in each direction) prohibits any approach which relies on expressing eigenfunction in the full basis.

Special cases $J = 0$ or $U = 0$ are, however, exactly solvable. In the first case the Hamiltonian (1.9) is already diagonal in the Fock basis $|n_1, \ldots, n_M\rangle$. The not interacting case, $U = 0$ may be approached by using a Discrete Fourier Transform to translate the Hamiltonian from real space Fock basis to momentum Fock basis with momentum modes $|k\rangle$ defined as:

$$|k\rangle = \frac{1}{\sqrt{L}} \sum_{j=1}^{L} \exp(ikj)|j\rangle. \tag{1.11}$$

The Hamiltonian (1.9) is then transformed into:

$$\sum_{k=\frac{2\pi n}{L}} E_k a_k^\dagger a_k, \quad E_k = -\mu - 2J\cos k, \quad a_k = \frac{1}{\sqrt{L}} \sum_{j=1}^{L} a_i. \tag{1.12}$$

Thus the free boson gas in the optical lattice potential is described by a Fock state in the momentum space — with all particles condensed in a momentum 0 state:

$$|\psi\rangle = (a_{k=0}^\dagger)^N |\Omega\rangle. \tag{1.13}$$

Moreover, higher Bloch bands are not involved, as the only way to couple different Bloch band is by an interaction term proportional to $U = 0$.

Most approaches to the remaining case, when both J and U are nonzero are either numerical ansatzes (such as a weak-coupling Bogoliubov approach [59, 60]) a perturbative expansion (a strong coupling expansion: [61]) or numerical computations. Bethe ansatz is applicable in a limited number of situations (for example in the $U \to \infty$ case of hardcore bosons [62])

Most successful numerical approaches are either Density Matrix Renormalization Group (works in 1D, gives access to a wavevectors and enables time evolution) or Quantum Monte Carlo methods [63, 64]. Standard algorithms implementation is available for example as an ALPS package [65].

1.3 The MPS approach

The Bose-Hubbard model introduced briefly in the previous paragraph is an example of a broad class of lattice Hamiltonians that are characterised by "on-site interactions" and limited range of intersite couplings. If studied in a 1D lattice, one may use an efficient representation, so called *Matrix Product State* representation that often efficiently represents physically relevant states in such settings [66, 67]. For example in the case of spin-1 Heisenberg model the efficient representation of the ground state as an MPS has been available for several years [68].

Let us consider a Hamiltonian over a 1D lattice which sites are labelled by numbers $i = 1, \ldots, L$ of the following form:

$$H = \sum_{i=1}^{L} H_i + \sum_{i=1}^{L-1} H_{i,i+1}. \tag{1.14}$$

Ir acts on a Hilbert space $\mathcal{H} = \mathcal{H}_1 \otimes \mathcal{H}_2 \otimes \ldots \otimes \mathcal{H}_L$, for $\mathcal{H}_i$ being a local Hilbert space for a single site i. In (1.14) H_i denotes a single site Hamiltonian operator acting nontrivially only on a site i. Similarly, operator $H_{i,i+1}$ acts on two neighbouring sites i and $i+1$. Different complex quantum systems defined over a lattice (such as Quantum Ising Model [69], Bose-Hubbard model (1.9)...) may be put or are explicitly of the form of Eq. (1.5).

In the zero temperature limit, systems modelled by the Hamiltonian (1.14) are described by a pure state $|\psi\rangle$ — the ground state. A general theorem of so called area laws [67, 70], warrants that a ground state $|\psi\rangle$ is close to the product state under quite general assuptions (of which energy gap separating the ground state with the excited states is most important). Quantitative formulation of this theorem requires introducing a notion of the entanglement entropy.

Theorem 1 *(Schmidt decomposition) For a state $|\psi\rangle \in \mathcal{H} = \mathcal{H}_A \otimes \mathcal{H}_B$ there exists a sequence λ_i such that $\sum(\lambda_i^{A:B})^2 = 1$ and*

$$|\psi\rangle = \sum_i \lambda_i^{A:B} |\psi_i^A\rangle |\psi_i^B\rangle. \tag{1.15}$$

Here, $(\lambda_i^{A:B})^2$ are eigenvalues of the both the reduced density matrix $\rho_B = Tr_A|\psi\rangle\langle\psi|$ and $\rho_A = Tr_B|\psi\rangle\langle\psi|$ with eigenvectors $|\psi_i^A\rangle$ and $|\psi_i^B\rangle$ respectively. Decomposition (1.15) is called **Schmidt decomposition** *[71].*

The above theorem introduces a sequence $\lambda_i^{A:B}$ corresponding to the Schmidt decomposition, so called **entanglement spectrum**. It may be computed for any bipartition of the full lattice system into two disjoint parts (one typically considers decomposition into "left" and "right" parts). With the spectrum one associates the notion of the **entanglement entropy** defined as

$$S(\psi) = \sum_i -(\lambda_i^{A:B})^2 \log(\lambda_i^{A:B})^2. \tag{1.16}$$

The basic properties of the entanglement entropy are:

- $S_i(\psi) = 0 \iff \psi = |\psi^A\rangle|\psi^B\rangle$.

The area laws theorem [67] establishes existence of an upper bound on the entanglement entropy of a ground state of the Hamiltonian of the form (1.5).

Theorem 2 *(Area law for local gapped 1D system [70]) Let L be a lattice system of the form of (1.14). If the system possess an unique ground state with first excited state separated by $\Delta E > 0$, then the entropy for a bipartition into sets $\{1, \ldots, k\} \cup \{k+1, \ldots, L\}$ satisfies:*

$$S(\rho_{\{1,\ldots,k\}}) \leq A. \tag{1.17}$$

For the precise definition of the constant A see [4]. Here it is important that A is not L-dependent.

One may perform [72, 73] the Schmidt decomposition of the state $|\psi\rangle$ with respect to any bipartition of the lattice of length L into "left" and "right" parts. Given a decomposition of the lattice $\{1, \ldots, L\} = \{1, \ldots, i\} \cup \{i+1, \ldots, L\}$, one may apply the Schmidt decomposition to "left" and "right" Schmidt vectors. Decomposing sets $\{1, \ldots, i\}$ and $\{i+1, \ldots, L\}$ as $\{1, \ldots, i-1\} \cup \{i\}$ and $\{i+1\} \cup \{i+2 \ldots, L\}$, gives rise to tensors $\Gamma^{[k],s}_{\beta\alpha}$ defined as:

$$|\psi^{[1\ldots i]}_{\alpha}\rangle = |\psi^{[1\ldots i-1]}_{\beta}\rangle |e^{i}_{\beta_i}\rangle \Gamma^{[i],\beta_i}_{\beta\alpha} \lambda^{[i-1]}_{\beta} \tag{1.18}$$

and

$$|\psi^{[i+1\ldots L]}_{\alpha}\rangle = \Gamma^{[i+1],\alpha_{i+1}}_{\alpha\beta} \lambda^{[i+1]}_{\beta} |e^{i+1}_{\alpha_{i+1}}\rangle |\psi^{[i+2\ldots L]}_{\beta}\rangle. \tag{1.19}$$

Altogether the above considerations provide an argument for describing the state $|\psi\rangle$ as:

$$|\psi\rangle = \sum_{\substack{\alpha_1,\ldots,\alpha_L \\ i_1,\ldots,i_M}} \Gamma^{[1],i_1}_{1\alpha_1} \lambda^{[1]}_{\alpha_1} \Gamma^{[2],i_2}_{\alpha_1\alpha_2} \ldots \Gamma^{[L],i_L}_{\alpha_{n-1}1} |i_1, \ldots, i_L\rangle =: \mathcal{M}(\Gamma, \lambda). \tag{1.20}$$

Summation of indices i_k is performed over a Fock basis spanning the local Hilbert space. Although such a basis may be infinite dimensional, in our applications ultracold temperature allows for its truncating to a finitely many states with low energy. Interaction limits the number of particle per site.

Ranges of indices α_i however may be expected to be exponential in system size L for a generic many-body state [74]. The area law bounds the entanglement entropy in case of a ground state. The sequence of $\lambda^{[k]}_i$ is dominated by few terms. Thus in the formula (1.20) the sequence $\lambda^{[k]}_i$ is expected to drop rapidly, warranting an additional approximation $\lambda^{[k]}_i = 0, i \leq \chi$ (all matrix elements involving higher indices are explicitly put to zero). Due to the area law theorem χ is expected to be efficiently bounded from above. Any vector expressed by the ansatz (1.20) is called a Matrix Product State (MPS) with a bond dimension χ. The set of all such states we denote by MPS_χ. As already stated $\bigcup_\chi MPS_\chi$ is full Hilbert space and each MPS_χ is a good example of an efficient variational manifold [75] (it is a certain product of Grassmann manifolds).

Minimization of energy $E(\psi) = \langle\psi|H|\psi\rangle$ over MPS_χ, which is a way to numerically estimate the ground state of the many body Hamiltonian, may be performed by numerical algorithms such as Density Matrix Renormalization Group (DMRG) [76].

The same result may be obtained by numerical imaginary time evolution, that is application of the evolution operator $\exp(-\tau H)$ to the initial state. The latter may be carried out for example by means of the time-evolution algorithms such as tDMRG [77, 78] or Time Evolving-Block Decimation (TEBD) [73]. The dynamical approach is motivated by a simple observation that a state $|\psi_0\rangle$, initial guess for the energy minimum may be expanded in eigenfunctions of the time-independent Hamiltonian:

$$|\psi_0\rangle = \sum_i c_i|\psi_i\rangle, c_i \neq 0 \tag{1.21}$$

under imaginary time evolution converges to the state with the lowest energy E_0 :

$$|\psi_0(t)\rangle = \sum_i c_i \exp(-iE_i t)|\psi_i\rangle \to c_0 \exp(-E_0 t)|\psi_0\rangle. \tag{1.22}$$

Note that generically, with probability 1 we have that $c_0 \neq 0$. Nevertheless, convergence of numerical computation to the true ground state is not certain. The reason for that are different truncations and roundoff errors. This is evident in the presence of the disorder potential which complicates the energy landscape and increases significance of small numbers.

The DMRG and TEBD algorithms enable also real time, unitary evolution of pure states. In this thesis an intensive use of the TEBD algorithm is made. It works by decomposing the operator $\exp(iH\delta t)$ as

$$\exp(iH\delta t) = \exp(iH_{odd}t\delta)\exp(iH_{even}\delta t) + o(\delta t^2), \tag{1.23}$$

where $H_{odd/even} = \frac{1}{2}\sum_{i=1}^{L} H_i + \sum_{i\in odd/even} H_{i,i+1}$. Then both H_{even} and H_{odd} consist of commuting two-site unitary operators, which may be easily applied to the MPS wavevector. Indeed $\exp(iH_{odd/even}\delta t)$ are just products of unitary two-site gates. [1]

The effects of higher order terms appearing in the Trotter expansion (1.23) are controlled by a proper choice of the time step δt. Alternatively, higher order analogues of (1.23) may be used [79].

[1] All the two-site gates may be applied in parallel by separate CPU cores. Applying the two-site unitary operators, and subsequent Singular Value Decomposition to recover MPS's vector representation in terms of λ and Γ tensors (see Section 1.3) constitute most of the CPU walltime of the whole TEBD implementation. This also means that the overall numerical complexity of the TEBD algorithm is $O(\chi^3)$.

1.4 Physics of the Bose-Hubbard model

The Bose-Hubbard Model predicts a phase transition between an insulator and a superfluid phase [80, 81]. Together with natural similarity to the Hubbard model for electron gas this fact sparked the interest of physics of ultracold atoms in the lattice potential.

By altering the power of lasers forming the lattice or using magnetic (or optical) Feshbach resonances [82] experimental exploration of phase diagrams of Hamiltonians modelling systems of ultracold atoms may be undertaken. A prime example is the Bose-Hubbard model, in which the mentioned techniques allow for independent control of U and J parameters. It is also possible for disordered systems, in which the disorder may be reproduced and controlled.

1.4.1 Phases: Mott Insulator, Superfluid, Bose-Glass

In the strongly interacting regime, in grand canonical ensemble, the Hamiltonian (1.9) is dominated by the term $\frac{U}{2}n(n-1)$ which fixes integer occupation of each lattice site. Thus, if the system is homogeneous in the low tunnelling regime, the Hamiltonian ground state is approximated by a product state of Fock states (with unique integer occupation). Such a state is a model state for the quantum phase of Mott Insulator (MI). The insulating properties of the MI phase are related to a finite energy gap for excitations. Elementary, particle-hole excitations cost energy of the order of U.

Finite value of J modifies this description by allowing for nonzero (of the order $\sim J^2$) on-site particle number variance: $\Delta_n = \langle\psi|n^2|\psi\rangle - \langle\psi|n|\psi\rangle^2 \neq 0$, Moreover the correlation function $c_{ij} = \langle a_i a_j^\dagger\rangle - \langle a_i\rangle\langle a_j^\dagger\rangle$ in this case is nonzero for $i \neq j$, and decreases exponentially with the distance $|i-j|$.

For large J the ground state of the BH model entails that the particles are delocalised over the whole lattice. In this case the correlation function decays algebraically: $c_{ij} \sim |i-j|^{-\nu}$ [81]. This regime may be also characterised by a nonzero condensate fraction, that is macroscopic occupation of a single-particle mode (the one delocalised over the whole lattice). The condensate fraction is defined as a largest eigenvalue of a single particle correlation matrix $M_{ij} = \langle a_i^\dagger a_j\rangle$ divided by total number of particles. In the Mott Insulator case the matrix M is almost diagonal, and in the thermodynamical limit its largest eigenvalue converges to 0. In the $U = 0$ case the condensate fraction ρ_c is 1 (all particles occupy the $k = 0$ momentum eigenstate). The superfluid phase is a gapless phase, the excitations are low-energy and long range excitations. The tunnelling allows also for long-range phase coherence.

A characteristic of the delocalised phase for the Bose-Hubbard Hamiltonian are superfluid properties of a gas. Superfluidity is related to ability of fluid to flow with zero viscosity in ultracold temperatures [83]. More precisely, if the velocity of a fluid with respect to walls of a container is

small enough, then the fluid is resistant to dissipation by creation of quasi-particles. At the level of the Bose-Hubbard model, the movement of the boundaries may be conveniently expressed in the comoving with the boundaries frame of reference by rotating in the complex plane the tunnelling constant [2] $J \to Je^{i\theta}$. The part of the fluid that is able to remain stationary despite the vessel movement, in the new coordinate frame is the part that responds to the imposed phase θ. The energy difference $E_\theta - E_0$ is equal to to the kinetic energy, of the superfluid part of gas $\frac{1}{2}mN\rho_s v^2$ (moving due to the phase gradient). The superfluid velocity is related to a phase gradient $v = \frac{\hbar}{m}\nabla\Theta(x)$. Thus, the superfluid fraction is defined as (see [52, 83]):

$$\rho_s = \frac{2m}{\hbar^2}\frac{1}{N}\frac{E_\theta - E_0}{(\nabla\Theta)^2} = \frac{1}{N}\frac{E_\theta - E_0}{J\theta^2}. \tag{1.24}$$

The latter equation stems from adopting the recoil energy as an energy unit and $\frac{a}{\pi}$ as a length unit. Note that in general superfluid fraction (described in the following paragraph) and condensate fraction are not equal.

The same value of ρ_s may be calculated by the so-called winding number statistics which is a standard way to compute the condensate fraction in the QMC approach [84].

Transition between the two phases in $T = 0$ is described by a quantum phase transition (QPT), through a different mechanism than classical phase transition. The QPT occurs as parameters of the Hamiltonian are modified and the ground state properties change suddenly by energy level crossings (perhaps avoided crossings in a finite system) as competing terms in the Hamiltonian change their relative relevance.

Up to now we have considered homogeneous systems. As described in Section 1.2.1 introduction of disorder may be performed by adding a local chemical potential μ_i (see Eq. 1.10), where μ_i are either explicitly calculated quasi random numbers or are considered purely random. Although some specific effects of imperfect randomness of local chemical potentials have been predicted [58], generically in case of strong interactions $U \gg J$ a new gapless insulator phase, a Bose-Glass (BG) phase emerges. Although the phase is gapless a typical excitation has a far from zero excitation energy, contrary to the SF phase [85].

The BG phase may be pictured as a Mott Insulator phase with random integer site occupation. The Bose-Glass phase has long been hypothesized to

[2] Indeed, symmetries not involving a time-reversal can be represented by a unitary operator. Galilean transformation to a inertial frame moving with relative velocity $\vec{v}$ is $G(v) = \exp(\frac{i}{\hbar}v\hat{Y})$, where $\hat{Y} = \hat{P}t - m\hat{X}$ is a generator of the symmetry. Then $\langle x|G(v)|\psi\rangle = e^{(i/\hbar)mvx - \frac{1}{2}mv^2t}\langle x|T(-vt)|\psi\rangle$, for T being a translation operator. Thus changing a frame of reference introduces a phase factor $e^{i\theta x}$ upon a wavefunction $\psi(x)$. The energy operator transforms just as in the classical case: $H' = H + Pv + \frac{1}{2}mv^2$, for small v approximately $H' \approx H$. Then the tunnelling constant $J' = \int w^*(x)\left(-\frac{\hbar^2}{2m} + V_{opt}(x)\right)w(x+a)e^{(i/\hbar)mva}\mathrm{d}x = e^{(i/\hbar)mva}J$.

separate Mott Insulator and Superfluid phases [80], but without a rigorous proof. Recent "theorem of inclusions" [86] seems to fill in this gap.

1.4.2 The mean field analysis

The Bose-Hubbard Hamiltonian may be analyzed through various mean field methods. As usual in the mean field approaches one considers a single node of the lattice coupled to the "mean field" formed by the reservoir of the other sites. The coupling is performed by expanding the tunnelling operator $a_i a_j^\dagger$ as

$$a_i a_j^\dagger = a_i \phi^* + a_j^\dagger \phi - |\phi|^2 \tag{1.25}$$

and in case of lack of translation-invariance:

$$a_i a_j^\dagger = a_i \phi_j^* + a_j^\dagger \phi_i - \phi_i \phi_j^*. \tag{1.26}$$

The mean field is determined by: $\phi_i = \langle a_i \rangle$. Then the mean field homogeneous Hamiltonian is the functional for the site i :

$$E_i(\psi) = \langle \psi | H_i | \psi \rangle - Jz a_i \phi^* - Jz a_i^\dagger \phi + Jz|\phi|^2 = \langle \psi | H_i | \psi \rangle - Jz|\phi|^2, \phi = \langle \psi | a | \psi \rangle. \tag{1.27}$$

It is minimized with respect to coefficients of expansion of a single-site state $\phi = \phi_j = \sum_i a_J |i\rangle$. It turns out that this simple approach enables to describe the phase diagram in 2 and 3 spatial dimensions reasonably well. The resulting phase diagram is in Figure 1.2. Other methods that lead to similar results, entailing similarly shaped MI lobes agree up to a few percent include: QMC [87], the strong coupling expansion [61, 88] within the bosonic DMFT approach [89], a quantum rotor model [90].

Although the phase diagram is reasonably described by the mean field approach, there are crucial differences. In the mean field approach the Mott Insulator state is a Fock state, i.e. $\psi = |n\rangle$. However, "exact" QMC results predict that $\langle n^2 \rangle - \langle n \rangle^2 \neq 0$.

1.4.3 The Gutzwiller variational ansatz

The lattice Hamiltonian may be analyzed also by the so-called Gutzwiller mean field variational ansatz, that is the energy minimum is sought within the submanifold of full Hilbert space formed by product states. The minimization is performed over parameters $f(i,j)$:

$$\psi = \prod_{i=1}^{L} \sum_{j=1}^{d} f(i,j) |e_j^i\rangle, \tag{1.28}$$

where $|e_j^i\rangle$ is j-th orthonormal basis vector of single site Hilbert space for site i.

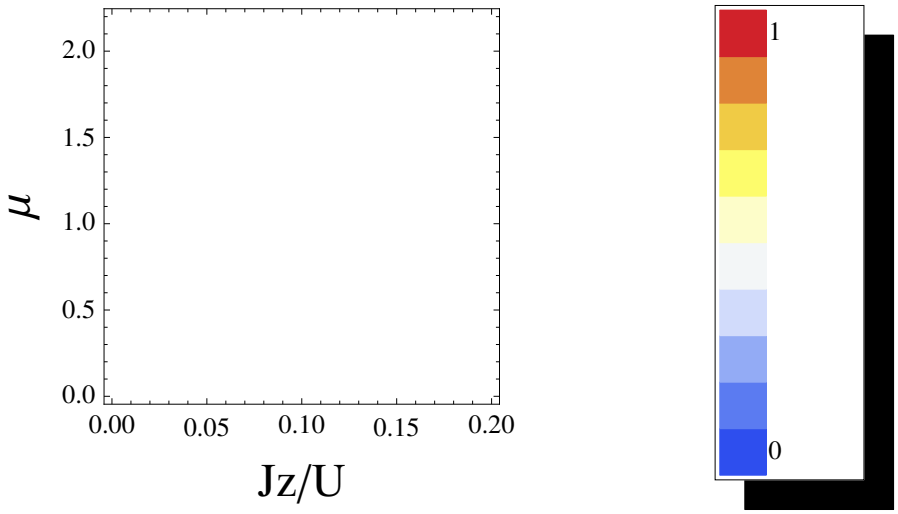

Figure 1.2: Superfluid order parameter $\phi = \langle a \rangle$ as a function of chemical potential μ and tunnelling J. The order parameter is zero in MI phase and nonzero in the SF phase. Each MI lobe corresponds to integer occupation of sites (different in each lobe).

Notice that in the mean field approach, and so in the Gutzwiller ansatz, both superfluid fraction and condensed fraction are related to the order parameter $\phi = \langle \hat{a}_j \rangle$. Indeed the mean field ansatz is a single-site description where the energy functional describes a single site coupled to the reservoir. The long-range correlations may either completely disappear or be seriously overestimated: whether the correlation function $\langle a_i a_j^\dagger \rangle = \langle a_i \rangle \langle a_j^\dagger \rangle$ is zero or nonzero, does not depend on site i and j relative location. Therefore the correlation matrix $\langle a_i a_j^\dagger \rangle$ is, in homogeneous case, strictly diagonal or has *all* nondiagonal terms equal to $|\phi|^2$. In such a case, the condensate fraction is approximately proportional to $|\phi|^2$. Thus, nonzero condensate fraction is synonymous with a nonzero value of the order parameter ϕ.

In fact the mean field presented in the previous chapter is mathematically equivalent to the Gutzwiller ansatz presented here. In general different nonequivalent mean field approaches may be formulated. One example is perturbative mean field analysis in Section 6.1.2.

1.4.4 The DMRG study

The phase diagram of the Bose-Hubbard model may be also obtained for dimension 1 using the MPS ansatz, and energy minimization performed by the DMRG or imaginary time TEBD (both approaches yield normalized ground states that satisfy $|\langle \psi_{DMRG} | \psi_{TEBD} \rangle| = 1$ for all parameters).

The DMRG approach, as well as the imaginary time evolution by the

TEBD enables to find a state with minimal energy for a given finite lattice length L and total number of particles N. The phase diagram of the BH model is typically considered in the thermodynamical limit with fixed N/L ratio and $L \to \infty$ in the variables J/U and μ/U. To introduce the notion of chemical potential given definite L and N, we define $E(L, N)$ to be the energy. Adding a single particle to the system with integer density $\rho = N/L$ should cost a value of the chemical potential $\mu_+ = E(L, N+1) - E(L, N)$ and removing one should release energy $\mu_- = E(L, N) - E(L, N-1)$. This means that if the chemical potential $\mu > \mu_+$ then it is worth to put an extra particle in the system to optimize (lower) its energy. Analogously for $\mu < \mu_-$ removing the particle lowers the energy. Hence for $\mu_- < \mu < \mu_+$ the phase contains exactly N particles. If for some J the phase is incompressible insulator phase, the Mott Insulator, then we expect $\mu_+ > \mu_-$ even in the thermodynamical limit $N/L \to \rho$ as $L \to \infty$. Thus calculating curves $\mu_+(J/U)$ and $\mu_-(J/U)$ gives the upper and lower boundary of the Mott Insulator phase in the phase diagram of the Bose-Hubbard model. Some numerical finesse is required to obtain the converged phase diagram in the thermodynamical limit. MI-SF border close to the Mott-Insulator tip converges slowly with L and its precise computation requires a serious numerical computation [91].

The phase diagram obtained by the DMRG computation is presented in Figure 1.3.

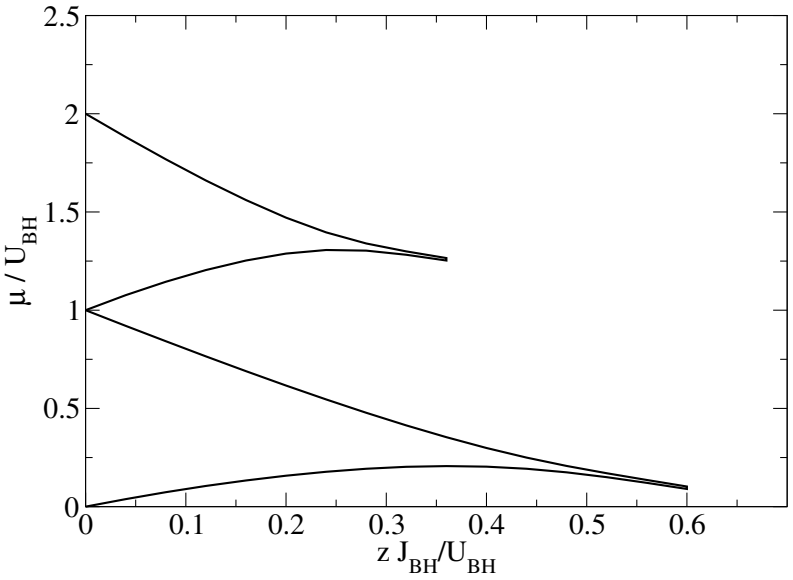

Figure 1.3: The 1D phase diagram of a Bose-Hubbard model obtained using the imaginary time evolution and the TEBD algorithm. Image from [92].

Chapter 2

Fidelity [93]

If there is a family of Hamiltonians depending on some parameters, then the notions of phases, phase diagram and phase transitions arise in a natural way. Let us assume that the family of Hamiltonians is parametrised by λ as $H(\lambda) = H_0 + \lambda H_1$, where H_1 is called a driving Hamiltonian. In the case of the Bose-Hubbard model (1.9) one consider $\lambda = J$, and H_0 being the atomic part of the Hamiltonian, and H_1 the kinetic energy term. Wavefunctions describing states of the system in different phases are expected to be substantially different which would mean that the fidelity function F (and fidelity susceptibility χ) defined as [94]:

$$F(J,\delta) = |\langle J - \delta/2 | J + \delta/2 \rangle|, \qquad F(J,\delta) \approx 1 - \delta^2/2\chi(J,\delta) + O(\delta^4) \quad (2.1)$$

should have a pronounced minimum (maximum) in the vicinity of the phase transition. In above definitions the parameter δ is small. In the thermodynamic limit, the overlap between two ground states computed for different values of the driving parameter is zero, no matter how small the δ is. This is known as the Anderson orthogonality catastrophe [95].

The character of the minimum of F depends highly on the nature of the transition. If the transition is due to the level crossing, then as the driving parameter λ changes the ground state changes abruptly from one state to the other orthonormal state at the critical value of $\lambda = \lambda_c$. Thus at λ_c we have $F(\lambda_c, \delta \to 0) = 0$ (generically $F(\lambda_c, \delta \to 0) = 1$). Moreover behaviour of $F(\lambda, \delta)$ for $\lambda < \lambda_c$ and $\lambda > \lambda_c$ both for $\delta < 2|\lambda - \lambda_c|$ stems from properties of different states and they are absolutely unrelated. Both sides may be described by different critical parameters [96]. If however, the transition is due to the avoided crossing (or other mechanism in which no energy crossing occurs) the exactly opposite statement to the above is valid ($F(\lambda_c, \delta \to 0) = 1$, and $F(\lambda_c, \delta)$ is expected to be analytical function if one works far form the thermodynamical limit). Such a situation occurs in the case of the Bose-Hubbard model.

The correlation length of the system typically diverges at the transition point with a characteristic critical exponent ν :

$$\xi(\lambda) \sim \frac{1}{|\lambda - \lambda_c|^{\nu}}. \tag{2.2}$$

For such systems, by considering appropriate scalings, general results on scaling of fidelity function may be obtained. At the critical point $\chi \sim M^{2/d\nu}$, while for a finite separation $\chi \sim M/|\lambda - \lambda_c|^{2-d\nu}$, where d is system dimension [97, 98]. Moreover, in the limit of $M \to \infty$ taken for fixed, nonzero small δ, for $\lambda \approx \lambda_c$ we have that $\ln F \sim -M|\delta|^{d\nu}$, while far from the phase transition $\ln F \sim -M\delta^2/|\lambda - \lambda_c|^{2-d\nu}$ [99–101].

The Bose-Hubbard model (1.9) admits a quantum phase transition between Mott Insulator and superfluid phases. This transition is of Berezinskii-Kosterlitz-Thouless (BKT) type [80]. The correlation length is infinite on the superfluid side and on the Mott Insulator side the correlation length diverges as: $\ln \xi \sim 1/\sqrt{\lambda_c - \lambda}$ [81, 102]. This means that no critical exponent ν can be defined on neither side of the transition and so the above scaling expressions do not apply.

2.1 Numerical results

We have studied quantum fidelity by means of numerical computation. The DMRG algorithm allows for determining ground states as MPS wavevectors for various J values. We have fixed $U = 1$ and considered values of J laying on a uniform grid with a step ΔJ. Then definition (2.1) is then used to compute the function F with various δ's, all being a multiplicity of base ΔJ.

From Fig 1.3 it is clear that MI-SF phase transition occurs approximately for $J_c/U \approx 0.3$. This value is supported by other numerical studies [81, 103–109] which give estimates for the transition point location ranging from 0.26 to 0.305, however most results falling between 0.295 and 0.305. Nevertheless, Figures 2.2, 2.3 and 2.4 clearly show that the position of the minimum computed by the DMRG method for the open boundary conditions (OBC) falls in the region of $J/U = 0.2 - 0.22$. We notice that the minimum of fidelity is significantly shifted towards the lower J values.

Moreover periodic and open chain results are profoundly different even qualitatively. As shown in Figure 2.1, the minimum of the fidelity function of the open chain is much flatter and shifted much deeper inside the MI region than in the periodic boundary condition (PBC) case. The OBC and PBC curves differ diametrically close to the transition. Therefore, separate numerical studies of both cases have been undertaken.

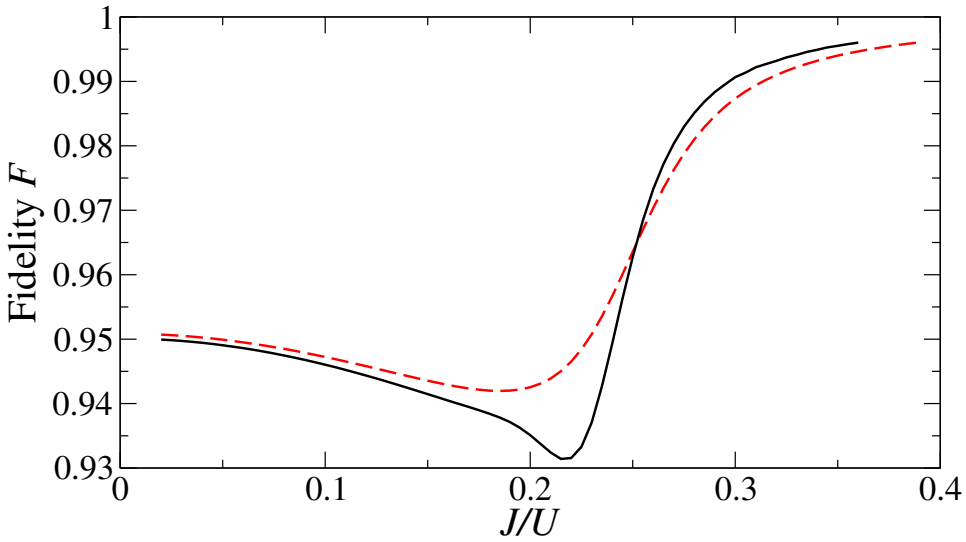

Figure 2.1: Black solid line shows fidelity in a periodic chain, while the dashed red line shows fidelity in an open chain. In both cases $L = 64$ and $\delta = 0.02$. Image from [93].

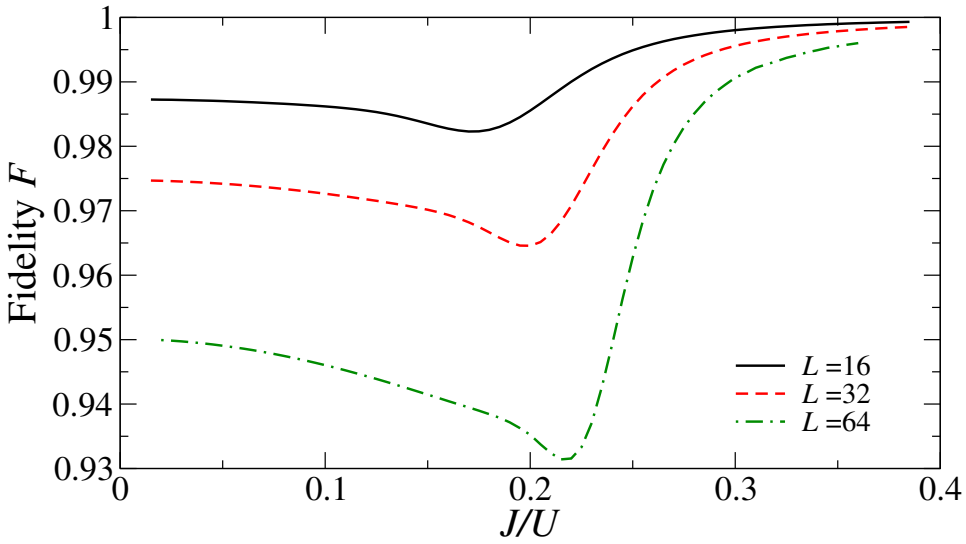

Figure 2.2: Fidelity in a periodic Bose-Hubbard model for different system sizes and $\delta = 0.02$. Image from [93].

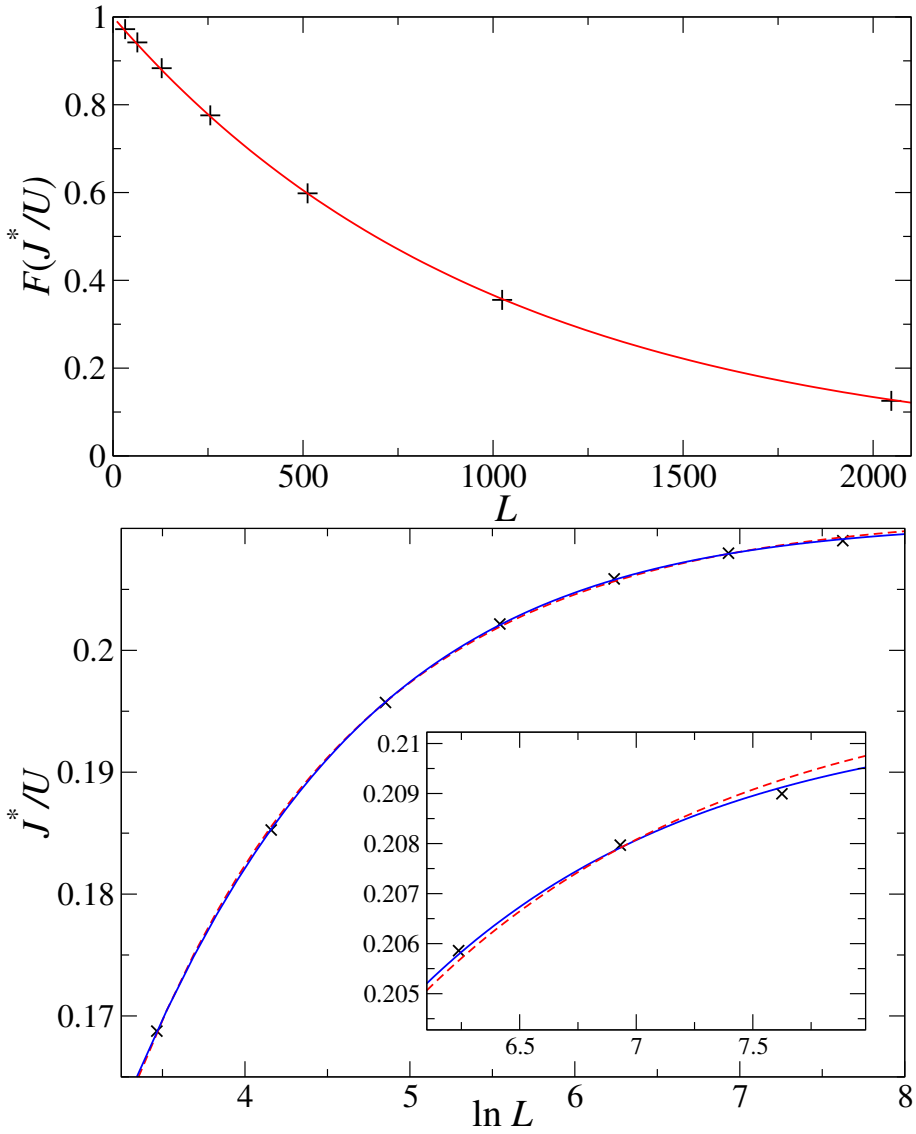

Figure 2.3: Upper panel: the value of fidelity at the minimum as a function of the system size (open boundary conditions). Pluses (upper panel) come from numerics done for $\delta = 0.02$ and $L = 32, 64, 128, 256, 512, 1024, 2048$. The line represents Eq. (2.3) with $\alpha \simeq 2.51$ obtained from the fit. Lower panel: X's show position of the minimum of fidelity as a function of the system size (open boundary conditions) — numerics done for $L = 32, 64, 128, 256, 512, 1024, 2048$ and $\delta = 0.02$. The red (dashed) line is the fit (2.4) while the blue (solid) corresponds to (2.5). The inset shows the zoom for large L to simplify comparing of both fits. Image from [93].

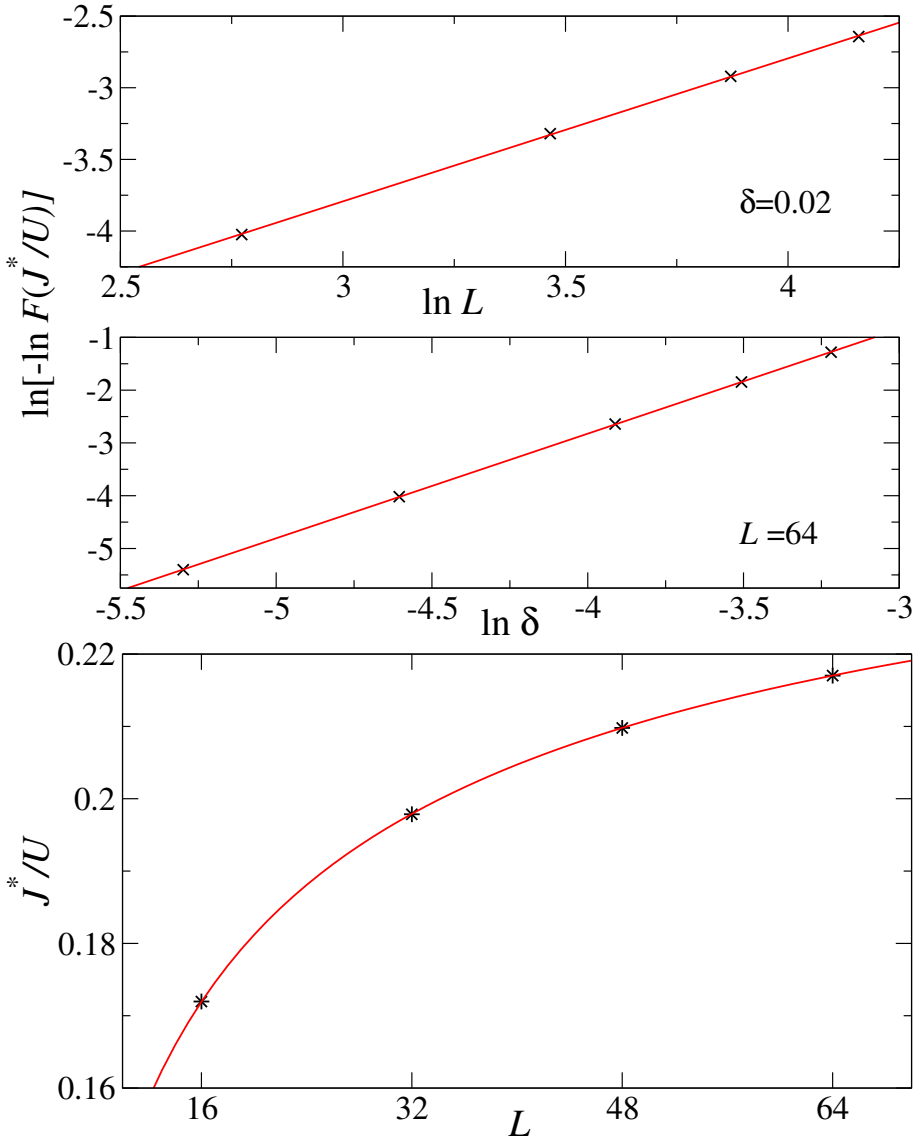

Figure 2.4: Scaling of the minimum of fidelity with the system size L and the parameter shift δ in a periodic Bose-Hubbard chain. Top panel: X's show numerics for $L = 16, 32, 48, 64$. The line represents the fit $\ln[-\ln F(J^*/U)] = -6.787 + 0.998 \ln L$. Mid panel: X's show numerics for $\delta = 0.005, 0.01, 0.02, 0.03, 0.04$. The line represents the fit $\ln[-\ln F(J^*/U)] = 5.104 + 1.982 \ln \delta$. Bottom panel: position of the minimum of fidelity as a function of the system size L in the periodic Bose-Hubbard model. Stars show numerics done for $\delta = 0.02$, while the line represents Eq. (2.4) with $J^*(\infty)/U \simeq 0.27$, $a \simeq 0.33$, and $b \simeq 0.44$ (all coming from the fit). Image from [93].

2.2 Open boundary conditions

We start our considerations by looking at the value of the fidelity at the minimum. We denote the position of the minimum as J^*/U. Our numerics suggests the following functional form of the fidelity:

$$F(J^*/U, \delta) = \exp\left(-\alpha L \delta^2\right), \tag{2.3}$$

where α is some constant. The detailed analysis of the relevant numerics is given in the caption of Figure 2.3. Let us notice that Eq. (2.3) works well also for $F(J^*/U, \delta) \ll 1$, i.e., in nonperturbative regime, where the fidelity is no longer described only by fidelity susceptibility, by lowest order Taylor expansion.

Having determined positions J^*/U of fidelity minima for various L, an extrapolation to the limit $L \to \infty$ should be performed. We were unable to find an extrapolation scheme that would reproduce the location of the critical point found in other theoretical works. We have made two approaches to the problem.

First, we have tested:

$$\frac{J^*(L)}{U} = \frac{J^*(\infty)}{U} - \frac{a}{L^b}, \tag{2.4}$$

which by standard fitting algorithms implemented in *Mathematica* package results in fitted parameters values $J^*(\infty)/U = 0.2114 \pm 0.0003$, $a = 0.53 \pm 0.02$, and $b = 0.73 \pm 0.02$ (Figure 2.3). The extrapolated minimum of fidelity in the $L \to \infty$ limit, $J^*(\infty)/U \simeq 0.2114$, is distant from the critical point position $(J/U)_c \approx 0.3$. The fit (2.4) was proposed in Ref. [110] which focused on the 2D transverse Ising model. However, in that model, critical exponents are well defined, contrary to the BH model. That is why the above scaling, contrary to the mentioned Ising model, is not well supported by theory in the BH model case.

We have also tried

$$\frac{J^*(L)}{U} = \frac{J^*(\infty)}{U} - a\frac{\ln L}{L^b}. \tag{2.5}$$

The previous fitting function was augmented by a logarithmic (as a function of lattice size L) correction (Figure 2.3). The fit gives $J^*(\infty)/U = 0.2106 \pm 0.0001$, $a = 0.375 \pm 0.007$, and $b = 0.991 \pm 0.006$. The χ^2 statistical parameter of these fits equals about 2.7×10^{-7} for the fit (2.4) and 3.9×10^{-8} for the fit (2.5). The value of the extrapolated transition position $J^*(\infty)/U$ is very similar as in the fit given by Eq.(2.4). Still the numerical quality of this fit is better (the inset of Figure 2.3).

The fit with Eq.(2.5) suggests that the shift of position of the minimum of fidelity scales as $\ln L/L$. Note that because we have considered lattice

chains of lengths differing by several orders of magnitude, the factor $\ln L$ was substantially different for different points.

We have also studied the position of the maximum of fidelity susceptibility for the same chain lengths L under open boundary conditions. We have used dependence of $F(J/U, \delta)$ on δ to extract $\chi(J/U, \delta)$ from Eq. (2.1). We have used the fitting function in Eq. (2.4) to perform the fit and obtained $J^*(\infty)/U = 0.2121 \pm 0.0002$. This result is very similar to previous results.

2.3 Periodic boundary conditions

In this section we discuss results on fidelity in the Bose-Hubbard model defined on a linear lattice chain under periodic boundary conditions. Numerical limitations restrict our studies to chain lengths L smaller by the factor of 32 than in the previous Section. Still we were able to achieve an increase of the size of studied systems by a factor of 4 as compared to previous studies [110] (performed by means of exact diagonalization).

As in Sec. 2.2, we find the value of fidelity at minimum, Eq. (2.3), well describes the numerical result (see Figure 2.4). On the other hand, the extrapolation of the position of the minimum, to the thermodynamical limit $L \to \infty$ using scaling in Eq. (2.4) gives a significantly different answer. The details are show in Figure 2.4 and its caption. The extrapolated fidelity minimum position is $J^*(\infty)/U = 0.270 \pm 0.008$, which agrees with previous works [111]. Also the $1/L$ scaling is no longer satisfied. We have determined that the convergence is best described by a smaller exponent: $b = 0.44 \pm 0.05$ in formula (2.4).

To increase the probative value of numerical evidence, it should be considered for larger system sizes. The main problem is that DMRG/TEBD algorithms with periodic boundary conditions are more complex and difficult to implement efficiently. In fact the final numerical complexity is less favourable under periodic than open boundary conditions [112]. The reason for this discrepancy is that under periodic boundary conditions many more singular values have to be kept to reach the same accuracy as in the open boundary conditions [112, 113]. We have observed this phenomenon in our computations. Still the periodic boundary conditions have a clear advantage over the open systems: there is no notion of boundary effects that seems to alter dramatically the results as seen in the previous section. Only finite size effects remain.

To be precise, for numerical computation we have used bond dimension of at most $\chi = 240$ for both OBC and PBC, which led to similar accuracy of the computed ground state although the longest chain for the OBC was $L = 2048$ and for PBC it contained only $L = 64$ sites. The accuracy of determination of the ground state was verified by calculating the total discarded weights in the DMRG/TEBD procedure.

2.4 Discussion

Our results show that there is a significant difference between fidelity in the open and periodic chains. The ground state differ also at the level of site occupation. The PBC case is translationally invariant and $\langle n_i \rangle = 1$ for all i. For the OBC it may be true far from the boundaries, but occupation of sites close to the edges of the lattice is affected. We believe that this inhomogeneity makes the difference, but we do not have the explanation of why it is so large, nor why it seems to flatten the fidelity function dependence on J near the minimum.

It is worth to realize that such an inhomogeneity did not cause much trouble in the determination of the location of the critical point through the studies of the decay of the correlation functions [91, 107]. The ground states in these studies were obtained through the open-chain DMRG simulations, so they were the same as in our calculations. As expected, the influence of inhomogeneities on the site occupation near the center was marginal for large-enough systems. Thus, one could possible obtain reliable results by computing the two-point correlation functions $\langle a_i a_j^\dagger \rangle$ near the center, for i, j far from edges of the chain.

The fidelity approach differs as it takes into account whole vectors, not observables calculated at particular sites. The parts of the system near the center and those near the edges both contribute to the final result with equal weights. The inner product of ground states contracts whole state into a single number.

A clear theoretical advantage of using periodic boundary conditions is hampered by dramatic increase of computational cost. Our results show that using "sufficiently large" open system is not a good alternative. A possible solution of that problem would be to redefine the inner product so that the sites close to boundaries were not taken in the account or use so-called smooth boundary conditions [114]. For a short overview see also an on-line short article [115].

The influence of the edges on fidelity may also be reduced, at least partially, by considering partial trace of the state vector, instead of the whole chain $\rho_\psi^k = \mathrm{Tr}_{\{1,\ldots,k\}\cup\{L-k+1,\ldots,L\}} |\psi\rangle\langle\psi|$. Then, instead of computing the fidelity $|\langle J - \delta/2 | J + \delta/2 \rangle|$, its analogue quantity for density matrix may be computed: $F_k^\rho(J,\delta) = \mathrm{Tr}\rho^k_{|J-\delta/2\rangle}\rho^k_{|J-\delta/2\rangle}$. We have been able to implement computation of $F_k^\rho(J,\delta)$. Preliminary results show that minimum of $F_k^\rho(J,\delta)$ is less shifted to the Mott Insulator region with respect to the PBC computation, than $F(J,\delta)$. However the difference is not very pronounced. For lattice lengths $L = 32, 64, 128, 256$ we compute $F_k^\rho(J,\delta)$, for $k = (L-16)/2$ leaving the reduced density matrices describing a system with 16 particles (in the middle of the sample).

We have again attempted to extrapolate the position of minimum using Eq. (2.4). We have determined that, the minimum of fidelity extrapolates to

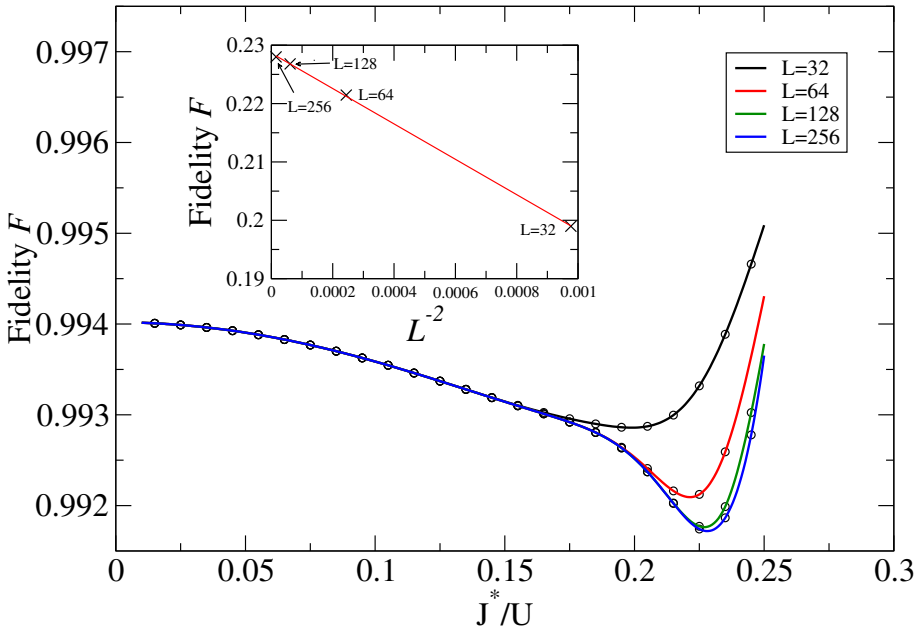

Figure 2.5: Fidelity of states described by reduced density matrices of a BH chain of length L to a subsystem consisting of middle 16 lattice sites. Full vectors were computed under open boundary conditions. The fidelity minimum is shifted towards large J values (see Figure 2.2). The inset shows extrapolation of minima position in the $L \to \infty$ limit. The line is a curve $F = 0.2286 - 30.32L^{-2}$. For Fidelity the shift parameter $\delta = 0.01$ was used.

$J^*(\infty)/U = 0.2289$, again far from the expected result ≈ 0.295 or the PBC result 0.27. Curiously in contrast to the OBC case the fidelity minimum converges to the limit with power -2 (see the inset in Figure 2.5 for the fitting results to quantify the quality of evidence supporting that assertion).

This results signify that the improved OBC estimation of the infinite limit is shifted by approximately 0.019 to the SF region w.r.t to the brute force OBC calculation with no regards to boundaries. The main obstacle for further investigation was that complexity of our implementation of F_k^ρ computation was $O(\chi^6)$. Therefore the numerics was limited to a relatively small value of $\chi = 60$. This could have had an impact on the extrapolation of fidelity minimum location.

The extrapolation of fidelity minimum positions in finite chains under OBC failed to converge to the correct value in the thermodynamical limit. This feature, to our knowledge, is not common. At the very least, we have determined that in the case of Quantum Ising Hamiltonian both PBC and OBC give the same limit, coinciding with phase transition location $g = 1$ [116, 117]. The key difference is that the correction of fidelity minimum location due to finite size effects is $\sim L^{-1}$ in the OBC case [118] and $\sim L^{-2}$ in the PBC case.

Better understanding of our numerical results, in particular the fitted scaling of fidelity, should come from the theoretical derivation of the finite system-size scaling. In particular the asymptotics of the finite system size correction to the position of the minimum of fidelity (maximum of fidelity susceptibility) in a BKT transition should be worked out.

Chapter 3

Spectral analysis of BH Hamiltonian [119, 120]

3.1 State extraction by the Fourier Transform [92]

As described before determining a ground state of a complex quantum systems is both possible and desirable. The ground state is not the only eigenstate of interest. Dynamical processes modelled by the time-dependent Schrödinger equation drive the system from the ground state by introducing excitations. Identifying these excitations is vital in description of the dynamics. It also relates the notion of adiabaticity or lack thereof [121, 122] to the intrinsic properties of physical process.

Computing numerically eigenstates different than the ground state present in a wavepacket $|\tilde{\psi}\rangle$, being a result of a time-dependent process, may be achieved by developing variants of DMRG algorithms targeting several eigenstates of the studied Hamiltonian [65]. Still this method suffers from accuracy problems as in general it is not possible to use the same left and right Schmidt vectors to represent efficiently both the ground state and low excited states. Another method is to use Lanczos sparse matrix diagonalization algorithm, which has been generalized to the MPS formalism [123]. Still, these methods allow for calculation only of a handful of eigenernergies and corresponding eigenvectors of a many-body Hamiltonian. Lanczos diagonalization may target particular states by means of their energy only.

Another method to compute some excited eigenstates is to identify good quantum numbers that characterize these eigenstates. Then one performs several ground state computations with standard DMRG approaches [65, 124], fixing the good quantum number to a different value each time. Altogether a different subspace of the full Hilbert space is chosen each time. Naturally this is possible only in special cases.

Translationally invariant Hamiltonians, even with additional external potential which breaks only weakly the translational invariance (such as

the BH Hamiltonian describing externally trapped gas) or translationally invariant systems with open boundary conditions, may contain myriads of degenerate eigenstates. For example, particle-hole excitations in a deep 1D optical lattice of length L may be performed in $O(L^2)$ nonequivalent ways with very similar excitation energy. Large spectral density makes differentiating these eigenstates troublesome.

To relate the computed eigenvectors $|\psi_i\rangle$ of the Hamiltonian to the studied physical dynamical process, inner products $\langle\psi_i|\tilde{\psi}\rangle$ may be computed. However the diagonalization makes no use of the analyzed wavepacket $|\tilde{\psi}\rangle$ (perhaps except for the average energy of $|\tilde{\psi}\rangle$ which might be used for eigenstate targeting) at all, only the Hamiltonian is used. To analyze a wavepacket $|\tilde{\psi}\rangle$ a state *decomposition* algorithm is required, not the Hamiltonian diagonalization.

In this section we introduce an another approach, that enables us to extract those eigenstates $|\psi_i\rangle$ for which $\langle\psi_i|\tilde{\psi}\rangle \neq 0$ where $|\tilde{\psi}\rangle$ is the analyzed wavepacket given as an MPS.

The method is based on performing a Fourier Transform directly on a time-series defined by a unitary evolution under a time-independent Hamiltonian of the analyzed wavepacket:

$$|\tilde{\psi}(t)\rangle = \exp\left(-\frac{i}{\hbar}Ht\right)|\tilde{\psi}\rangle = \sum_i \exp\left(-\frac{i}{\hbar}E_i t\right) c_i|\psi_i\rangle. \tag{3.1}$$

The time autocorrelation function $C(t) = \langle\tilde{\psi}(0)|\tilde{\psi}(t)\rangle = \sum_i \exp(-\frac{i}{\hbar}E_i t)|c_i|^2$, gives the spectrum in terms of the Fourier transform:

$$\tilde{C}_T(E) = \frac{1}{T}\int_{-T/2}^{T/2} \mathrm{e}^{\frac{iEt}{\hbar}} C(t)\mathrm{d}t = \sum_i |c_i|^2 \,\mathrm{sinc}\frac{(E-E_i)T}{2\hbar}. \tag{3.2}$$

In the $T \to \infty$ limit the $\tilde{C}_T$ spectrum converges to $\sum_i \delta(E-E_i)|c_i|^2$. In numerical applications the total available time-series signal length is finite, resulting in nonzero width of the FT peaks.

This analysis enables to determine the eigenenergies of eigenvectors forming the wavepacket being analized and the overlaps $\langle\psi_i|\tilde{\psi}\rangle$ at the same time.

Calculating the Fourier transform of the time series defined by real time evolution $|\tilde{\psi}(t)\rangle$ one obtains:

$$I_{\tilde{\psi}}(E,T) = \frac{1}{T}\int_0^T \mathrm{d}t \exp(iEt)|\tilde{\psi}(t)\rangle = \sum_i \exp\left(\frac{i}{2\hbar}ET\right)\mathrm{sinc}\frac{T(E-E_i)}{2\hbar}c_i|\psi_i\rangle. \tag{3.3}$$

To be able to compute the appropriate eigenvectors by the FT method some idea about its eigenenergy is necessary. The FT performed on a time series (3.3) is much more numerically involved than FT of the autocorrelation function (3.2). In both cases the most expensive part of the computation

is calculating the time series (3.1) itself, so an optimal use of the finite time interval of either time series (3.2) or (3.1) sequence has to be achieved.

The peaks whose shape is defined by the sinc function decay algebraically as $(|E - E_i|T)^{-1}$. To improve the resolution, the naive approach would be to rely on increasing the total integration time so that the tail contribution becomes small enough. Another, more advanced technique is to use the appropriate windowing function:

$$\tilde{C}_T^w(E) = \frac{1}{T}\int_0^T \mathrm{d}t w(t)\exp(iEt)\sum_i \exp(-iE_i t)|c_i|^2 = \sum_i |c_i|^2 \tilde{w}(E - E_i). \tag{3.4}$$

Windowed FT exchanges peak width for peak tail asymptotics.

Let us remind that if a function f has a FT $\mathcal{F}$, then if a FT of $f^{(n)}$ exists, it is equal to $(ik)^n\mathcal{F}$. Moreover, if f is L^1-integrable function then $\mathcal{F} \to 0$ as $E \to \pm\infty$. Widowing functions are supported on $[0, T]$ thus if windowing function vanishes on the border with power n then its $n-$th derivative is L^1-integrable and therefore $k^n\mathcal{F}(k) \to 0, |k| \to \infty$. Therefore "smoothness" class of a windowing function at boundaries translates directly to the asymptotics of the $\mathcal{F}$ tails.

Using the windowing function: $w_H(t) = \sin(t\pi/T)$ and its square w_H^2 makes asymptotics decrease faster: $(|E - E_i|T)^{-2}$ or $(|E - E_i|T)^{-3}$. We provide an exemplary analysis of a bogus quantum system in Figure 3.1.

3.1.1 Computing the eigenvectors

The vector time-series $|\tilde{\psi}(t)\rangle$ is available in the MPS form by applying a standard TEBD algorithm for evolving the states expressed in the MPS language.

Computation of the integral (3.3) reduces thanks to the trapezoidal approximating rule:

$$\int f(x)\mathrm{d}x \approx \Delta x(f(0) + f(n))/2 + \sum_{i=1}^{n-1} f(i)\Delta x \tag{3.5}$$

to a problem of performing an efficient numerical addition of Matrix Product States. The MPS representation is highly nonlinear with respect to numerical coefficients in tensors Γ and λ in equation (1.20). To be able to calculate the approximating sum (3.5) to the integral (3.3) it is enough to master addition of just two MPS vectors. Given a numerical representation of two Matrix Product States $|\psi\rangle$ and $|\eta\rangle$, the state $|\psi\rangle + |\eta\rangle$ may be represented as an MPS:

$$|s\rangle = |\psi\rangle + |\eta\rangle = \mathcal{M}(\Gamma', \lambda'), \tag{3.6}$$

where $\Gamma^{i,[k]'}(|s\rangle) = \Gamma^{i,[k]}(\psi) \oplus \Gamma^{i,[k]}(\eta), \lambda^{[k]'} = \lambda^{[k]}(\psi) \oplus \lambda^{[k]}(\eta)$. This representation is inefficient, as memory requirements grow linearly with the total number of additions. This problem is best solved by assuming that

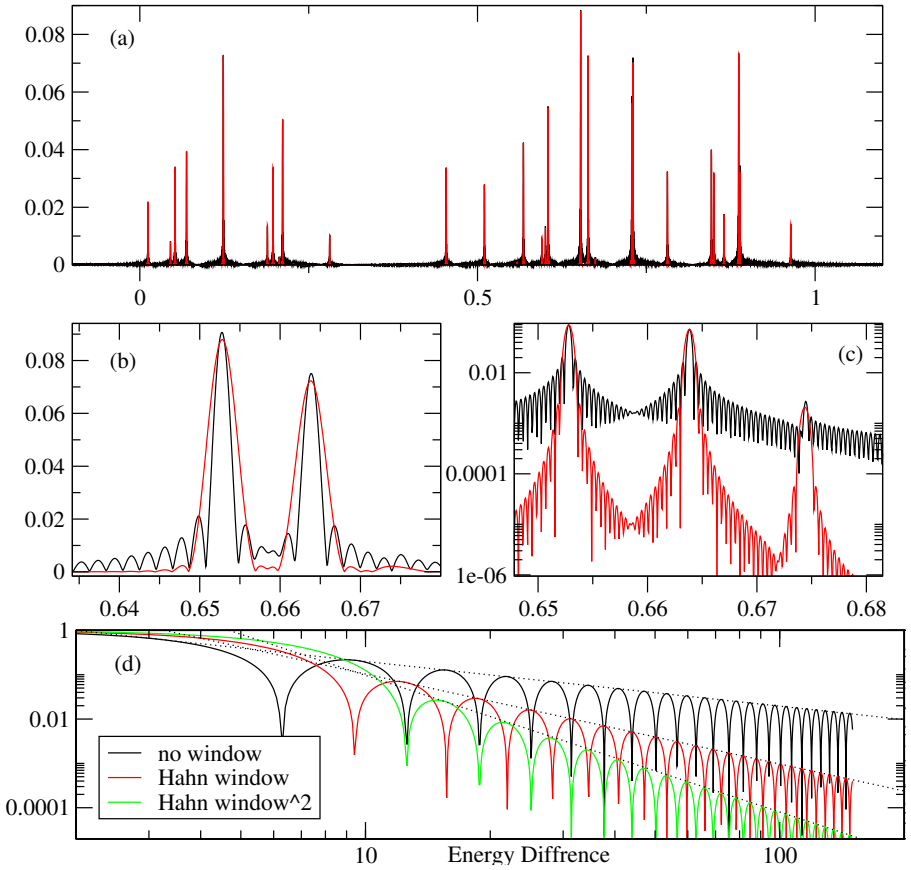

Figure 3.1: Windowing function use allows for efficient determination of the eigenenergies through Fourier Transform. In this figure, all panels show a FT analysis (Eq. 3.2) of a time series spawned by a model system (random wavepacket, random eigenvalues) is shown. Panel (a) shows overall FT for time T=15000. Height of peaks in the autocorrelation FT shown here is proportional to $|c_i|^2$. Panel (b) shows the FT of the autocorrelation function for $T = 3000$, from panel, both Hahn window, and sinc peaks are shown. Panel (c), shows plot of the modulus of the autocorrelation function in the logarithmic scale for $T = 15000$; it is clear that the Hahn window function allows for significant SNR increase. For the peak with eigenenergy $E \approx 0.675$ the SNR without windowing is of the order of 2. Using Hahn window increases this up to the order of 10^2. Panel (d) compares peak shapes for three window functions: constant, Hahn window, Hahn window squared.

we deal only with the MPS forms that satisfy the condition that families of vectors $|\psi_a^{[1\ldots i]}\rangle$ and $|\psi_\alpha^{[i+1\ldots L]}\rangle$ satisfy orthonormality conditions : $\langle\psi_\beta^{[1\ldots i]}|\psi_\alpha^{[1\ldots i]}\rangle = \delta_{\alpha\beta}$ and $\langle\psi_\beta^{[i+1\ldots L]}|\psi_\alpha^{[i+1\ldots L]}\rangle = \delta_{\alpha\beta}$. The MPS satisfying the above conditions are called to be *in the canonical form* [76].

The procedure which puts the MPS vector back in the canonical form, first computes reduced density matrices $\rho^{[1,\ldots,k]}$ and $\rho^{[k+1\ldots L]}$ for $k = 1$ and, by diagonalizing them, determines left Schmidt eigenvectors $|\psi_\beta^{[1,\ldots,k]}\rangle$. By expressing them in the basis $|\psi_\alpha^{[1,\ldots,k-1]}\rangle \otimes |i_k\rangle$ coefficients $\Gamma_{\alpha\beta}^{[k],i_k}$ and $\lambda_\beta^{[k]}$ are determined. Then k is increased and the whole procedure is repeated. After each diagonalization the truncation is performed: only first χ of 2χ singular values $\lambda_\alpha^{[k]}(|\psi\rangle)$ are kept. This is sufficient to compress the MPS representing the sum $|s\rangle$. The procedure should be repeated from $k = L$ down to $k = 1$. The second sweep ensures that all right Schmidt eigenvectors are orthonormal. Although first, left to right sweep produces set of orthonormal Schmidt vectors (left and right) at each step, discarding some Schmidt vectors while processing the next site ruins this property. Last sweep performed in reverse direction for convenience may restore this property. It is not necessary for eigenstates extraction as it does not change the state, only its representation as an MPS (tensors λ, Γ). The partial sum is not used in evolution, and abandoning the second part of the reduction saves computation time.

If after the summation (3.6), the state $|s\rangle$ is put back in the canonical form (for example by algorithm in [72]), then it turns out that sequences of $\lambda_\alpha^{[k]}(|s\rangle)$ often do not decay significantly slower than $\lambda_\alpha^{[k]}(|\psi\rangle)$ and $\lambda_\alpha^{[k]}(|\eta\rangle)$ (as α grows). This is **not** a general property of MPS state addition. This property comes from the fact that the states being added here stem from a physical time series and the sum is meant to converge to an eigenstate (which heuristically should have a simpler MPS form than the whole wavepacket containing many eigenstates).

3.2 Excitations

We consider a system formed by an ultracold atom gas in the external harmonic trap in the optical lattice potential. We assume the gas is well modelled by a single-band Bose-Hubbard model (1.9). We have implemented and applied the Fourier Transform MPS eigenstates extraction method to work on a time series obtained from unitary time evolution of the BH Hamiltonian by the TEBD algorithm.

Limited computer resources and questionable numerical stability of the TEBD algorithm demand that maximal use of finite time series length T should be made. Computing the eigenvectors by the Fourier Transform method may be shortened by using various tricks. First of all the energy of the sought after state is known, at the very least roughly, from physical

principles (for example atomic limit, perturbative argument etc). Typically even short real time evolution enables to narrow down the estimate of the energy of the state of interest by calculating low resolution spectrum (much lower than in exemplary spectrum in Figure 3.1). The problem is now to weed out the contribution of the other states with eigenenergies $E_i \neq E_{i_0}$ for which tails of the functions $\tilde{w}(T(E-E_i))$ may give a serious contribution to impurities present in the extracted state.

Already discussed method was to choose the windowing function so that contributions (of magnitude $|c_i \tilde{w}(T(E-E_i))|$) of other eigenstates with energies E_i were negligible. If the initial guess for the energy of the wanted eigenstate is accurate up to ΔE then performing the wave function integration $I_{|\tilde{\psi}\rangle}(\frac{\hbar}{\Delta E}, E)$ gives a new initial wavepacket with enhanced contribution of $|\psi_i\rangle$. It also helps the numerical efficiency of the TEBD algorithm — the fewer eigenvectors the wavepacket contains the more stable dynamics it seems to initialize.

In the physical applications often one may encounter peaks that correspond to almost degenerate energy levels (for example due to a slightly broken symmetry). In such a case often the two energy levels are very close to each other, demanding long integration time T to separate the peaks. If estimation the small energy difference ΔE is possible, then performing the FT integration for time $T_s = \frac{2\pi\hbar}{\Delta E}$ enables one to exactly nullify the contribution form the other, "undesired" eigenstate. If the time ΔE is not known with high enough precision then the contribution of the other state is not exactly zeroed, but can be expected to be significantly smaller than those of the extracted state (say by a factor of $\gamma \ll 1$). Then the n-fold repetition of such a procedure, each time starting the time evolution from the current approximation for the extracted eigenstate, reduces the contribution from the other state by a factor γ^n. Mathematically in first step one obtains an approximation $I_{|\tilde{\psi}\rangle}(T_s, E)$, after second step $I_{I_{|\tilde{\psi}\rangle}(T_s,E)}(T_s, E)$, then $I_{I_{I_{|\tilde{\psi}\rangle}(T_s,E)}(T_s,E)}(T_s, E)$ and so on.

All in all we are able to weed contribution of states that have eigenenergy much different than the sought after eigenstate with just one step. Moreover we may manually delete contribution of a particular undesired eigenstate which is close in the energy to the target state.

The ground state in Mott insulating regime $U/J \gg 1$, in presence of the external trap, has a well known "wedding-cake" spatial structure as shown in Figure 3.2, panel (a). We have considered two physical processes which deal with ultracold atom gas in the harmonic trap and lead to excitations: ramping up the lattice potential and explicit time-periodic modification of the optical lattice potential - the modulation spectroscopy.

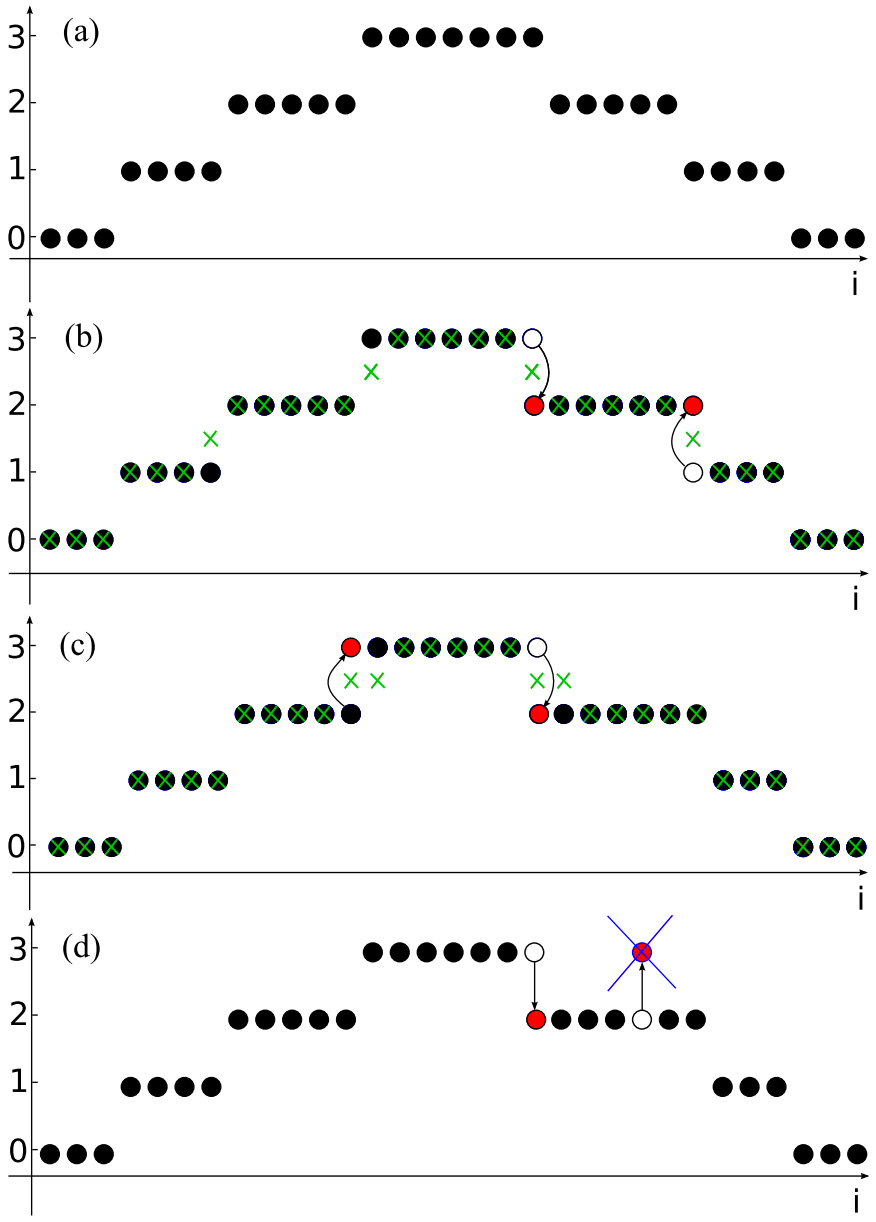

Figure 3.2: The wedding cake structure of the occupation of lattice sites in no tunnelling ($J = 0$) regime, (see Eq. (1.9)). Panel (a) shows the Fock state, the ground state. Panel (b) shows symmetrised low energy excitation occupation (jumping of particle from one to other level MI boundary). Panel (c) shows particle transfer to the same level. Panel (d) shows excitation that do not appear as a result of a slow quench. See Section 3.2.1 for a detailed discussion. The assumed potential is symmetric, $r_0 = 0$ in Eq. (3.7). Image from [119].

3.2.1 Excitations while ramping up the lattice potential

In the Florence experiment [10] a boson gas was prepared in the harmonic trap with the optical lattice potential switched off. The final goal of this experiment was to prepare a so-called Bose-glass phase, that requires reaching a ground state of the deep optical lattice potential of height s_1 with an additional optical lattice potential of height $s_2 \ll s_1$ with incommensurate wave length, introducing the disorder. All in all inclusion of these potentials reduces to adding to the Hamiltonian a local chemical potential Hamiltonian term of the form $\sum_i \epsilon_i n_i$ with ϵ_i given by (1.10) and additional trapping potential:

$$\epsilon_j = c(j - r_0)^2 + s_2 \sin^2\left(\frac{\pi j \lambda}{\lambda_2} + \phi\right). \tag{3.7}$$

Note that the trap center position r_0 does not need to coincide with the minimum of the optical lattice (r_0 is not necessarily integer). The quotient λ/λ_2 has to be "irrational enough" so that the disorder was a good imitation of a truly pseudorandom sequence.

Ramping the lattice slowly enough, with gas initially in the ground state, was predicted to enable to reach a ground state of the final optical lattice potential [10]. As the alleged final state, the BG has no gap, serious questions about the adiabaticity may be posed, as it is the energy gap which is a necessary requirement for the adiabatic theorem to hold [125]. The numerical simulations showed that the higher the disorder potential, the less overlap on the true ground state one should expect [122].

If there is no external disorder, and the optical lattice is deep, the wedding cake profile (see Figure 3.2) allows for several mechanisms for excitations: high-energetic particle-hole excitation, low-energetic excitation in the superfluid interfaces, low energetic excitation based on displacing particles from one Mott Insulator plateau to another. Authors of [122] observed low energy excitations and enlarged particle number variation in the SF interfaces as compared to the ground state.

The process of ramping the optical lattice has been simulated using the BH Hamiltonian. In the experiment [10] optical lattice potential was increased from 0 to $16E_R$. In the theoretical analysis this was represented by an increase from 0 to $14E_R$. This modification allowed to roughly include J and U constants renormalization which takes into account virtual excitation to higher Bloch bands, as described in detail in Section 4. In the simulations U and J parameters are computed by the BH model formulas (1.8). In the actual simulations the very initial phase — rise from 0 to 4 E_R was assumed perfectly adiabatic. The initial state evolution for $s \in [0, 4]$ may not be modeled by the BH Hamiltonian (next-nearest and subsequent tunnelling terms are not negligible). This stage is assumed instead to be perfectly adiabatic and the simulation was in the end performed from $s = 4E_R$ to $s = 14E_R$

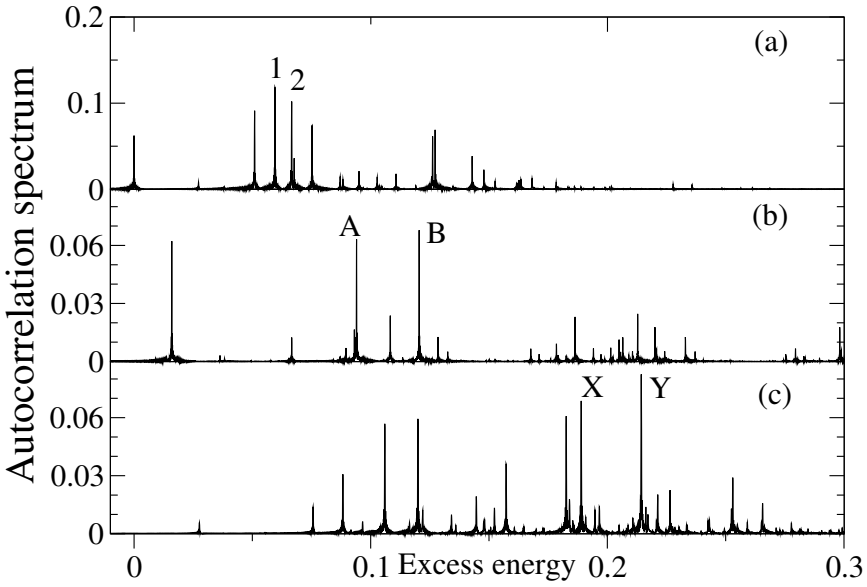

Figure 3.3: Autocorrelation spectra, Eq. (3.2), obtained dynamically for s=14 E_R after switching on the optical lattice, for disorder strengths s_2= (a) 0 E_R, (b) 0.4375 E_R, (c) 2.1875 E_R. All parameters are taken to approximate the experimental situation [10]. The energy levels of the system appear as peaks (origin at the zero-point energy), with height $|c_i|^2$ from eigenbasis expansion. Peak labels are for further reference. Image from [119].

using the exponential ramp with the ground state for $s = 4E_R$ as the initial state. The total ramp time was 100 ms. The autocorrelation function (3.2) for the final wavepacket was computed already in [122]. We have used that result as a starting point of our analysis.

From the autocorrelation function presented in Figure 3.3 we have chosen most contributing eigenstates and calculated them as described in Section 3.1.1.

First let us discuss the case where the additional lattice of height s_2 generating the disorder is not used. The excess energy brought by nonadiabatic preparation is small. As seen in Figure 3.4, excitations take place close to the SF regions: these are transfers of a single atom from an edge of one Mott plateau to another edge of perhaps different Mott plateau. The particle-hole excitations, which are typical for a insulating homogeneous system (without the trapping potential) are absent. Indeed their excitation energy would be of the order of U which several times larger than typical energy of excitation present in the wavepacket.

We have found that description of the system presented in [126] is not confirmed by numerics. There the ground state was assumed to be contaminated by local particle-hole excitations. Melting of the MI [127] scenario

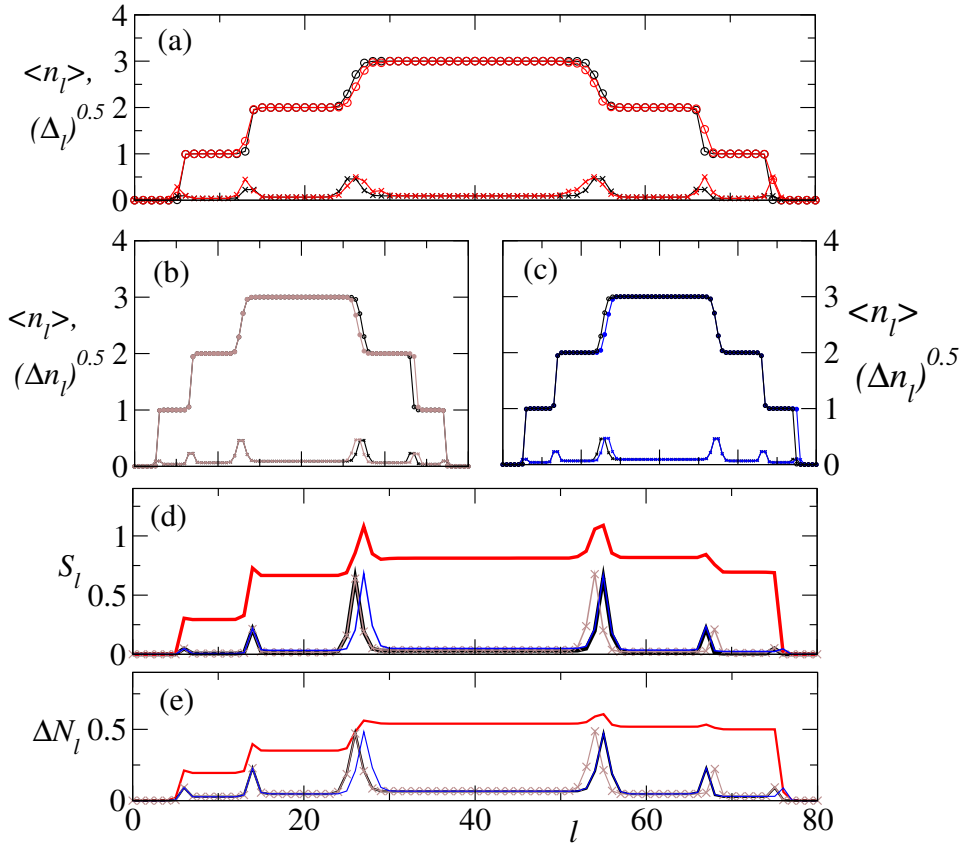

Figure 3.4: Properties of states of the trapped BEC in a deep optical lattice (s=14), without disorder (s_2=0), r_0=35.12345 in Eq. (3.7). The black thick line refers to the ground state, the red thin line to the dynamically prepared wavepacket, the brown (with crosses) and blue lines to the two excited states with the largest populations denoted as 1 and 2 in Figure 3.3(a). (a), (b), (c): Average occupation number $\langle n_l \rangle$ and standard deviation of number of atoms $\sqrt{\Delta_l} = \sqrt{\langle n_l^2 \rangle - \langle n_l \rangle^2}$ on each site for the wavepacket and the two eigenstates. (d): Entanglement entropy, Eq. (1.16); almost zero in the Mott plateaus for eigenstates - implying their approximate separability; large for the wavepacket. (e): Variance of the number of atoms to the left of site l. Image from [119].

seems more accurate.

The wavepacket (see Figure 3.4) is characterized by small local number of particles variance Δn_l in Mott phases. However Δn_l in the regions between MI plateaus is much larger than in the SF regions of the ground state. Nevertheless the difference is not very pronounced.

More substantial difference may be observed when comparing the entanglement entropy S_l of a bipartition of a whole lattice $\{1, \ldots, L\} = \{1, \ldots, l\} \cup \{l+1, \ldots, L\}$. For the eigenstates, it essentially vanishes in the MI regions and shows small peaks in the SF regions. For the wavepacket, on the contrary, the entanglement entropy S_l is large in the Mott regions as well. The wavepacket is a sum of simple eigenstates that differ by long range displacement of particles between the SF regions. This creates substantial entanglement for the bipartition into "left" and "right" parts. The same may be stated about dislocations of particles between SF interfaces.

The entanglement entropy is large over the MI regions for the wavepacket because in contrast to simple eigenstates, the wavepacket does hot have well defined number of particles in "left" and "right" part of the system (assuming that the bipartition is taken w.r.t to the site belonging to the MI plateau). Indeed, variance of a quantity $N_l = \sum_{i=0}^{l} \hat{n}_i$, clearly distinguishes the two cases (see panel (e) in Figure 3.4). In case of the eigenstate we have $\Delta N_l \approx \Delta n_l \ll 1$, while for the wavepacket ΔN_l is of the order of unity. If statistics of such a quantity could be measured experimentally, it would prove a way to detect lack of adiabaticity.

In the regime of deep disorder ($s_2 = 2.1875 E_R$) the ground state is a BG phase with no visible "levels" of the "wedding cake" structure. The whole sample is characterised by rapid changes of integer occupation of different sites. The autocorrelation function of the resulting wavepacket is shown in Figure 3.3. We have computed several eigenstates. The exemplary excitations are shown in Figure 3.5. We have found that most contributing eigenstates are again BG states differing from the ground state by moving single particles form one site to the other. The different sites still have a quasi random integer occupation and seem identical in nature to the ground state. Excitations effects are local. However the particle dislocations again may be long distance, proving to be a serious obstacle to adiabaticity. The entanglement entropy computed for eigenstates is small, except in small random, isolated SF intervals. This is in great contrast to the full wavepacket which has large entanglement entropy and site occupation variance Δn_l, with numerous peaks indicating melted regions.

3.2.2 Excitations by modulation spectroscopy

One of the standard methods of analysis of complex quantum systems is so-called modulation spectroscopy, that is study of energy absorption by

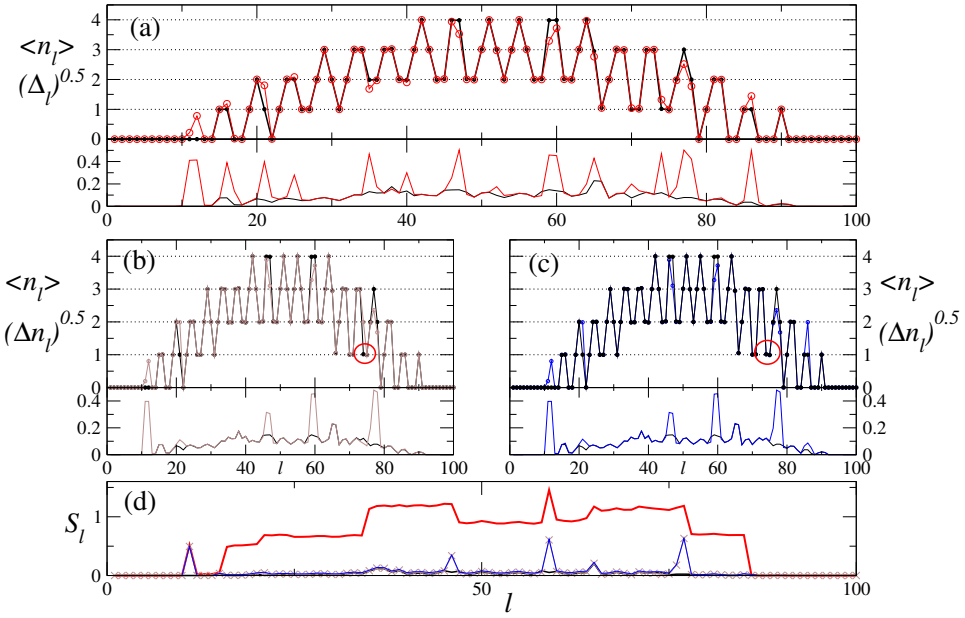

Figure 3.5: Properties of states of bosons trapped in a deep optical lattice (s=14) in the presence of strong disorder s_2=2.1875. Here r_0=50.1075 and ϕ=0.0304 in Eq.(3.7). Brown, blue lines correspond to excitations X and Y in Figure 3.3(c). Again the plots show the average occupation of lattice sites and the standard deviation $\sqrt{\Delta_l} = \sqrt{\langle n_l^2\rangle - \langle n_l\rangle^2}$. The entanglement entropy S_l is larger for the dynamically created wavepacket than for stationary states, and Δ_l has many more peaks, indicating a significant melting of the Bose glass. Image from [119].

the system as a function of frequency of external modulation of the system. This may allow for detection of the gap and determining that the system is in an insulating phase as in [10].

We have considered a fairly deep optical lattice of depth $s = 12E_R$ [128], closer to the tip of the SF-MI transition. We have chosen the ground state as an initial state. It has greatly pronounced SF regions separating the Mott plateaus (see a ground state occupation simulation in Fig 3.6). Therefore excitations are likely to occur also in large part in the superfluid regions. The absorption spectrum contains two structures around $\omega/U \approx 1$ and $\omega/U \approx 2 - 2.3$ in parallel to the experiment results [129]. The excitations with energy U are pure particle-hole Mott Insulator excitations, and were an expected feature, as they proved existence of the MI. The other structure has been more of a mystery. It was claimed [128] to correspond to high energy

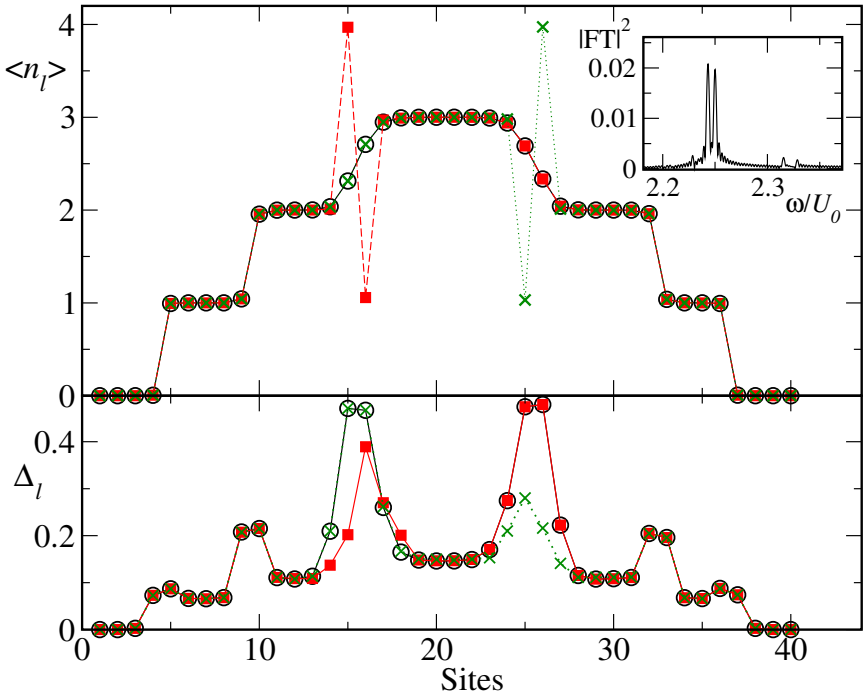

Figure 3.6: Black circles: average occupation number for the ground state of 65 particles in a lattice with depth $s = 12$ (40 sites) and a harmonic trap with curvature $c = 0.006$, centered around $r_0 = 20.62345$ (to separate left and right excited states w.r.t. to the trap center). The filled red squares connected by a dashed line and the green crosses connected by a dotted line show occupation numbers for two extracted excited states showing a particle-hole excitation in the SF region. The excess energies (energies measured with respect to the ground state energy) of the states are $\Delta E/U_0 = 2.2502$ (resp. $\Delta E/U_0 = 2.2434$) for the "red squares" (resp. "green crosses) in excellent agreement with the positions of two closely spaced peaks in the FT of the autocorrelation function shown in the inset. The lower panel shows the standard deviation of the occupation number on each site, for the ground state (open circles) and the excited states, the latter shows reduced fluctuations. Image from [119].

particle-hole excitation in the superfluid interface connecting the two MI phases.

To prepare the wavepacket for analysis we introduce a modulation of optical potential height with time, that is $s(t) = s_0 + s_m \sin \omega t$. The wavepacket obtained for a given frequency, at the end of the modulation, is a starting wavepacket for our eigenstates extraction procedure. The strong 20% modulation, which was used in [128], leads to a "too excited" wavepacket. Although the final wavepacket is converged, the subsequent evolution needed for for a high-resolution FT is impossible for the TEBD algorithm to handle (see, however, a discussion in Section 3.3). We expect that most significantly excited states do not depend on the strength of the modulation. However for strong modulation we leave the perturbative regime and the absorption curve is nontrivially modified. That is why we decided to use a more subtle modulation with a smaller (1.67%) amplitude.

We restrict for brevity on the wavepacket modulated with frequency $\omega/U_0 \approx 2.3$. As before we compute the autocorrelation function of the real time unitary evolution, then perform its FT. The inset of Figure 3.6, shows the relevant section of the spectrum, where two close peaks are present. The Figure 3.6 shows also the average occupation and its variation for the two excited states. Indeed, these states are definitely a particle-hole excitation in the SF region as suggested by [128]. Curiously the variation $\Delta_l = \langle \hat{n}_l{}^2 \rangle - \langle \hat{n}_l \rangle^2$ in the relevant region is much lower for the excited eigenstate. This means that the excitation is of "Mott insulator"-type and the SF character is destroyed.

Other states populated as a result of the modulation may also be extracted. For example particle-hole excitations within the MI phase may be successfully targeted.

3.3 Limitation of the method

The main limitation of the FT eigenvector extraction is set by the stability of the time-evolution of the wavepacket by the TEBD algorithm. In dynamical situations there is no analogue of the area laws and the entanglement entropy typically grows linearly with time. This translates to the emergence of strong entanglement across the sample and failure of the MPS ansatz. Therefore only a short time-series data is available for analysis. The exceptionally stable evolution may be reached if physical arguments motivate it. For example we have observed, that numerical evolution of wavepackets that proved later to contain only a handful of eigenstates apparently could be continued indefinitely. Such wavepackets typically stem from gentle evolution of an initial state close to the eigenstate (such as semiadiabatic quench of the ground state).

Unitary evolution preserves the norm of the wavevector and the average

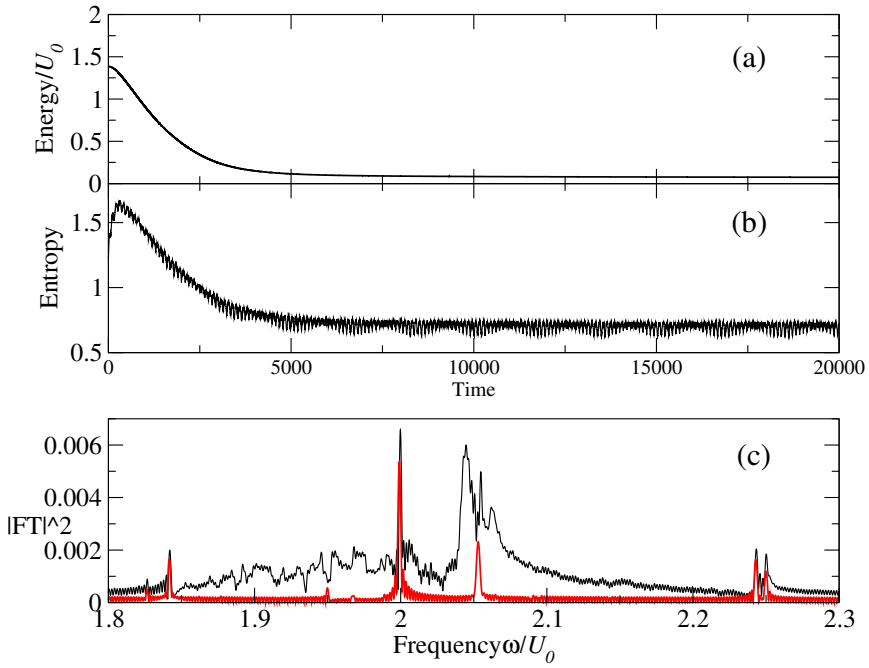

Figure 3.7: Long time evolution of a wavepacket prepared by a modulation at frequency $\omega/U_0 = 2$ and then evolved with the TEBD algorithm. The excess energy over the ground state is plotted in top frame (a). It is not conserved but, after the initial drop, it stabilizes. Similar behaviour occurs for the entanglement entropy (b), with additional oscillations because the wavepacket is a sum of relatively few localised states. The FT of the autocorrelation function (c) does not display any clear peaks if performed in the [0,5000] time interval (black thin line), but definitely shows several well defined excited states over the time interval [15000,20000] (thick red line). Image from [119].

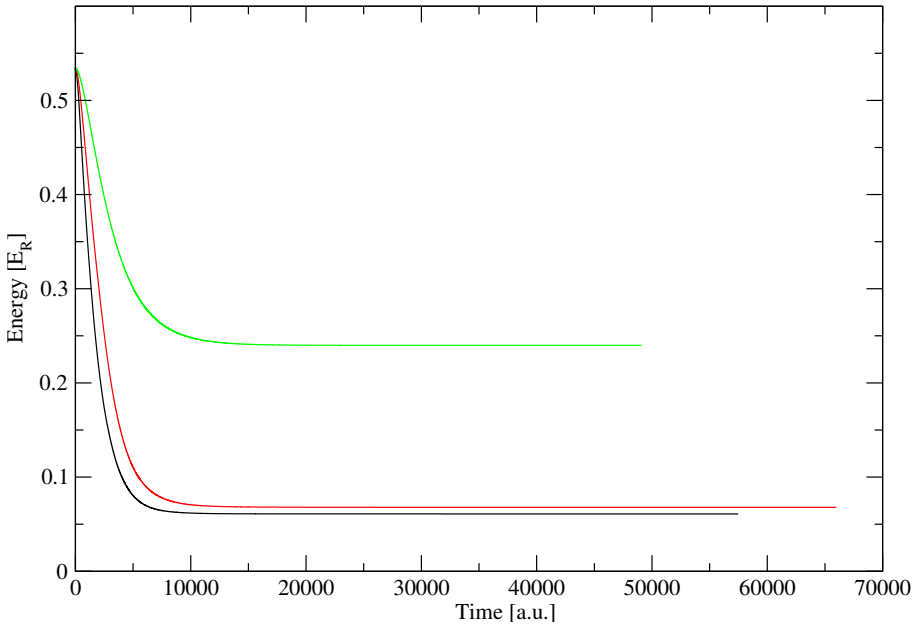

Figure 3.8: The expected energy of the evolved test wavepacket $E(t) = \langle\psi(t)|H|\psi(t)\rangle$. The test wavepacket is a $N = 12$ particle ground state of a BH Hamiltonian in $L = 12$ lattice sites. The evolution is performed under different trap curvature (for details see text). Non-conservation of energy is due to too small bond dimension χ in the MPS form (Eq. 1.20 and following discussion) and is purely a numerical effect. Stabilization of energy hints that after initial "decay", the remaining part of the evolution is unitary again.

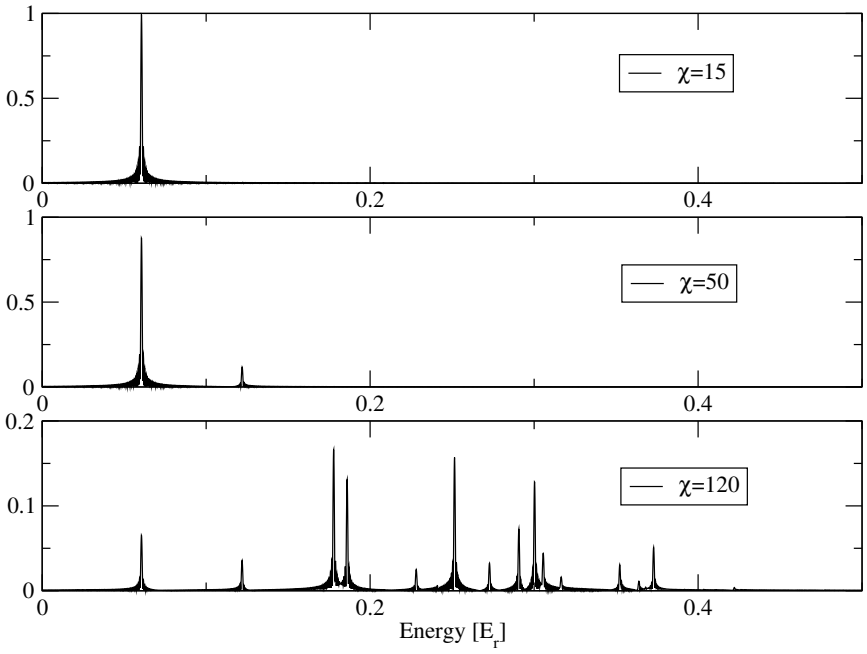

Figure 3.9: Autocorrelation spectra of final wavepacket obtained as in Figure 3.8. Wavepackets taken after $t = 20000$ units have been used. Clearly the higher the bond dimension the more additional eigenstates make it into the final wavepacket.

of the energy of the wavepacket. Any loss of the norm and variation of the energy w.r.t to the time is a sign of a numerical instability. This may arise due to the numerical errors in the time-discretization of the $\exp(iHt)$ and truncation performed during reexpressing the wavevector after the two-site operator $\exp(iH_{even/odd}\delta t)$ as an MPS with bond dimension χ (for more details see Section 1.3). Representing excited states may require a higher bond dimension χ than the ground state. The numerical computation suggests, that if χ is sufficient for expression of the ground state but not for other eigenstates, the overlap of a wavepacket over the "more complex" eigenstates decreases in with time, while magnitude of projection of a wavepacket to stable eigenvectors remains constant.

To back these claims with computation we have considered a small system within a shallow a shallow lattice with $\kappa = 0.01$ consisting of 15 particles in $L = 10$ sites. Here lattice depth is $s = 5E_R$ and in perpendicular direction $s_\perp = 12.5E_R$ for which $U/J \approx 2$ and the system is deep in the SF phase. The initial state is a ground state of such system but calculated for $\kappa = 0.0045$. Definitely the initial state is far from the ground state. Figure 3.8 shows the evolution of the expected value of energy of the state as a function of evolution time for different $\chi = 15, 50, 120$. Clearly the higher

the bond dimension the higher the value at which the energy as a function of time saturates. Note that the perfect stability of TEBD implies that the energy is constant, there should be not drop altogether. Figure 3.9 shows the FT of the final wavepackets correlation function. It is clear the higher χ the more eigenstates remain in the wavepacket.

Similar situation occurs in the large systems that have been studied. The FT of the autocorrelation function (see Figure 3.7) of the wavepacket considered in the modulation spectroscopy analysis over the time interval [0, 5000] displays a myriad of different structures. Evolving the wavepacket numerically using the TEBD algorithm, under time-independent Hamiltonian to obtain a FT of the autocorrelation function for the time interval [15000, 20000] gives only a handful of sharp peaks at some frequencies. During the course of evolution, a *self-purification* of the wavepacket occurs with the non-converged fraction seemingly disappearing. No noticeable artifacts after the purification shows that the following numerical evolution is unitary.

Chapter 4

Higher bands - Effective BH Hamiltonian [92]

In previous sections the single band Bose-Hubbard hamiltonian has been used to model the ultralcold gas of bosons. It has been hinted in Sections 1 and 3.2.1 that inclusion of higher band is necessary for good quantitative agreement of result.

The multiorbital BH Hamiltonian (1.6) describes exactly the physics of the ultracold atom gas in the optical lattice potential. However, it is prohibitively difficult to apply due to the large dimension of the local Hilbert space. In this thesis we use separable lattice potentials, thus single particle energy levels are characterised by triples of indices $(\alpha_x, \alpha_y, \alpha_z)$ where α_i enumerate one dimensional eigenfunctions in the relevant direction $i = x, y, z$. Restricting all α_i to take values of $1 \dots B$ gives us a total of B^3 single-particle basis states. The local Hamiltonian which governs the physics in the single site is $\mathcal{H}_{loc}$:

$$\mathcal{H}_{loc} = \sum_{i,\alpha} E_i^{\alpha} n_i^{\alpha} + \underbrace{\frac{1}{2} \sum_{\alpha,\beta,\gamma,\delta} U_{ijkl}^{\alpha\beta\gamma\delta} (a_i^{\alpha})^{\dagger} (a_i^{\beta})^{\dagger} a_i^{\gamma} a_i^{\delta}}_{\mathcal{H}_{int}} . \tag{4.1}$$

The local dimension d of the n-particle problem restricted to the lowest B bands is $d = \binom{B^3+n-1}{n}$. Its dimension is a key parameter on which the computational speed of the DMRG and TEBD algorithms depends.

If one considers slow dynamics or a static situation, then it is expected that it suffices to include in the theoretical description only the low energy subspace. In the ordinary BH model (1.9), only states truncated to the lowest band are included and n-particle state $(a_0^{\dagger})^n |\Omega\rangle$ is fully characterised by the value n, hence the total dimension of local Hilbert space is $n_{max} + 1$.

Authors of [38] proposed to base the choice of the relevant Hilbert space on this simple property. They proposed diagonalizing a single site $n-$particle

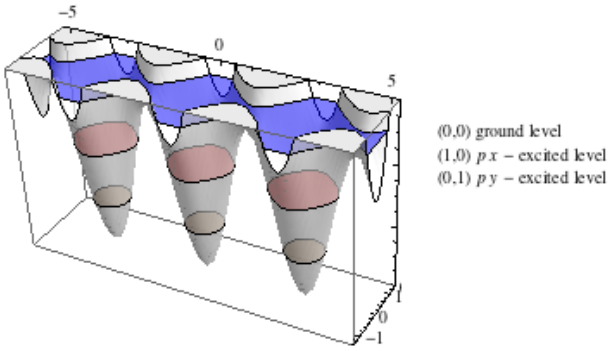

Figure 4.1: The optical potential with schematic energy levels (an analogous 2D case). The lowest Bloch band and excited band in the direction along the optical lattice are described by localised Wannier functions. The excitation in transverse direction consists of delocalised states, but are excluded as their energy is too high.

	$B=1$	$B=3$	$B=5$	$B=7$	$B=9$
$n=2$	1	378	7875	58996	266085
$n=4$	1	27405	10668000	586862710	11864996235

Table 4.1: The dimension of the local Hilbert space as a function of number B of Bloch bands included in each direction and total number of particles. This signifies the difficulty of direct diagonalization of the Hamiltonian $\mathcal{H}_{loc}$ and lack of any possibility of application of the DMRG techniques to the MBH Hamiltonian Eq. (1.6) in its full form.

Hamiltonian to obtain a $n-$particle interacting ground state of $\mathcal{H}_{loc}$. Then one should construct a single site Hilbert space for the lattice as one spanned by the interacting ground states with a different total number of particles (ranging from 0 to n_{max}). Although the states are characterised solely by n, there is no notion of a single particle mode. In the position representation these states are not separable. It was shown [130] that separable states do not describe the ground state of $\mathcal{H}_{loc}$ very efficiently.

Changing the local Hilbert space basis from a full Fock space to the proposed subspace, necessarily leads to renormalization of parameters of the Bose-Hubbard Hamiltonian. The "traditional" interpretation of J an U parameters of the Bose-Hubbard Hamiltonian (1.9) was "tunnelling amplitude" and "pair interaction energy". In the following we show how to define relevant parameters and how to interpret them in the new basis.

To define renormalized values of the interaction energy U per particle,

the eigenenergy ϵ^n should be expressed as a sum of interaction energy (which in case of the BH model, is just $\frac{U}{2}n(n-1)$) and a single-particle energy. The most natural way to define the interaction energy would be then to use:

$$U_{int} = \frac{U_n}{2}n(n-1) = \langle\psi_0^n| \sum_{\alpha\beta\gamma\delta} U^{\alpha\beta\gamma\delta}\hat{a}_\alpha^\dagger\hat{a}_\beta^\dagger\hat{a}_\gamma\hat{a}_\delta|\psi_0^n\rangle. \tag{4.2}$$

This definition corresponds to $U_{int} = \int \psi^*(x_1,\ldots,x_n)V_{int}\psi(x_1,\ldots,x_n)$.

Unfortunately, U_n cannot be defined in such a way if we request the final effective Hamiltonian to have a form resembling Eq. (1.9) and expect it to have a physical content well approximating that of the Hamiltonian (1.6). That is because in $\mathcal{H}_{loc}$ the single particle energy is no longer a function of n, but it depends on distribution of n particles over different Bloch bands. Therefore the only way to have a description solely by the site total occupation is to include a "single particle energy" contribution in the definition of new U parameters. All in all we define new U_n parameters as:

$$\epsilon_0^n = \frac{U_n}{2}n(n-1) + nE_0. \tag{4.3}$$

Although technical, this point is of utmost importance. In the original BH model, the U parameter is interpreted only as an interaction parameter. The single particle energy is included in the global chemical potential and is later disregarded as it gives just a constant term in the canonical ensemble). In the new approach it is related to the "total local energy". For the single band BH model, we have $U_n = U_{BH}$. Often dependence on n of the sequence U_n is weak and may be considered linear: $U_n = U_2 - (n-2)W, W \ll U_2$

Statements such as "energy gap in Mott Insulating phase, in atomic limit is U" in fact do not refer to the "interaction energy" meaning of U but rather the "total energy", as energy gap is difference of "total energies" of states (and chemical potentials cancel out). Thus U no longer quantifies "interaction" but it still measures the gap and particle hole excitation energy (For further details, see Section 4.3 and Appendix 9.3).

The second stage is to renormalize the inter-site couplings. If only a single band model is considered, the interaction term U_{iiij}^{0000} induces an interaction term, which acts just as hopping term proportional to density: $U_{iiij}^{0000}a_i a_j^\dagger(n_i + n_j - 1) + H.c.$ in the effective Hamiltonian (called bond-charge term in [38, 131]). The couplings by ordinary kinetic operator have also to be modified, as the states spanning local Hilbert space are modified [38]. The new, renormalized tunnelling parameters also become density-dependent (even if obviously density dependent U_{iiij} terms are not included), as the interacting $n+1$-particle eigenstate of $\mathcal{H}_{int}$, the $|n+1\rangle_{\mathcal{H}_{int}}$ does not differ from the interacting eigenstate $|n\rangle$ by action of any of operators $(a_i^\alpha)^\dagger$:

$$J_{n_i,n_j}^{MO} = \frac{1}{\sqrt{n_i(n_j+1)}}\sum_\alpha J_\alpha\langle j, n_j+1|(a^\alpha)^\dagger|j,n_j\rangle\langle i,n_i-1|a^\alpha|i,n_i\rangle. \tag{4.4}$$

In the above formula $|i,n\rangle$ denote interacting $n-$particle ground states. If the usual Fock states are used just as in the BH model, then $J_{n_i,n_j} = J_0$. The full tunnelng amplitude J_{n_i,n_j} contains also the bond-charge term that is

$$J^{BC}_{n_i,n_j} = \frac{\langle n_i - 1, n_j + 1|\frac{1}{2}U^{\alpha\beta\gamma\delta}(a^{\alpha}_j)^{\dagger}(a^{\beta}_i)^{\dagger}a^{\gamma}_i a^{\delta}_i|n_i, n_j\rangle}{\sqrt{n_i(n_j+1)}(n_j + n_i - 1)}. \tag{4.5}$$

The full, density-dependent tunnelling amplitude is then $J_{n_i,n_j} = J^{MO}_{n_i,n_j} + J^{BC}_{n_i,n_j}(n_i + n_j - 1)$.

The tunnelling parameters J^{α} are much higher for particles occupying the higher bands. The interacting n-particle states differ from the BH basis just by smearing the distribution of particles over higher bands. Therefore the tunnelling parameters are expected to increase.

The effective multiorbital (EMO) Hamiltonian finally becomes:

$$\mathcal{H}_{EMO} = -\sum_{\langle i,j\rangle} a_i a^{\dagger}_j \sum_{n_i,n_j} J_{n_i,n_j} P^i_{n_i} P^j_{n_j} + H.c. + \sum_{n,i} \frac{U_n}{2} n(n-1) P^i_n, \tag{4.6}$$

where $P^i_n = |i,n\rangle\langle i,n|$. Here the creation operators a_i are **defined** by the requirement that $a_i|n,i\rangle_{\mathcal{H}_{int}} = \sqrt{n}|n-1,i\rangle_{\mathcal{H}_{int}}$. In particular it is **not** true that $a_i = a^0_i$. Nevertheless operator $n_i = a^{\dagger}_i a_i$ correctly counts the total number of particles within a single site.

The plots Figs 4.2 and 4.3 show the dependence of the new density-dependent J and U parameters on the optical lattice depth as compared to the BH parameters.

The accurate determination of constants U_n and J_{n_1,n_2} has to be addressed throughly before any serious application of the new effective model. However this point is essentially a solution of a de facto numerical-mathematical problem (although physical arguments are required to solve it). As many numerical problems this problem is subject to continuous improvements of accuracy and efficiency. Thus we have been able to obtain a serious improvement over the solution proposed in the original work [38]. Detailed description of this point is given in the Appendix 9.4.

4.1 Gutzwiller ansatz analysis of the Multiband effective Hamiltonian

A homogeneous (without the external trap) lattice Hamiltonian may studied in the thermodynamical limit by means of the Gutzwiller ansatz (for details see Section 1.4.3). The multiorbital Hamiltonian Eq. (4.6) may also be analyzed with this method. As the multorbital model is of essentially of the same form as the Bose-Hubbard model (1.9), with similar interpretation of its terms, and its purpose is to describe systems which were quite successfully

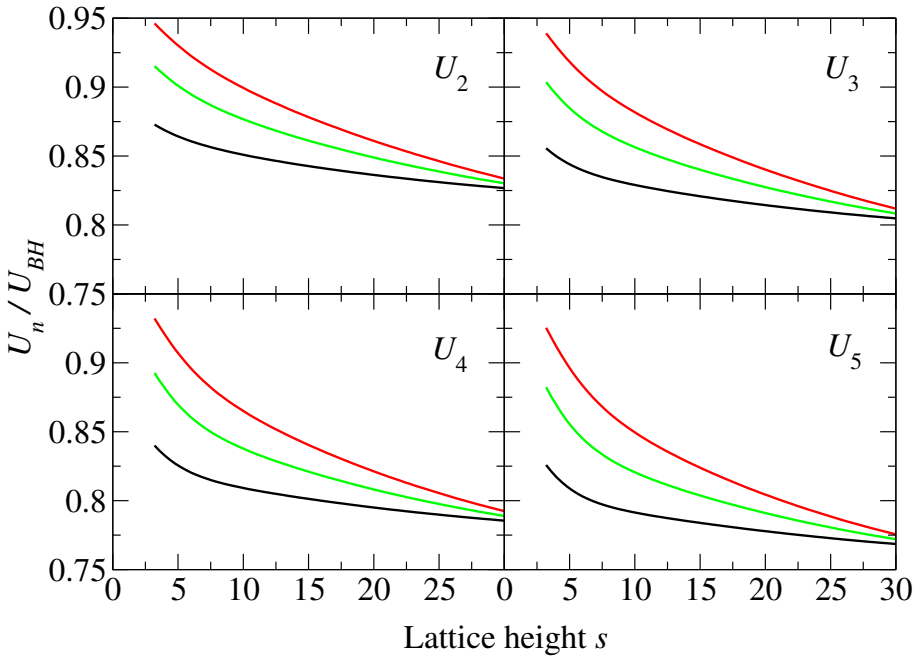

Figure 4.2: Renormalized interaction parameters U_n vs. height of the optical lattice potential, for different dimensionalities: black, green, and red lines corresponding to 1D, 2D, 3D, respectively. Interaction and lattice parameters: $2a_s/\lambda = 0.014, \lambda = 754$ nm. The transverse lattice depth is $s_\perp = 34.8$. The curves meet at $s = s_\perp$. Image from [92].

described by the BH model, we expect existence of the same phases that is MI, SF phases, characterised by integer site occupation and nonzero SF order parameter $\langle a \rangle$ respectively. Experimental results call for an accurate locating the phase boundary between MI and SF phases in terms of optical lattice depth s, a key experimental parameter.

In the MO Hamiltonian, the dependence of interaction parameters on the dimensionality of the optical lattice is nontrivial. We use the data for J_{n_i,n_j} and U_n for configuration as described in Figure 4.2, that is $2a_s/\lambda = 0.014, \lambda = 754$ nm. The transverse lattice depth is $s_\perp = 34.8$. The Gutzwiller mean field approach applied to the effective Hamiltonian (4.6) reduces to finding the global minimum of the following functional:

$$\begin{aligned} E_{EMO}[\psi] &= -2z \sum_{n_1,n_2} J_{n_1,n_2} \langle\psi|a_i|n_1\rangle\langle n_1|\psi\rangle\langle\psi|a_i^\dagger|n_2\rangle\langle n_2|\psi\rangle + \\ &+ \sum_n \frac{U_n}{2} n(n-1)|\langle\psi|n\rangle|^2 - \mu \sum_n n|\langle\psi|n\rangle|^2. \end{aligned} \tag{4.7}$$

In the mean field approximation to the Hamiltonian (1.9) the dimensionality of the lattice enters the solution only by the coordinate number z. If

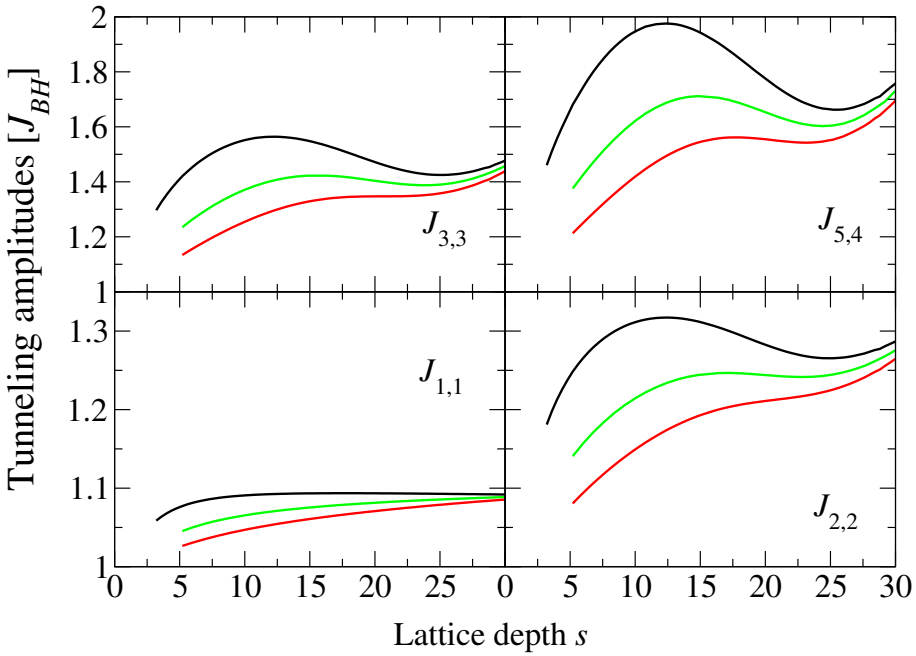

Figure 4.3: Renormalized tunnelling amplitudes J_{n_1,n_2} vs. height of the optical lattice potential, for different dimensionalities: black, green, and red lines corresponding to 1D, 2D, 3D, respectively. Interaction and lattice parameters: $2a_s/\lambda = 0.014$, $\lambda = 754$ nm, $s_\perp = 34.8$. The curves meet at $s = s_\perp$. Image from [92].

the considerations are performed as a function of Jz/U then the results are lattice geometry-independent. In the effective model for the EMO Hamiltonian a single notion of J nor U is present. Instead of choosing arbitrary coefficients we have decided to plot the phase diagram of the EMO Hamiltonian as a function of $J_{BH}(s)/U_{BH}(s)$. That is for several values of s we determine phase in which the system may be found and associate that information with a point $(J_{BH}(s)/U_{BH}(s), \mu/U_{BH}(s))$. The resulting phase diagram may be seen in Figure 4.4. It is evident that mean field phase diagram is dimension dependent in a matter different than the ordinary BH Hamiltonian. Moreover it is evident that MI lobes are smaller making it more difficult for an insulator phase to exist.

4.2 DMRG analysis of the Multiband effective Hamiltonian

In a 1D lattice, the mean field approximation applied to description of the Bose-Hubbard model is inaccurate [61, 81]. Therefore the MPS ansatz was used. The energy minimization was perfored using the Time Evolving Block

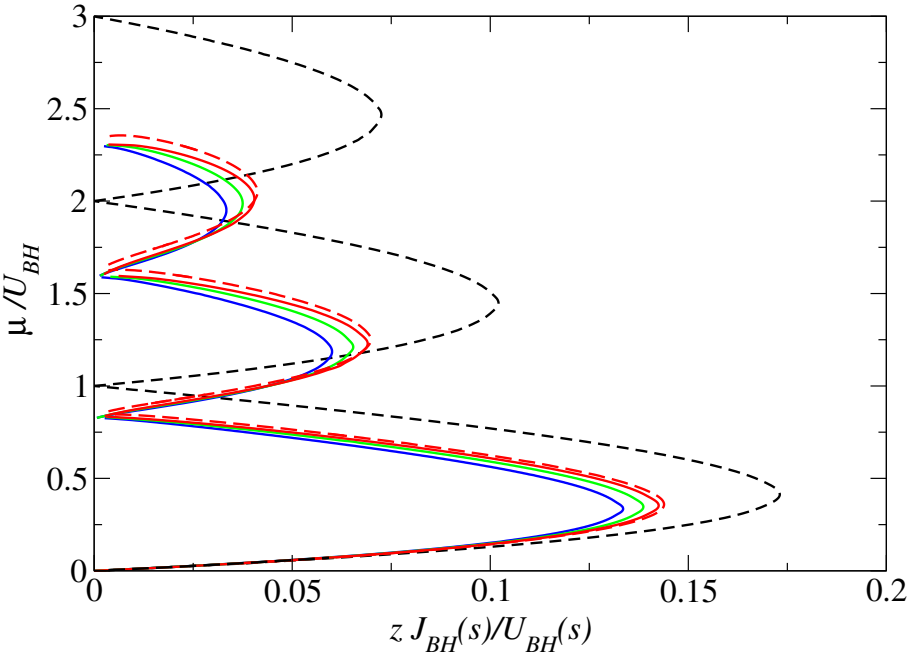

Figure 4.4: Mean field phase diagrams for 1D, 2D, and 3D lattices. Different curves denote borders between MI and SF phases. Dashed black lines correspond to the standard BH model for any dimension, blue, green, and red curves denote 1D, 2D and 3D lattices of the EMO Hamiltonian. Dashed red lines show the result obtained for 9 bands as in [38]. The limit $zJ_{BH}(s)/U_{BH}(s)), s \to \infty$ is different for each dimension. The $s \to \infty$ limit corresponds to the ill-defined situation in which the transverse lattice is shallower than the main lattice (this formal limit is also dimension-dependent). The perpendicular lattice depth is fixed at $s_\perp = 34.8$, $\lambda = 754$ nm, $2a_s/\lambda = 0.014$ as appropriate for ^{87}Rb [38]. Image from [92].

Decimation (TEBD) [69, 73] algorithm and imaginary time evolution. It yields the same minimum as the DMRG algorithm. We have chosen the lattice size to be $L = 100$. It allows to avoid finite size effects, except for regions close to the MI tip. There the extrapolation was performed using $L = 200, 300, 400$ results. A better, but more computationally demanding alternative would be to use translationally invariant TEBD algorithm which works directly in the thermodynamical limit [91, 132]. The transverse lattice depth is again $s_\perp = 34.8E_R$. Let $\epsilon^N(s)$ be the ground state energy of a N-particle system for lattice potential depth s. We approximate values of chemical potentials μ_+, μ_- delimiting the Mott insulator region from above and below (see Section 1.4.4). The specific formulas for the MI with average site occupation n are: $\mu_+(s) \approx \epsilon^{nL+1}(s) - \epsilon^{nL}(s)$, $\mu_-(s) \approx \epsilon^{nL}(s) - \epsilon^{nL-1}(s)$. Having found the phase diagrams for both BH and the EMO Hamiltonians, we plot them in Figure 4.5. The difference between the two phase diagrams

is similar to the mean field case: the EMO phase diagram shows MI-SF phase transition moved to shallower lattices. This has a nontrivial effects on dynamics as shown in next section.

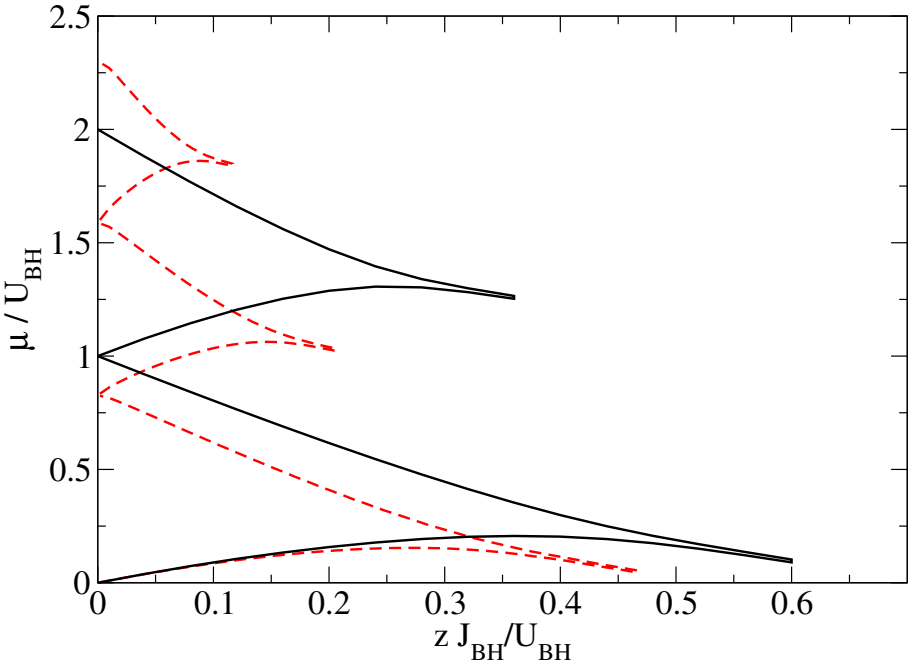

Figure 4.5: The 1D phase diagram obtained using imaginary time evolution and the TEBD algorithm. Black solid curves presents the standard BH 1D case, the red dashed lines are obtained for the EMO 1D model (4.6) with $s_\perp = 34.8$. Image from [92].

4.3 Modulation spectroscopy analysis of the Multi-band effective Hamiltonian

As described in detail in Section 3.2.2, the modulation spectroscopy may be used to probe the excitation spectrum of a ultracold quantum gas. It may be used to detect the energy gap for excitations and determine insulator or superfluid behavior of the gas modelled by the BH model. We have studied what is the effect of renormalization of parameters J and U on absorption spectra of the system of ultracold atoms in the optical lattice with the presence of an external trap. Until now results from the ordinary BH model were available [128, 133]. Also the experiment [10] (already referred to in Section 3.2.1) was finalized with absorption spectroscopy to prove the existence of the gap in the system of lack thereof. The goal was to verify the insulator character of the supposed BG phase. The experimental data have shown an inconsistency with a theoretical model given by the BH

Hamiltonian. Work [10] gave a different (1.9 kHz) prediction for the position of the absorption peak which was expected to be located at a frequency ω related to the interaction energy U_{BH} by $\hbar\omega = U_{BH}$. The latter gives a prediction of 2.3 kHz. This led authors of [122] to model an optical lattice potential of height s by a theoretical optical lattice potential of height $(7/8)s$ which shifted the absorption peak to the experimental [10] position and provided a good agreement of experiment and theory. In case of the dilute rubidium-87 gas used in [10] it is true that

$$U_{BH}(7/8s) \approx \frac{1.9}{2.3} U_{BH}(s). \tag{4.8}$$

However only hand waving arguments that including higher bands in the analysis leads to decrease of the interaction energy of atoms (greater spread of the single particle mode) could be made. In this section we augment the equation (4.8) with:

$$U_{BH}(7/8s) \approx U_2(s), \tag{4.9}$$

which has the true physical meaning. The dependence of U_n on n is weak, and for low per-site densities $U_n \approx const. \neq U_{BH}$. Therefore the MO Hamiltonian may be approximated by the effective BH model with different parameters of U and J.

The coefficients of the effective multiorbital Hamiltonian (4.6) U_n have been calculated in a identical way as described in the previous paragraphs. The approximate equation (4.9) is indeed satisfied. Detailed analysis shows that absorption peaks shape depends on the Mott plateau in which the excitation takes place (contrary to the pure BH model). Excitations within $n = 1, 2, 3$ Mott plateaus should be placed (in $J \to 0$ limit) at $U_2 = 2$ kHz, $-2U_2 + 3U_3 = 1.85$ kHz, $U_2 - 6U_3 + 6U_4 = 1.74$ kHz. This may be inferred from the difference of energy (still assuming $J \to 0$ limit) of a Fock state obtained by moving a particle from site i to the site j (in our case $|i-j| = 1$) which is shown in Appendix 9.3. The deep final optical lattice of height $s = 16E_R$ prohibits almost completely any tunnellings. The "average" peak position is 1.87 kHz in a good agreement with the experiment.

We now move to study a smaller system, similar to the one studied in [119, 133]. We fill the trap with $N = 36$ particles. Again this is an ultracold gas of atoms in an external harmonic trap, with curvature $\kappa = 0.009$. The lattice depth is $s = 15E_R, s_\perp = 30E_R$. The scattering length is $a_s = 5.45$nm. We computed the renormalized J_{n_1,n_2}, U_n parameters. In particular we obtain $U_{BH} = 0.662E_R$ and $U_2 \approx 0.565E_R, W \approx 0.0125E_R$. We use the full EMO hamiltonian for numerical simulation.

Computation of a ground state and numerical simulation was performed by means of the TEBD algorithm. Occupation of each site was truncated by allowing up to 6 particles in each site (with mean not exceeding 2).

The average site occupation of ground states of EMO and BH Hamiltonians form a wedding-cake particle distribution (like in Figure 3.2) with

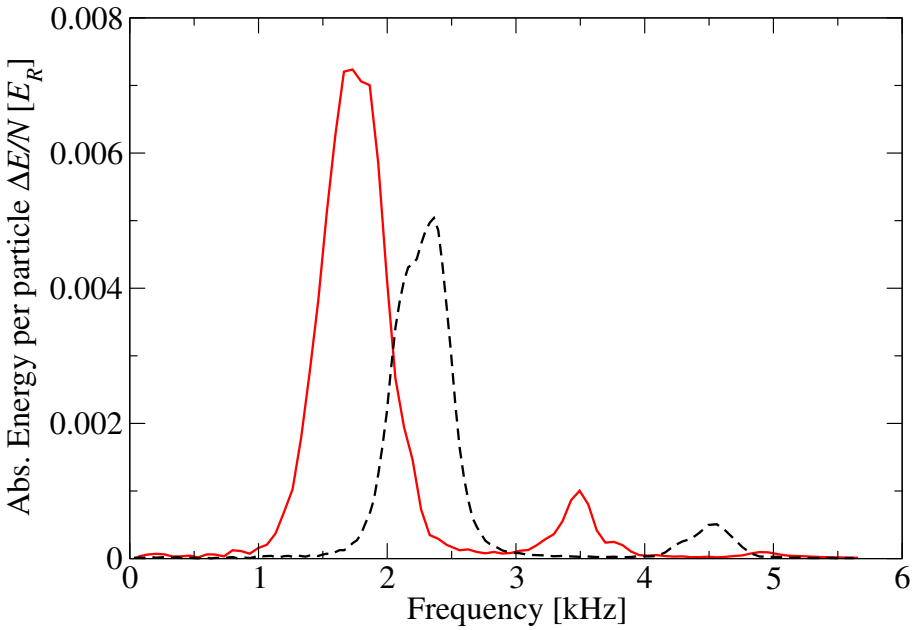

Figure 4.6: Absorption spectrum obtained by applying the lattice modulation with amplitude $s_m = 1E_R$ on the wavepacket created by exponential ramp up to $s = 16$. The black dashed line corresponds to the standard BH model, the red line is the result of effective multiorbital theory. The position of the absorption peaks in the latter case reproduce well the experimental results [10]. Image from [92].

innermost MI region occupied by 2 particles per site. Both distributions are very alike. This enables us to interpret any difference of the excitation energies as an effect of interaction energy renormalization. The contribution of local, single particle energy cancels out.

We have performed the absorption spectroscopy (Section 3.2.2) simulation with total modulation phase duration $t = 100\hbar/E_R$. The modulation amplitude of the lattice potential height was $s_m = 1E_R$. The results are shown in Figure 4.7.

The obvious difference between the energy spectra obtained for the BH and EMO Hamiltonians is that the spectrum for the EMO Hamiltonian is significantly shifted towards lower energies. The center of its main structure is located at position U_2 in contrast to U_{BH} for the BH Hamiltonian.

An another feature is that the absorption spectrum under the EMO Hamiltonian is broader and additional, secondary peaks may present in the main structure. A peak corresponding to excitations within $n = 1$ Mott plateau stands out from the top-right part of the main peak. In atomic, $J = 0$ approximation the elementary excitation energy within $n = 1$ MI is by roughly $0 < -3W = (-2U_2 + 3U_3) - U_2$ higher. See elementary derivation

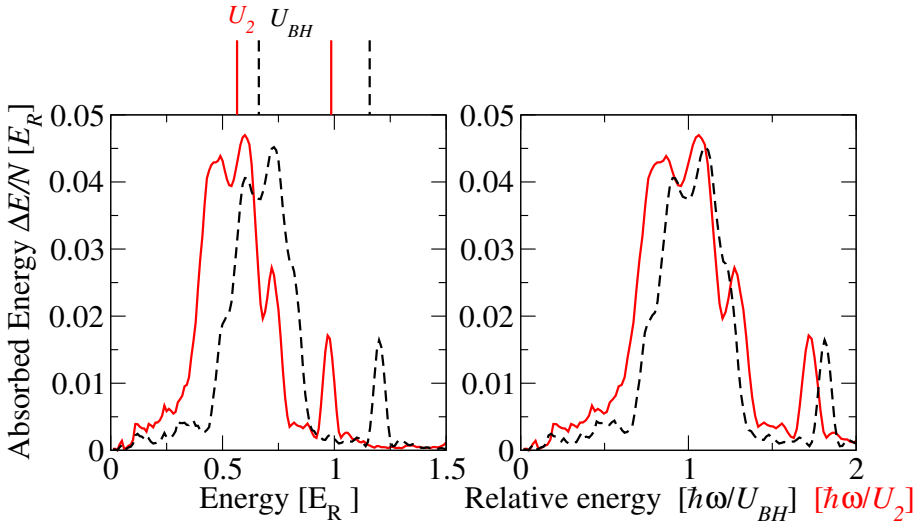

Figure 4.7: Absorption spectrum (modulation time $t = 100\hbar/E_R$, modulation amplitude $s_m = 1$). Black dashed lines correspond to the BH model, red solid curves to the effective multiorbital theory. Left panel shows spectra on a common energy scale, observe the significant shift of the EMO structure toward smaller energies. Bars above the plot give the mean expected positions of peaks for the n=2 Mott plateau. Right panel shows the same data with rescaled energy axes (U_{BH} for the black curve, U_2 for the red one). Image from [92].

of this result in the Appendix 9.3.

The absorption spectra are quite sensitive to the system's density distribution. Adding or removing a couple of particles, may make EBH and BH prediction for the ground state substantially differ. Indeed, deplacement of particles between MI edges cost very little energy and are sensitive towards Hamiltonian parameters alteration (mainly to U change).

4.4 Numerical diagonalization of n particle problem and U, J parameters determination

Solving the single site, interacting n-particle, multiband problem as needed for U_n and J_{n_1,n_2} particles computation reduces to the evaluation of ground state of the Hamiltonian (4.1). As described in the Section 4 the full Hamiltonian matrix is prohibitively large for full diagonalizations even if relatively small number of Bloch bands B is included. The basis consists of n-particle Fock states with particles occupying B^3 modes. Let us choose a subset V of those basis states. Let us consider a submatrix of $\mathcal{H}_{int}$ (see Eq. 4.1)) called $\mathcal{H}_{int}(V)$ defined by those entries with indices corresponding to the set V. The smallest eigenvalue of $\mathcal{H}_{int}$ is bounded form above by performing

the diagonailzation of the matrix $\mathcal{H}_{int}(V)$ and taking the least eigenvalue $\epsilon^n(V)$ as an estimate. Naturally $\epsilon^n(W_1) \geq \epsilon^n(W_2)$ for any $W_1 < W_2$. Thus a good quantifier of the quality of the diagonalization subspace is the lowest eigenvalues itself.

The optimal choice of V is to include only those Fock basis states which inclusion is expected to influence the bound for the least eigenvalue most significantly. This prompted authors of the effective Hamiltonian method [38] to restrict themselves to the Fock states $|\psi\rangle$ with smallest $\langle\psi|\mathcal{H}_{int}|\psi\rangle$.

In the single band, the ground state is just the Fock state with n particles occupying the lowest Bloch band $(0,0,0)$. If more bands are included, classical perturbation theory is an argument for taking the quotient $Q(\psi) = \frac{|\langle\psi|\mathcal{H}_{int}|\psi_0\rangle|}{E(\psi)-E(\psi_0)}$ as a measure of the importance of the basis state ψ. Maximizing the Q quotient allows for choosing of basis states that are both of low energy, and strongly coupled to the ground state Fock state. By the perturbation theory these two features ensure that most of relevant states will be chosen. Using the Metropolis algorithm we have sampled the set of all basis states to choose a set of states V with largest value of the quotient. The details are described in the appendix. We have performed diagonalization in the "least-energy" basis and the "high-Q" basis. Actually the formula for Q corresponds to a first order perturbative expansion. It may be generated to second and higher orders (see Appendix 9.4). In the final solution only about 1% of the elements of V were taken in the second order. The interaction Hamiltonian $\mathcal{H}_{int}$ matrix coupling the ground state with a Fock state with a single particle promoted to a second excited state is proportional to $n^{3/2}U^{2000}$ and this causes the energy change of $\Delta = E^2 - E^0$. The requirement for validity of the perturbative approach is $\Delta \gg n^{3/2}U^{2000}$. For typical parameters corresponding to Rb atoms this yields a final estimate of $n \ll 15$ (we have verified that indeed for larger n the least energy method is more efficient). Curiously in high density regime the zero order ground state is no longer $(a^\dagger_{(0,0,0)})^n|\Omega\rangle$, and the BH Hamiltonian is clearly invalid. This is because the local energy grows with n as $\frac{U^{0000}}{2}n(n-1) + E^0 n$ (*). For large enough n it may be beneficiary for example to move some particles from a mode $(0,0,0)$ to a mode $(2,0,0)$ and others. This then gives the energy $\frac{U^{0000}}{2}n_0(n_0-1) + \frac{U^{2222}}{2}n_2(n_2-1) + 2U^{0022}n_0n_2 + E^0n_0 + E^2n_2$ which may be smaller than energy (*) for $n_2 + n_0 = n$. Indeed, for the $\sin^2(k_x x)$ periodic potential, we have $U^{2200}, U^{2222} < U^{0000}$, and single particle, linear in n_i energy terms $E^0n_0, E^2n_2, E^0 < E^2$ no longer dominate the energy value and fix $n_2 = 0$.

Figure 4.8 shows comparison of U_n parameters (being, up to a constant, the ground state energy) for both basis choice methods. Clearly for a given basis size using "least-energy" basis may give a false impression of convergence of the results if at least $B = 9$ bands are used. Analysis of least-energy basis vector set with 40 thousands elements shows that the reason for that

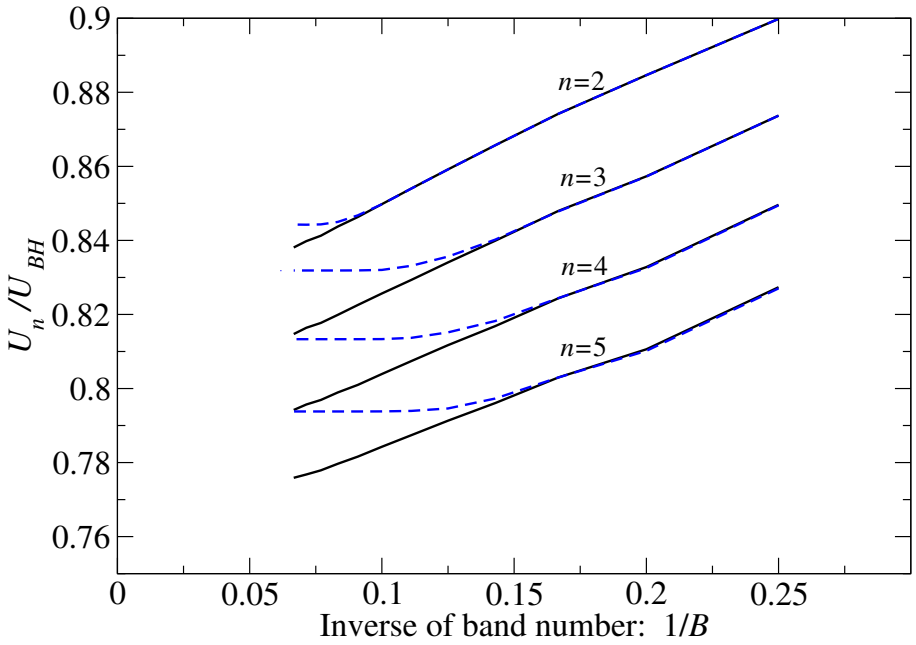

Figure 4.8: Comparison of the effective on-site interaction strength U_n obtained using diagonalization of the on-site Hamiltonian $\mathcal{H}_{loc}$ on two different basis sets with the same size equal to 40000. If basis vectors are chosen according to their energy (dashed lines), false saturation effects appear. Estimating the influence by a perturbative-like scheme (solid lines) does not seem to suffer from saturation effects. The 3D case is considered: $s = s_\perp = 34.8E_R$. Image from [92].

is trivial: hardly any Fock vector with any particle in higher band than 9th, makes it into the set V, no matter how big B is. It turns out that some of elements of V, although with low energy, have little impact on diagonalization as they are weakly coupled to the zero-order, single band result. Optimizing for Q parameter enables to include more important basis vectors resulting in increased performance seen in Figure 4.8. Moreover the least energy estimate may be expressed as

$$E(B) = E_\infty + \frac{c}{B}, \tag{4.10}$$

with no signs of early saturation around $B = 9$.

The point interaction is only an approximation. For large enough band number, and therefore momentum, the microscopic description of atom-atom collision has to be carried out. The trend suggested by Eq. (4.10) and confirmed by data presented in Figure 4.8 was derived under low energy assumption and for large B is be expected to be modified due to terms in the interaction potentials that have not been included [34, 35].

Chapter 5

Fast dynamics of the optical lattices [134]

The Multiband Bose-Hubbard model (1.6) is equivalent to the second-quantized Hamiltonian for a fixed lattice potential height s, if all Bloch bands and arbitrary long large interaction and hopping terms are included. As discussed in Section 1.2 under reasonable assumptions it may be expected to provide an almost exact description of physics. Actually, a question of convergence makes these suppositions hardly obvious (see Chapter 4). It turns out that when considering dynamics of the Multiband Bose-Hubbard model, the continuous to discrete model mapping should be put under additional scrutiny if the optical potential strength s is time-dependent. Strong additional dynamical couplings may appear, including of which in the description is necessary for accurate description of dynamics.

The derivation of the MBH model presented in the Section 1.2 of this thesis was based upon the expansion of the field operator in the localised modes defined by the Wannier functions.

At the level of a single particle physics: derivation of the MBH describing a single particle uses a mapping $\mathcal{U}$ from the Hilbert space of complex functions defined on the real 3D space to the discrete Fock space spanned by Wannier functions modes, being in case of the separable potential a product of 1D Wannier functions $w_i^\alpha(x)w_j^\beta(y)w_k^\gamma(z)$ calculated for lattice depth s. Such a mapping takes, naturally, explicitly into account the shape of the Wannier functions and is therefore s-dependent: $\mathcal{U}(s)$. To describe 1D systems we restrict to $i = j = k$ and $\gamma = \beta = 0$ (for 2D the condition $\beta = 0$ would be dropped).

If the optical lattice depth s is itself time-dependent, for example s is varied in experiment to alter the U/J ratio, then by a textbook change of basis we get the following time-dependent Hamiltonian:

$$\mathcal{H}_\mathcal{W} = \mathcal{H}_{MBH} + \mathcal{W} = \mathcal{H}_{MBH} + i\hbar\frac{d}{dt}(\mathcal{U}(t))\mathcal{U}^\dagger(t), \quad \mathcal{W} = \mathcal{T}ds/dt, \quad (5.1)$$

which governs the time-evolution by the Time-Dependent Schrödinger Equation (TDSE) in the time-dependent basis defined by the instantaneous Wannier functions. Naturally in the position representation the Hamiltonian is $\mathcal{H}_X$ with no modification. The term $\mathcal{T}$ in (5.1) may be expanded as (see Appendix 9.2 for details):

$$\begin{aligned} \mathcal{T} &= \mathcal{T}_x + \mathcal{T}_y + \mathcal{T}_z, \\ \mathcal{T}_x &= -i \sum_{i,j,\alpha,\beta} T^{\alpha\beta}_{i-j}(s_x)(a^\alpha_i)^\dagger a^\beta_j, \\ T^{\alpha\beta}_{i-j}(s_x) &= \int w^\alpha_i(x, s_x) \frac{d}{ds_x} w^\beta_j(x, s_x) \mathrm{d}x. \end{aligned} \tag{5.2}$$

Had the considered optical lattice potential not been separable, the above formulas for $\mathcal{T}$ operator would not separate into sum of x, y and z direction. The integral defining $T^{\alpha\beta}_{i-j}$ would have to contain an integral of a 3D Wannier function over whole $\mathbb{R}^3$ space. As from now on we restrict ourselves to the 1D lattice, we have $\mathcal{T}_y = 0$ and $\mathcal{T}_z = 0$ which corresponds to s_y, s_z =const. Transition integrals $T^{\alpha\beta}_{i-j}(s)$ obey relations: $\forall i, j, \alpha : T^{\alpha\alpha}_{i-j} \equiv 0$, $T^{\alpha\beta}_{i-j} = (-1)^{\alpha+\beta} T^{\alpha\beta}_{j-i} = -T^{\beta\alpha}_{j-i}$, $T^{\alpha\beta}_0 = 0$ for $\alpha - \beta$ odd. The additional coupling tunnelling like terms from Eq. (5.2) which were brought about by the optical potential height dependence on time do couple different bands as opposed to the kinetic energy operator in (1.6). Moreover extra single-particle on-site couplings mixing Bloch bands appear. Figure 5.1 shows values of parameters T.

Eq. (5.1) does not depend on a particular way the lattice is distorted. The same equation describes the situation when the lattice is made oscillating sideways that is the lattice potential is $V(x, t) = V(x - x_m \sin \omega t)$. The different modulation method results in altering the formula for the coupling constants T, which in the latter case are:

$$T^{\alpha\beta}_{i-j}(s) = -\int w^\alpha_i(x, s) \frac{d}{dx} w^\beta_j(x, s) \mathrm{d}x. \tag{5.3}$$

Transition integrals in this $T^{\alpha\beta}_{i-j}(s)$ obey relation $T^{\alpha\beta}_0 = 0$ for $\alpha - \beta$ even.

Experimental noise makes the laser intensity fluctuate randomly, with high frequencies. This context in which terms similar to (5.2) arise was studied in [135].

To study the effect of the additional couplings two scenarios for change of optical lattice depth were investigated: fast linear (in s value) quench and modulation spectroscopy experiment, where parameters U and J of the optical lattice are modulated due to harmonic oscillation of the optical lattice depth s.

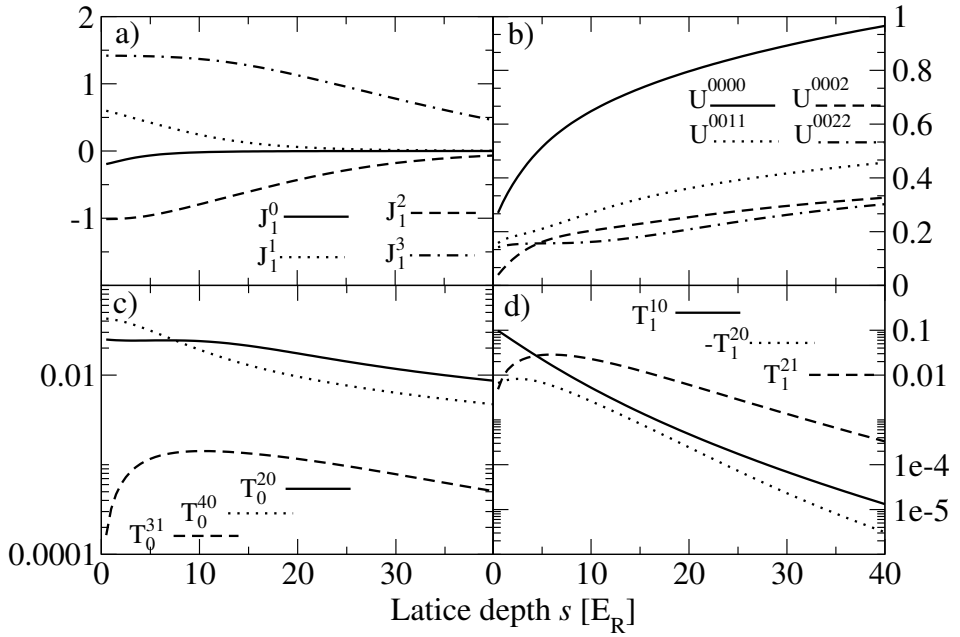

Figure 5.1: Relevance of different transition amplitudes: (a) – nearest neighbor tunnellings J_1^α for different Bloch bands (b) – interaction integrals for $g = 1, \kappa = 2\pi$; the term U_{iiii}^{0000} term present in the Bose-Hubbard Hamiltonian is compared with interaction terms involving excited bands.Panels (c) and (d) show additional amplitudes $T_{i-j}^{\alpha\beta}$ [see Eq. (5.2)] coming from the time-dependence of Wannier functions [i.e. $\mathcal{W}$ term (5.1)]. Image from [134].

5.1 A linear quench

In this section we will consider a linear quench of a small system, containing $N = 5$ ^{87}Rb atoms in a 1D lattice of containing $L = 4$ under periodic boundary conditions (PBC). The initial depth of the lattice is $s_0 = 12E_R$. The linear quench is realized by changing the optical lattice depth linearly with time $s(t) = s_1 t/\tau + (1 - t/\tau)s_0$. Here τ is the total duration of the quench. The ground state obtained by the exact diagonalization of (1.6) serves as an initial state. The final depth of the lattice is $s_1 = 40E_R$. The quench is performed for different values of τ. In the following we did not choose to incorporate the effect of the finiteness of $L = 4$ on coefficients T. That is, we have used the same J, U and T values that one obtains if one uses Wannier functions computed for the infinite lattice. We did not aim for high precision description of a purely academic four well potential under PBC in real space, but rather to obtain some idea what are the effects one may expect in realistic systems. Naturally our analysis still suffers from some finite-size effects (as $a_0 \equiv a_L$) but we believe that our approach has

eliminated one of two sources of them and makes our results more applicable to large systems.

We find that (see Figure 5.2) as soon as $\tau < O(\hbar/E_R)$ the final energy becomes significantly larger in the presence of the $\mathcal{W}$ term than without it. That reflects an increased occupation of the second excited band. Thus a simple treatment of higher bands via the MBH model is insufficient to explain the dynamics; time-variation of Wannier functions has to be taken into account.

An important special case of the linear quench may be singled out. It is the instantaneous quench limit $\tau \to 0+$. A Hamiltonian governing the evolution is second-quantization many particle Hamiltonian in the real space (1.5). The zero time evolution is described by the evolution operator $U_X(\tau, 0) = P \exp\left(\int_0^\tau H_X(t)\mathrm{d}t\right)$ taken to $\tau \to 0+$ limit, ie $U_X(0+, 0) = Id$. The description in terms of the Multiband Bose-Hubbard Hamiltonian (1.6) without the $\mathcal{T}$ terms (5.2) leads to the same conclusion. Let $\mathcal{B}(s)$ denote the one particle basis of Wannier functions for lattice depth s. The basis which is used in the MBH model for the initial time is $\mathcal{B}(s_0)$ and after the time $\tau \to 0+$ it is $\mathcal{B}(s_1)$. The expansions of the state vector in position representation in the different bases $\mathcal{B}(s_0)$ and $\mathcal{B}(s_1)$ have to yield a different expansion coefficients what contradicts the MBH model predictions that $U_{MBH}(0+, 0) = Id$. The conclusion is that for $\tau \to 0+$ the evolution operator is well approximated by $\mathcal{P}e^{\int_{s_0}^{s_1} \mathcal{W}(s)\mathrm{d}s}$ as $H + \mathcal{W} = H + \frac{ds}{dt}\mathcal{T} \to \frac{ds}{dt}\mathcal{T}$ for $\tau \to 0+$. This is just a change of basis operator: $U(s_1)U^\dagger(s_0)$. In Figure 5.2 one may observe the described behaviour for small enough τ.

5.2 Modulation

Recently it has been suggested [131] that periodic modulations of the lattice depth, for example in the x-direction,

$$s_x(t) = s_x^0 + s_m \sin(\omega_x t), \tag{5.4}$$

can be used to excite the atoms in the optical lattice to a state in the excited Bloch band. The Bloch bands are separated by a large gap, and high frequency modulation is required to couple them [131]. This this means that the lattice depth oscillates quickly, and ds/dt is large. Therefore the effect of the $\mathcal{W}$ term may be expected to be large. These terms were not considered in [131].

To quantify the importance of the $\mathcal{W}$ part is, we have recalculated the numerical simulation [131] using the MBH Hamiltonian (1.6) with and without the additional $\mathcal{W}$ term, Eq. (5.1-5.2). The studied system is a 2D lattice in a deep lattice regime. The gas is in a Mott Insulator phase. The lattice

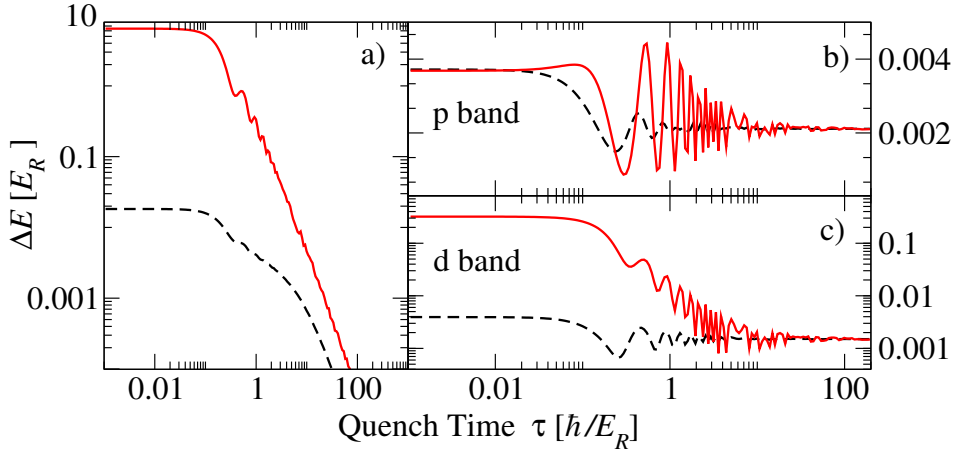

Figure 5.2: The energy gain ΔE (i.e. the excess energy over the corresponding ground state) after a linear quench of a model 1D system from $s_0 = 12E_R$ to $s_1 = 40E_R$. For the adiabatic process $\Delta E = 0$. Red (black, dashed) lines correspond to the simulation with (without) the $\mathcal{W}$ term (5.1) in the time-dependent Hamiltonian. Panels b) and c) show time variation of averages of band occupation operators $\langle \hat{n}_1 \rangle$, $\langle \hat{n}_2 \rangle$. Image from [134].

depths in x, y directions, and transverse harmonic confinement with curvature κ are $(s_x = 32, s_y = 20, \kappa = 8)$. The large depth of the potential wells allows to neglect hopping in the lattice an consider layers of indpendent 2D sublattices (see Figure 1.1) each consisting of decoupled sites. We assume that each site is filled with exactly $\nu = 2$ atoms.

The simulation is performed by preparing the system in the ground state $|\psi(0)\rangle$ with energy E_0 (again we use exact diagonalization). Just as in [131] we restrict the numerical simulation to first three bands in both directions x and y. We are aware that the $\mathcal{W}$ term efficiently populates higher bands, but this restriction has the advantage that we consider the model as in [131].

We have performed the numerical simulation of modulation of the optical lattice depth s_x lasting 10 ms. We have analyzed a whole spectrum, by performing several runs with different modulation frequencies ω_x. In [131] the author introduced a maximal ground state depletion function: $\delta(\omega_x) = 1 - \sup_{t\in[0,T]} |\langle \psi_{\omega_x}(t) | \psi(0) \rangle|$. Here $\psi_{\omega_x}(t)$ is a solution of the Time Dependent Schrödinger Equation and ω_x is the modulation frequency.

The results (presented in Figure 5.3) show that inclusion of the $\mathcal{W}$ term leads to a significant alteration of description of the dynamics. The simulations performed with the $\mathcal{W}$ term present, contain several additional excitations. Moreover excitations already existing in the simulation by the pure MBH Hamiltonian are modified by broadening and shifting the excitation peaks obtained.

The key point made in [131] is a possibility of efficient population of

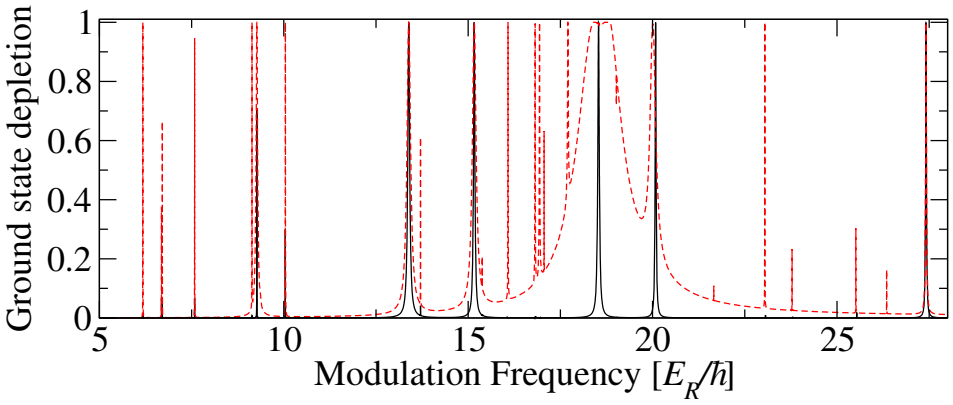

Figure 5.3: Excitation via modulation of the lattice depth with and without $\mathcal{W}$ term, Eq. (5.1). The depletion function during the first 10ms, without (black, solid) and with the $\mathcal{W}$ term (red, dashed). The broadening of the peak around $\omega = 18.5 E_R/\hbar$ is a power broadening effect, see discussion in the text. Image from [134].

higher Bloch bands optical lattice modulation. We have determined that including the $\mathcal{W}$ term in the analysis does not hamper the feasibility of the process. On the contrary, we found that the efficiency of such state preparation procedure is greater than simulations performed using the MBH Hamiltonian without the W terms would suggest. The occupation of atomic states in higher Bloch bands is performed by Rabi-like oscillations (see Figure 5.5). The oscillation period is decreased usually several times with similar excitation efficiency (the Rabi-like oscillations' amplitude). Therefore, while confirming the possibility of direct resonant transfer of population to excited bands by lattice depth modulation, our analysis suggests that taking the time variation of Wannier functions into account is crucial for controlling the process and for selective excitation of desired bands.

The effects of presence of the $\mathcal{W}$ term in the Hamiltonian, on the dynamics (5.1), may be also visualized using the using the Floquet theory [136]. The Floquet theory entails analysis of a stroboscopic evolution operator, which evolves the system for a time corresponding to a whole oscillation period. Its eigenstates are states that, although not stationary during the evolution, are stationary up to a phase factor after evolution by a full oscillation period. The widths of avoided crossings present in the spectra are related to the Rabi oscillation periods.

As a on object for the analysis, we have chosen a broad resonance peak with energy 18.5 E_R present in Figure 5.3. Spectra of the evolution operator $\mathcal{P}\exp(i\int_0^{2\pi/\omega} H(t)\mathrm{d}t)$ are shown in Figure 5.4. The spectrum without $\mathcal{W}$ contribution shows a single isolated avoided crossing indicating a simple resonance (corresponding to the isolated peak in Figure 5.3). This contrasts

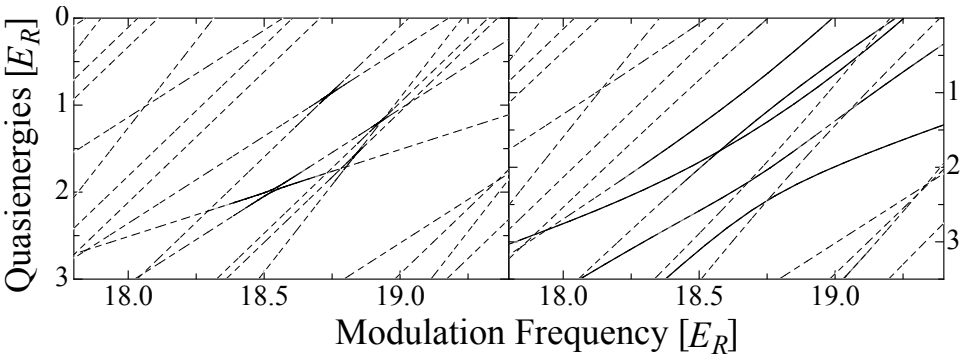

Figure 5.4: Floquet spectrum without $\mathcal{W}$ contribution (left) and with with $\mathcal{W}$ term, Eq. (5.1) (right panel). Broad avoided crossings for the latter are due to the strength of terms omitted within BH description as well as the influence of higher harmonics - see text for discussion. The region of avoided crossings (large curvatures) is highlighted with solid lines. The black color intensity increases with the curvature. Image from [134].

with the case of the quasi-exact evolution, where a compound resonance is present. This structure correlates well with the broadened peaks observed in the depletion function.

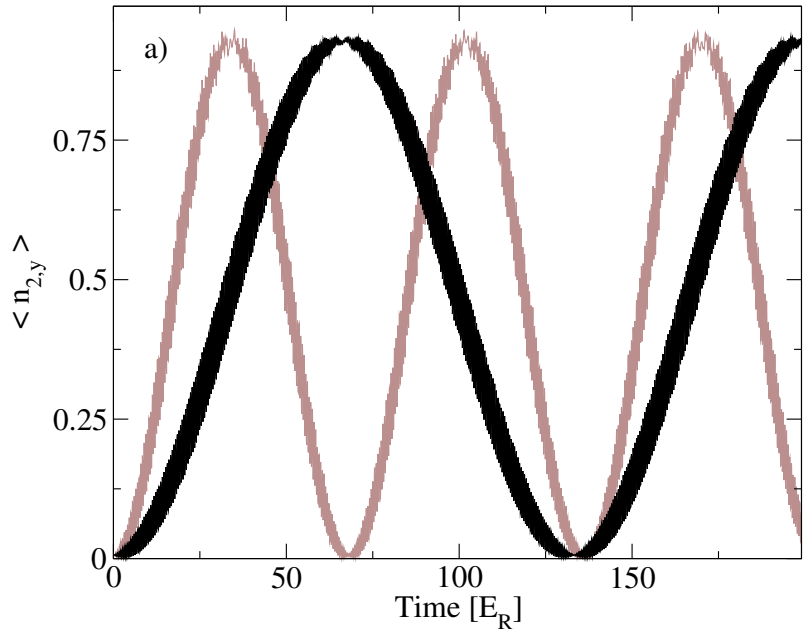

Figure 5.5: Average value of operator $n_{2,y} = a^{\dagger}_{(0,2)} a_{(0,2)}$ as a function of time during the modulation. Brown curve shows the results in the presence of the $\mathcal{W}$ terms (5.2), black for ordinary MBH model (1.9). The ordinary MBH model underestimates the target state population speed by a factor of 2. Image from [134].

Chapter 6

Spinor Bose-Hubbard model with disorder [137, 138]

Spinor Bose-Hubbard (BH) models describe strongly correlated lattice systems where bosons have an internal angular momentum (the hyperfine structure) whose orientation in space is not externally constrained. Bosonic interactions are sensitive to the spin degree of freedom leading to a rich phase diagram in zero temperature. Like in the spinless case, interactions may be parametrised by two-body short range (s-wave) scattering length, and the interaction is point-like and rotationally invariant. As interactions are rotationally invariant, scattering depends on total spin only.

6.1 Bose-Hubbard model for spin-1 bosons

Low energy spin-1 bosons loaded in optical lattices, in the complete analogy to the spinless BH model, may be described by the spinor BH model. The appropriate second quantization field operator Ψ, instead of one, has three components: $\Psi_{-1}, \Psi_0, \Psi_1$. The scattering interaction is again by contact interaction which may be decomposed as $V(x-x') = g_0 P_0 \delta(x-x') + g_2 P_2 \delta(x-x')$ where P_i are projection operators in the two particle space to a state with total spin 0 or 2. Odd total spins are forbidden by bosonic exchange symmetry of atoms. The remaining limitations are analogous to those discussed in Section 1.2. The corresponding Hamiltonian is [139]:

$$\begin{aligned} \hat{H} &= -J \sum_{\langle i,j\rangle,\sigma} \left(\hat{a}^\dagger_{i\sigma} \hat{a}_{j\sigma} + \hat{a}^\dagger_{j\sigma} \hat{a}_{i\sigma} \right) + \frac{U_0}{2} \sum_i \hat{n}_i (\hat{n}_i - 1) \\ &+ \frac{U_2}{2} \sum_i \left(\hat{S}_i^2 - 2\hat{n}_i \right) - \mu \sum_i \hat{n}_i, \end{aligned} \tag{6.1}$$

where $\langle i,j\rangle$ denotes summing only over i,j being nearest neighbors in the lattice and $\hat{a}^\dagger_{i\sigma}$ ($\hat{a}_{i\sigma}$) denotes the creation (annihilation) operator of a boson

in the lowest Bloch band localised on site i with spin component $\sigma = 0, \pm 1$.

The first term in (6.1) describes spin preserving hopping with a tunnelling amplitude J (in complete analogy to the ordinary BH model). The second and third term are spin independent and spin dependent pointlike interactions. The interaction coupling constants are $U_{0,2} = c^i_{0,2} \int d\vec{r} W^4(\vec{r} - \vec{r}_i)$ with $c^i_0 = 4\pi\hbar^2(a^i_0 + 2a^i_2)/3m$ and $c^i_2 = 4\pi\hbar^2(a^i_2 - a^i_0)/(3m)$, where a^i_S is the s-wave scattering length of two particles with total spin S [14, 140] and $W(\vec{r} - \vec{r}_i)$ is the Wannier function of the lowest band at site i. We have allowed some latitude for explicit dependence of a_S on site i. Spatial variation of the scattering length is the way to introduce disorder in interaction parameter value and it will be described in detail later. The third term of (6.1) depends on spin configuration of atoms within a single lattice site i. The spin operator used here is defined as: $\hat{S}_i = \sum_{\sigma\sigma'=0,\pm1} \hat{a}^\dagger_\sigma (F_i)_{\sigma\sigma'} \hat{a}_{\sigma'}$. Matrices F are spin matrices for angular momentum $S = 1$ in the spin basis. The operators $\hat{S}_i$ satisfy angular momentum commutation relations $[\hat{S}_l, \hat{S}_j] = i\epsilon_{ljk}\hat{S}_k$, and they commute if taken at different sites.

Note that the spin-dependent interaction energy described solely by the third term in (6.1) is minimized if the total spin is zero for $U_2 > 0$ (antiferromagnetic regime). For $U_2 < 0$ the minimal energy is reached when spin takes maximal allowed value [14, 140, 141]. In the grand canonical approach the total number of particles is controlled by the last term of (6.1) where μ is the chemical potential and $\hat{n}_i = \sum_{\sigma=0,\pm1} \hat{n}_{i,\sigma}$, is the total number of bosons operator on site i. More details about the derivation can be found in [14, 36, 140, 142, 143].

In the Hamiltonian (6.1) all the parameters are site-independent, provided a^i_S is homogeneous. As discussed in Section 1.2.1, the model also may be made site-dependent by introducing an external potential (which is described by using site-dependent chemical potential μ_i). The last term of (6.1) takes then the form $\sum_i \mu_i \hat{n}_i$. In this work we depart from the confines of the details of disorder realization and we will assume that the chemical potentials μ_i are random numbers with uniform distribution on the interval $[\bar{\mu} - \Delta\mu, \bar{\mu} + \Delta\mu]$. We will also consider situations where other parameters are random. Although there are plenty of possible choices, we will only consider situations where U_2 is a random parameter. This may be realized by introducing space-inhomogeneous magnetic field to alter scattering lengths a_0 and a_2.

6.1.1 The phase diagram at $J = 0$

The starting point of the analysis of spinor Bose-Hubbard model is gaining full understanding of the model in $J = 0$, single site limit. In contrast to ordinary BH model, in that limit interplay of U_2, μ, U_0 parameters leaves a potentially rich phase diagram.

In this limit, lattice sites are decoupled. Each site has its own Hamilto-

nian $H_{0,i}$ and $\hat{H}_0 = \sum_i \hat{H}_{0,i}$ with

$$\hat{H}_{0,i} = -\mu\hat{n}_i + \frac{U_0}{2}\hat{n}_i(\hat{n}_i - 1) + \frac{U_2}{2}\left(\hat{S}_i^2 - 2\hat{n}_i\right). \tag{6.2}$$

The particle number, and total spin operators commute, $\left[\hat{n}_i, \hat{S}_i^2\right] = 0$. The eigenstates of $\hat{H}_{0,i}$ may be chosen so that occupation n_i, spin S_i and $\hat{S}_z$ projection m_i are simultaneously defined $|S_i, m_i; n_i\rangle$. The orbital part of such an eigenstate is just a product of real Wannier functions. Therefore the spin part has also to be symmetric so that the whole wavefunction obeys bosonic statistics. This means that the sum $S_i + n_i$ has to be even.

The eigenenergy of the state $|S_i, m_i; n_i\rangle$ in the atomic limit $J = 0$ is

$$-\mu n_i + \frac{1}{2}U_0 n_i(n_i - 1) + \frac{1}{2}U_2\left[S_i(S_i + 1) - 2n_i\right].$$

We minimize the above to describe the spin structure of the system in $J = 0$ limit. For $U_2 > 0$, the energy is minimized when S_i value is minimized. Bound that $n_i + S_i$ is even means in that case that $S_i = n_i (\mathrm{mod}\ 2)$. For even n_i the state is spin singlet insulator $|0_i, 0_i; n_i\rangle$ [144]. For odd n_i, the $J = 0$ ground state has a nonzero spin, and the state is just $|1_i, m_i; n_i\rangle$. The spin S_z projection m_i is arbitrary as no external magnetic field is assumed. For $U_2 < 0$ the energy is minimized when S_i is maximized. Therefore in the ferromagnetic regime, the ground state is $|S_i, m_i; n_i\rangle, S_i = n_i$, with m_i again arbitrary.

To describe the exact phase diagram it suffices to determine the occupation in both $U_2 < 0, U_2 > 0$ cases (the spin S_i may be uniquely determined from U_2 and n_i). The phase diagram is parametrized by two independent variables $(U_2/U_0, \mu/U_0)$. It is shown in Figure 6.1. As in the pure BH case the $J = 0$ model allows to determine widths of the MI lobes in a typical $J - \mu$ phase diagram. It is interesting to note that in Figure 6.1 for $0 < U_2/U_0 < 0.5$ some boundaries are vertical lines - their position in μ/U_0 variable does not depend on U_2. Because of this fact, as shown later in Section 6.2.2, when disorder is imposed on variable U_2 the position of the boundary is unaltered. It is also responsible for the absence of the BG phase between lobes with occupation $2k$ and $2k + 1$ for $k \in \mathbb{Z}$. In the antiferromagnetic region, as $U_2 > 0$ is increased, odd lobes shrink while even lobes broaden. The phase diagram indicates complete disappearance of odd filled lobes of $U_2/U_0 > 0.5$. In the ferromagnetic case $U_2 < 0$ the lobes shrink as $|U_2|$ increases and disappears for $U_2 = -1$. For $U_2 \leq -1$ the system is unstable: the local Hamiltonian spectrum is not bounded from below in the grand canonical ensemble. Increasing total number of particles decreases the energy without limit. The description would be only possible by fixing the total number of particles. This aspect is not relevant for this thesis.

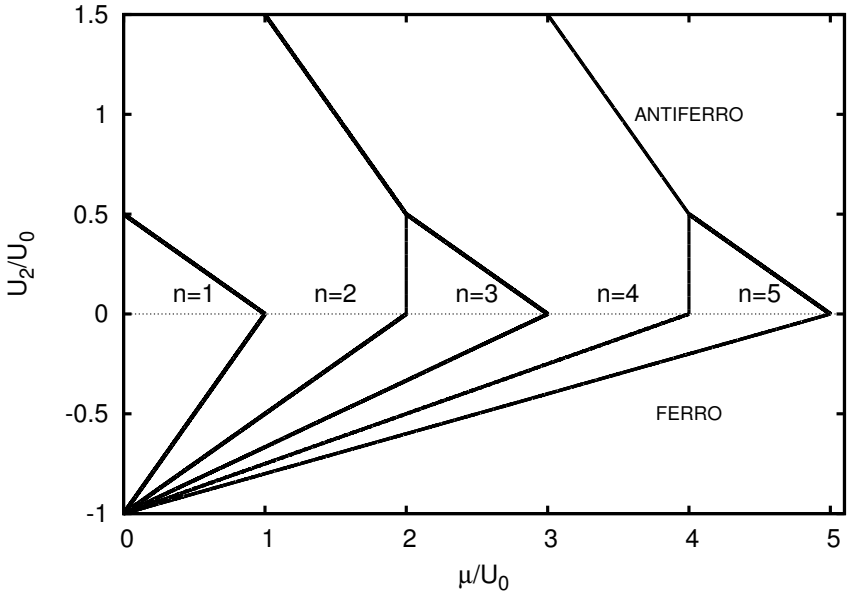

Figure 6.1: Phase diagram of the spinor $F = 1$ BH model in the limit $J = 0$. Each region corresponds to a MI phase with a different integer occupation number. Image from [137].

6.1.2 Probabilistic Mean Field approach

In this Section we will solve the variant of a perturbative mean field theory which yields an analytic formula for the borders of phases for spinor Bose-Hubbard model (6.1). In the $J = 0$ limit the Hamiltonian reduces to the sum of single-site Hamiltonians $\hat{H}_0 = \sum_i \hat{H}_{0,i}$. Introducing standard mean-field decoupling of the tunnelling operator (1.26) we obtain a Hamiltonian: $\hat{H}_{MF} = \sum_i \hat{h}_i$ with

$$\begin{aligned} \hat{h}_i &= -Jz \sum_{i,\sigma} \left[\left(\psi_{i,\sigma} \hat{a}^\dagger_{i,\sigma} + \psi^*_{i,\sigma} \hat{a}_{i,\sigma} \right) - |\psi_{i,\sigma}|^2 \right] - \mu \hat{n}_i \\ &+ \frac{U_0}{2} \hat{n}_i (\hat{n}_i - 1) + \frac{U_2}{2} \left(\hat{S}_i^2 - 2\hat{n}_i \right). \end{aligned} \tag{6.3}$$

To study of zero-temperature properties of (6.1) with the (6.3) mean field Hamiltonian we will find the ground state, which is a minimizer of the energy functional $E_{GS}(\psi_\sigma) = \langle GS| \hat{h} |GS\rangle$ together with the condition $\langle GS| \hat{a}_\sigma |GS\rangle = \psi_\sigma$ which makes the problem nonlinear. This condition does not necessarily have to be imposed, but at minimum it is nevertheless satisfied.

As typical J parameter values of interest are small ($J \ll U_0$) we use perturbation theory around the zero order, $J = 0$ solution with perturbation

Hamiltonian $V = -Jz \sum_\sigma \left[\left(\psi_\sigma \hat{a}_\sigma^\dagger + \psi_\sigma^* \hat{a}_\sigma \right) \right]$.

The eigenstates of the single site Hamiltonian $|S_i, m_i; n_i\rangle$, satisfy:

$$H_{0,i} |S_i, m_i; n_i\rangle = E_0(S_i, n_i, U_0, U_2, \mu) |S_i, m_i; n_i\rangle \tag{6.4}$$

where:

$$\begin{aligned} E_0(S_i, n_i, U_0, U_2, \mu) &= -\mu n_i + \frac{1}{2} U_0 n_i (n_i - 1) \\ &+ \frac{1}{2} U_2 \left[S_i (S_i + 1) - 2 n_i \right]. \end{aligned} \tag{6.5}$$

We have here again that $S_i \in \{0, 1\}$ minimizes the energy E_0 and for $U_2 < 0$ it is $S_i = n_i$ which minimizes the energy. As shown in detail in [143] the ground-state energy up to second order is for odd occupation number given by:

$$\begin{aligned} & E^{(2)}(S = 1, n, J, U_0, U_2, \mu, \psi_\sigma) = \\ = \; & zJ \left[1 - zJ \sum_{j=1,4} \alpha_j(n, U_0, U_2, \mu) \right] \sum_\sigma |\psi_\sigma|^2, \end{aligned} \tag{6.6}$$

and for even occupation

$$\begin{aligned} & E^{(2)}(S = 0, n, J, U_0, U_2, \mu, \psi_\sigma) = \\ = \; & zJ \left[1 - \frac{zJ}{3} \sum_{j=1,2} \gamma_j(n, U_0, U_2, \mu) \right] \sum_\sigma |\psi_\sigma|^2, \end{aligned} \tag{6.7}$$

where

$$\begin{aligned} \alpha_1(n, U_0, U_2, \mu) &= \frac{n + 2}{3 \delta_{n-1,0;n,1}(U_0, U_2, \mu)}, \\ \alpha_2(n, U_0, U_2, \mu) &= \frac{4(n - 1)}{15 \delta_{n-1,2;n,1}(U_0, U_2, \mu)}, \\ \alpha_3(n, U_0, U_2, \mu) &= \frac{n + 1}{3 \delta_{n+1,0;n,1}(U_0, U_2, \mu)}, \\ \alpha_4(n, U_0, U_2, \mu) &= \frac{4(n + 4)}{15 \delta_{n+1,2;n,1}(U_0, U_2, \mu)}, \end{aligned} \tag{6.8}$$

$$\begin{aligned} \gamma_1(n, U_0, U_2, \mu) &= \frac{n + 3}{\delta_{n+1,1;n,0}(U_0, U_2, \mu)}, \\ \gamma_2(n, U_0, U_2, \mu) &= \frac{n}{\delta_{n-1,1;n,0}(U_0, U_2, \mu)}, \end{aligned} \tag{6.9}$$

and $\delta_{l,r;n,s}(U_0, U_2, \mu) = E_0(l, r, U_0, U_2, \mu) - E_0(s, n, U_0, U_2, \mu)$.

Minimisation of the energy for nonzero SF order parameter is achieved when the expressions in the square brackets in (6.6) and (6.7) are negative. The MI phase is a ground state for those values of parameters for which the minimum is reached for $\psi_i = 0$, that is for positive contents of parentheses (6.6) and (6.7).

All in all the boundary between MF and SF phase is defined by contents of square brackets in Equations (6.6) and (6.7) being zero. This gives the following formulas for the MI-SF phase boundaries:

$$J_{odd} = \frac{1}{z \sum_{j=1,4} \alpha_j(n, U_0, U_2, \mu)}, \tag{6.10}$$

$$J_{even} = \frac{3}{z \sum_{j=1,2} \gamma_j(n, U_0, U_2, \mu)}. \tag{6.11}$$

The analysis of the ferromagnetic regime ($U_2 < 0$) is analogous and yields the answer (the plots are available in [137]):

$$J_{ferro} = -\frac{(n + nU_2 - \mu)\left[(-1 + n)(1 + U_2) - \mu\right]}{z(1 + U_2 + \mu)}. \tag{6.12}$$

The above, ordinary perturbative mean field approach has to be generalized to be applicable to the disordered case. Now $\psi_{j\sigma} = \langle a_{j,\sigma} \rangle$ is explicitly site-dependent. The averaging over disorder may be performed at different levels. Here we choose to average at the level of formula for the energy functional. The averaged main equation for energy reads just as before

$$\begin{aligned} \bar{E}(s, n, J, U_0, U_2, \mu, \bar{\psi}_\sigma) &= \bar{E}_0(s, n, U_0, U_2, \mu) \\ &+ \bar{E}^{(2)}(s, n, J, U_0, U_2, \mu, \bar{\psi}_\sigma), \end{aligned} \tag{6.13}$$

where expression for $\bar{E}, \bar{E}_0, \bar{E}^{(2)}$ is analogous as in (6.5), (6.7), (6.6), but functions α_i and γ_i in (6.8) and (6.9) are integrated over disorder realization (for example if disorder is over $U_2 \in [\bar{U}_2 - \Delta\bar{U}_2, \bar{U}_2 + \Delta\bar{U}_2]$ then $\bar{\alpha}_i = \frac{1}{2\Delta} \int dU_2' \alpha_i(n, U_0, U_2', \mu)$.

Such an approach treats spatial correlation in a trivial way. A more complete analysis needs a more complex theory, such as the Stochastic Mean Field Theory [8]. In such an approach the additional self consistent equation arises $\bar{\psi}_i = \int d\psi P(\psi_i) \langle a_i \rangle$ which takes into account spatial fluctuations. The analysis may also be performed by means of the finite size lattice with some disorder realization (such as real-space Gutzwiller approach discussed in Section 6.1.3), after which limit $L \to \infty$ is taken.

We have used the simplified approach in further disorder studies. In the following Sections (6.2.1) and (6.2.2) the disorder is studied using both real space Gutzwiller ansatz and the simplified mean field approach.

6.1.3 Variational Gutzwiller approach

The Gutzwiller ansatz, described in detail in the Section 1.4.3 has been applied to the Hamiltonian (6.1). Here the ansatz takes the form:

$$|\psi\rangle = \prod_{i=1}^{M} \sum_{n=0}^{n_{max}} g_i(n) \sum_{S=0}^{n} f_i(S,n) \sum_{m=-S}^{S} h_i(S,m,n) \, |S_i, m_i, n_i\rangle \tag{6.14}$$

The spinor Bose-Hubbard Hamiltonian differs from the ordinary BH model by the term proportional to U_2 parameter, which for typical applications satisfies $|U_2| \ll U_0$, but in this thesis we aim for full study of the phase diagram. In interaction-dominated regime the system is in a MI phase, but when tunnelling dominates, the system is in a delocalised SF phase. Although spin-dependent term alters SF-MI phase transition location and is responsible for spin properties of various phases, it does not give birth to additional phases other than MI and SF.

The MI phase prevails for small hopping amplitude and it is defined as gapped, incompressible phase. The compressibilty is defined as $\kappa = \frac{\partial \rho}{\partial \mu} = -\frac{1}{V}\left(\frac{\partial V}{\partial P}\right)_T$ with

$$\rho = \frac{1}{N} \left\langle \sum_j \hat{n}_j \right\rangle, \tag{6.15}$$

and N being the total number of bosons. The SF phase is characterised by long-range correlations and nonzero compressibility, gaplessness. At least two quantities may be used to detect it: the superfluid fraction ρ_S and the condensate fraction ρ_C as described in 1.4.1 and 1.4.3.

The computation was performed for a small lattice, as the Gutzwiller ansatz in the homogeneous (no disorder) case is not subject to finite size effects, like full Hilbert space computation. In Figure 6.2 we show the condensate fraction, ρ_C. As the value of U_2 increases, the lobes with even number of particles in the MI phase expand, in contrast to odd-filled MI lobes which are shrunk. For $U_2 > 0.5U_0$ the odd lobes vanish completely. This corresponds to the $J = 0$ phase diagram in Figure 6.1).

In Figure 6.2 perturbative mean field results are shown as solid black lines. The perturbative mean field and Gutzwiller predictions for the boundaries of the even lobes disagree for small U_2/U_0 as reported in [145]. This deviation appears only if MI-SF transition is first order. To show that we plot in the right column of Figure 6.2 the condensate fraction as a function of J along $\mu = const.$, horizontal lines in the phase diagram, across the MI-SF transition. The chosen values of fixed chemical potential correspond to the vertical position of tips of the Mott Insulator lobes in the Gutzwiller phase diagram. We have found that the perturbative mean field and Gutzwiller ansatz discrepancy occurs if and only if the condensate fraction as a function of tunnelling shows a discontinuity at the phase transition (i.e. the

phase transition is of the first order). The phase transition is clearly first order for $U_2/U_0 \leq 0.1$, and clearly second order for $U_2/U_0 \geq 0.3$ We have estimated that character of the phase transition changes at approximately $U_2/U_0 = u_c \simeq 0.2$. The observation of a first order phase transition in the even lobes - where MI is formed by singlets on each site is not new and has been also pointed out in the mean field analysis of [143, 145] in 2D, as well as in Quantum Monte Carlo (QMC) calculations [146] in 1D.

Investigation of the ground states on both sides of the transition, shows that the reason for the discontinuity is abrupt population on the SF side the phase transition of atomic states with total spin $S = 2$. For $U_2/U_0 \leq 0.1$ the energy gap created by spin excitation is overpowered by the kinetic energy, and nonzero occupation of mode $|S = 2, m, n\rangle$ occurs for even n around the MI tip. For $U_2/U_0 \geq 0.3$ the superfluid is a mixture of states $|S = 0, m, n\rangle$ for even n (in both cases of course there is contribution form $|S = 1, m, n\rangle$ states with n odd).

6.2 Disorder in Spinor Bose-Hubbard Model

The introduction of the disorder in local chemical potential results in the presence of an additional insulating phase, the Bose Glass phase in the phase diagram.

The addition of a site-dependent disorder destroys the translation invariance of the system. Mean field or Gutzwiller ansatz descriptions have reduced the Hamiltonian to a single site description. Such a procedure is no longer possible. Instead, the mean fields $\langle a_{\sigma,i} \rangle$ as well as Gutzwiller wave function coefficients become explicitly site dependent.

Solution of the disordered potential may be achieved by considering large systems with an appropriate ansatz (as exact Hilbert space methods are of course unavailable) or large number of realizations of small systems for which some sort of averaging should take place. In this section we will apply the Gutzwiller ansatz (Section 6.1.3) to a single finite 2D lattice (40×40 sites). We have verified that this size of the lattice allows for self-averaging of the results. We will also use generalisation of the perturbative mean field approach, the Probabilistic Mean Field approach (introduced in Section 6.1.2)

The disorder in the interaction parameters U_0 and U_2 may be experimentally realizable using optical Feshbach resonances [57, 147–149]. The use of magnetic Feshbach resonances seems impossible, as mere switching on of an external magnetic field, would lead to additional terms in the Hamiltonian (the Zeeman hyperfine level splitting). Depending on the strength of the magnetic field, it could also lead to a breakdown of the trapping.

The use of optical Feshbach resonances has other consequences. It typically causes losses due to spontaneous emission from the intermediate state [148, 149]. Coupling to that state is the essence of the optical Feshbach

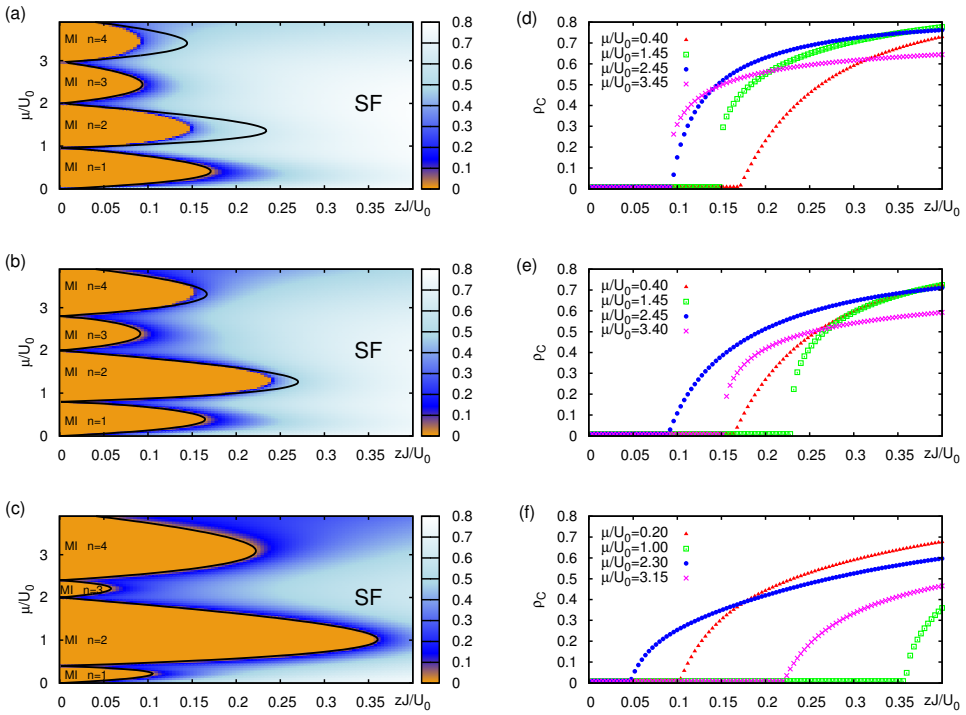

Figure 6.2: Left panels depict the condensate fraction ρ_C obtained numerically by the Gutzwiller ansatz for, (a)$U_2/U_0 = 0.02$, (b)$U_2/U_0 = 0.1$ and (c)$U_2/U_0 = 0.3$, in the homogeneous case without disorder, where MI lobes correspond to vanishing ρ_C (orange areas). The lobes are compared with the boundaries obtained with the MFPT (solid lines). In the right panels is depicted ρ_C as a function of zJ/U_0 for values of μ/U_0 corresponding to the lobes' tips. In the transition between the MI and SF on the tip one can observe a first order transition for the even occupation lobes in panels (d) and (e) (abrupt jump on the condensate fraction) while for lobes corresponding to odd occupation the transition is always of the second order. Image from [137].

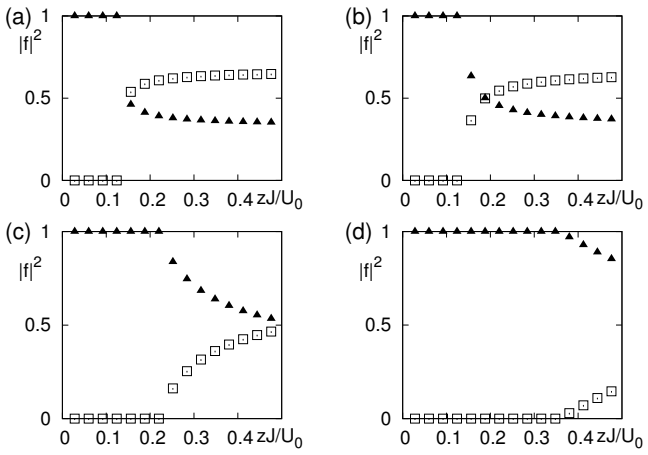

Figure 6.3: Coefficients $|f(S=0,n=2)|^2$ (triangles) and $|f(S=2,n=2)|^2$ (squares) of the Gutzwiller state (6.14) as a function of zJ/U_0. The value μ corresponds to the $n=2$ MI lobe's tip. The panels refer to different values of spin interaction: $U_2/U_0 = 0.01$(a), 0.02(b), 0.1(c) and 0.3(d). Image from [137].

resonance method, so it may not be avoided. If the loses are too serious, the preparation of the ground state may not be possible due to stringent time constraints. In to-date experiments the loses limited system's lifetime up to tens of miliseconds. This is shorter then the disordered sample preparation time in [10] and the physics of the spinor Bose-Hubbard model may be even more subtle due to typically small value of the parameter U_2.

Another possibility is to apply microwave-Feshbach resonance technique, which has been suggested [150–152]. This method uses resonant microwave coupling between different total spin (hyperfine structure) ground state levels to tune the scattering length. No losses due to spontaneous emission are expected.

If the laser (or microwave) EM field is subject to spatial fluctuations, but on average is tuned to the Feshbach resonance, then correlated fluctuations of U_0 and U_2 appear. This is due to correlated alteration of a_0 and a_2 scattering lengths by the values δa_0 and δa_2. To achieve fluctuations only in parameters U_2 and constant U_0 the condition $\delta a_0(\delta\omega) + 2\delta a_2(\delta\omega) \simeq 0$ has to hold.

6.2.1 Disorder in μ

First we study the situation where the disorder is imposed in the chemical potential. It signifies addition to the main Hamiltonian the disorder modification $\hat{H}_{dis}(\epsilon_i) = \epsilon_i \hat{n}_i$. Note that this sort of disorder is called "diagonal disorder". This term is not used here, as it is vague. The disorder imposed

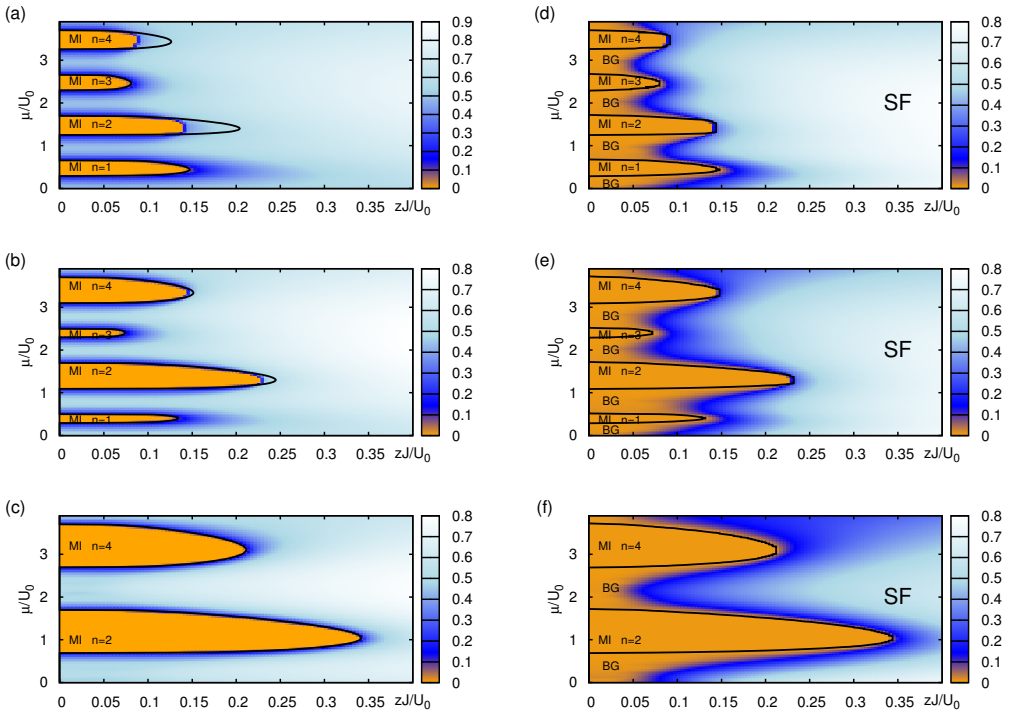

Figure 6.4: Left column panels report the average density fluctuations $\sqrt{\overline{n^2} - \overline{n}^2}$ obtained from the Gutzwiller MF approach. MI lobes, corresponding to vanishing fluctuations (orange areas), are compared with the probabilistic mean field prediction (solid lines). Right column panels show the corresponding condensate fraction in comparison with the Gutzwiller MI lobes (solid lines). The zero-condensate fraction areas (orange areas) outside the MI lobes correspond to BG phase. For all panels, random disorder in the chemical potential with $\Delta = 0.3U_0$ is considered. The different panels correspond $U_2/U_0 = 0.02$ (a-d), $U_2/U_0 = 0.1$ (b-e) and $U_2/U_0 = 0.3$ (c-f). Observe the disappearance of the odd filling MI lobes for the largest U_2/U_0 ratio in agreement with the simple estimate given in text. Image from [137].

on U_0 or U_2 could also be termed diagonal.

The phase diagram again contains MI and SF phases with identical characteristics as in no disorder situation. In addition to them a Bose Glass (BG) phase shows up in the phase diagram. Due to Gutzwiller ansatz limitations, the Bose glass phase has again zero local particle number variance, just as the Mott Insulator. However the key difference is large spatial variation of the occupation — each site has its own integer occupation.

This explains intuitively the properties of the BG phase: integer occupation corresponds to particles localization, still zero gap is achieved in the thermodynamical limit. Indeed, arbitrary low energy excitation is made by dislocating a particle from site i to a (typically distant) site j for which $\epsilon_j \approx \epsilon_i$. We have verified that nonzero global variance of local occupation $\langle n_i \rangle$ (together with $\Delta n_i \approx 0$) characterizes the same region as nonzero compressibility together with zero superfluid fraction ($\rho_S = 0$) criterion.

Finite J results also in finite uncorrelated SF domains (that is groups of neighboring sites with nonzero $\langle a_{i,\sigma} \rangle$). These domains are due to presence of neighbouring sites for which local chemical potential has coincidently value corresponding to the interlobe SF region in the no disorder phase diagram. This behaviour is a purely random occurrence, vanishing in the thermodynamic limit. It also gives no contribution to the superfluid fraction ρ_S even for a finite lattice. The situation alters dramatically if the local SF regions join up to form a single SF region (it is a classical percolation phase transition). This is a mechanism decribing BG-SF phase transition.

The results are shown in Figure 6.4 for fixed disorder amplitude, for a couple or values of U_2. Zero local particle number fluctuations and zero compressibility, determine the extent of Mott Insulator lobes. These quantities are plotted in panels (a-c). Black solid lines signify the results obtained from the Probabilistic Mean Field Approach. Just like in the ordinary BH Hamiltonian, increasing disorder steadily shrinks the Mott Insulator lobes and introduces the BG phase separating them. The extent of the BG phase in the phase diagram is obtained by determining which points in the phase diagram are characterised by nonzero spatial variance of local occupations and zero condensate fraction (ρ_C).

In Figure 6.4, no phase separates tips of the MI phase and the SF region. Therefore this gives rise to a direct SF-MI transition even in the presence of the disorder. Note that the mean field approximation has a tendency to overestimate long range correlations as $\langle a_i a_j^\dagger \rangle = \langle a_i \rangle \langle a_j^\dagger \rangle$ with no regard to relative position of sites i and j. This promotes the false appearance of the SF order (or large condensate fraction). This may be one of the reasons why the BG phase appears only for small J, contrary to theoretical predictions [80]. Recently, quite convincing argument called "theorem of inclusions" has transpired [86]. It seems to have positively settled the long dispute whether the intermediate BG phase has to separate Mott insulating phase from the superfluid phase. It appears that this is the case, despite our numerical

results.

For the even MI lobes the maximal gap for particle-hole excitations is $U_0 + 2U_2$ when $0 < U_2 < 0.5U_0$ while for odd occupation lobes the maximal gap is $U_0 - 2U_2$. Note that here we do not use the most naive definition of a spectral gap that is difference of energies of the first excited state and the ground state (in case of scalar BH these notions are equivalent), as these states differ just by S_i values and are uncoupled by the kinetic energy operator and by the on-site Hamiltonian. Indeed, a spin value S_i is a good quantum number. Therefore the gap here denotes the least energetic separation of states coupled by kinetic energy operator.

Just as in the ordinary BH case the critical disorder value, when imposed in the chemical potential, for the disappearance of any MI lobe is half the value of the maximal gap. For the odd/even occupation lobes it is $\Delta_o = U_0/2 \pm U_2$. If the disorder amplitude is larger, then the MI lobe does not show (it is destroyed by appearance of neighbouring sites with large local energy), and instead the insulator phase is just a BG phase. In Figure 6.4 the panels differ by the values of U_2 which alters the values of critical disorder Δ_o in each row. This parameter for odd lobes from top to bottom row is: $\Delta_o = 0.48U_0$, $0.4U_0$ and $0.2U_0$. The disorder Δ exceeds the critical disorder value Δ_o only for the last row. It is clear that in that case no odd Mott insulator lobes are present at all. In the case of the ordinary BH model all the MI lobes vanished simultaneously.

After the oddly-filled MI lobes have vanished the remaining Bose Glass insulator phase is nematic ($\langle \hat{S}^2 \rangle \neq 0$) for $U_2/U_0 < 0.5$ and it is formed by singlets ($\langle \hat{S}^2 \rangle = 0$) for $U_2/U_0 > 0.5$. To show this we plot the averaged $\langle \hat{S}^2 \rangle$ as a function of μ/U_0, for $zJ/U_0 = 0.02$ and four different values of U_2. The plot is presented in Figure 6.5. The constant values of $\langle \hat{S}^2 \rangle$ in that plot correspond to the MI regions, as may be seen by comparison to Figure 6.4. If $\left\langle \hat{\mathbf{S}}^2 \right\rangle \notin \{0, 2\}$, the system is in the BG phase. For $U_2/U_0 = 0.3$, which in no disorder case allows for existence of the MI lobes, the BG has nematic properties $\langle S_z \rangle = 0, 0 < \langle \hat{S}^2 \rangle < 2$.

For $U_2/U_0 > 0.5$ (in our case $U_2/U_0 = 0.51$ is shown) we have $\langle \hat{S}^2 \rangle = 0$ no matter whether μ/U_0 corresponds to the BG phase or the evenly-filled MI phase. This means that both phases are singlet. This is no surprise for the MI case, as the same properties was described before.

Just like in the no disorder case the Gutzwiller ansatz results agree with the Probabilistic Mean Field Analysis unless we consider a small U_2/U_0 value and even number of particles in the MI lobe. Again the mechanism of this discrepancy is likely to be the same - the first order phase transition.

6.2.2 Disorder in U_2

The disorder in the U_2 parameters will be characterized by random values of the U_2 parameter for each lattice site, that is $U_2^i = U_2 + \epsilon_i$ where ϵ_i

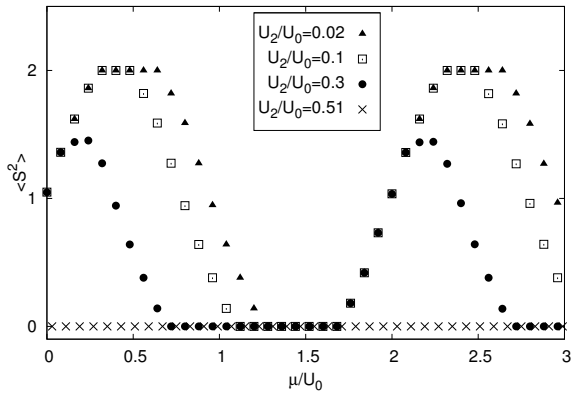

Figure 6.5: Total spin average $\langle \hat{S}^2 \rangle$ as a function of μ/U_0 with $zJ/U_0 = 0.02$ for $U_2/U_0 = 0.02$ (solid triangles), $U_2/U_0 = 0.1$ (empty squares), $U_2/U_0 = 0.3$ (solid circles) and $U_2/U_0 = 0.51$ (crosses). Image from [137].

takes a random value in the interval $[-\Delta, \Delta]$ with uniform distribution and $\Delta < U_2$.

Figure 6.6 shows the $J/U_0 - \mu/U_0$ phase diagram for the U_2-disordered spinor Bose-Hubbard model for parameters $U_2/U_0 = \pm 0.1$ and the disorder amplitude $\Delta/U_0 = 0.06$. In the ferromagnetic case, $U_2 < 0$, (plots (a) and (c)), the phase diagram is similar to the phase diagram with disorder in μ. The MI lobes become smaller and BG phase separates them. Nevertheless there is a key difference. In the case of the disorder in $U_2 < 0$ the BG region width is in fact proportional to the occupation of the MI lobe, not of constant width as in case of disorder in the chemical potential. This is easy to see from Figure 6.1 (and of course it is visible in Figure 6.6 as well). The boundaries separating different MI lobes for $U_2 < 0$ are lines with increasing slope as $n \to \infty$. Disorder in U_2 corresponds to averaging sites which are spread on a vertical segment (of length 2Δ in Figure 6.1). If the occupation of the MI lobe is high enough, it is impossible to draw a vertical interval of that length which fits inside just a single MI region. Then MI phase vanishes completely. So in the ferromagnetic case $U_2 < 0$ there exist finitely many MI lobes, no matter how small Δ is. Naturally this argument is not valid for finite J. The ultimate proof is the numerical analysis. In Figure 6.6(a) one may clearly see that separation of the MI lobes increases with lobe occupation.

New features emerge also in the antiferromagnetic case, $U_2 > 0$. It is shown in plots (b) and (d) in Figure 6.6. One may see that the BG phase is formed only between lobes corresponding to occupation by $2n - 1$ and $2n$, for $n \in \mathbb{N}$. No effect of disorder is visible between $2n$ and $2n + 1$ MI lobes.

Again this feature may be explained in the $J = 0$ limit, when lattice sites are decoupled. The reference figure is again Figure 6.1. For the pure

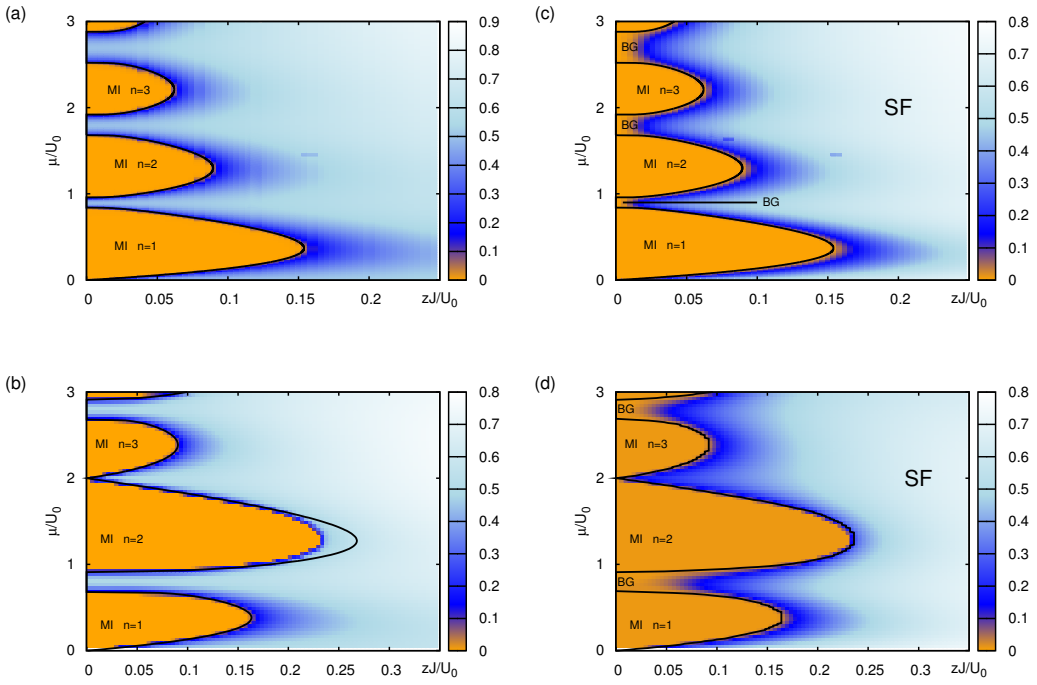

Figure 6.6: Density fluctuations (left panels) and ρ_C (right panels) for $U_2 = \pm 0.1U_0$ and disorder in U_2, $\Delta U_2/U_0 = 0.06$. MI lobes compared with the MF results (solid lines). Vanishing ρ_C outside the MI lobes (solid lines), corresponds to the BG phase. Panels (a) and (c) correspond to the ferromagnetic case $U_2 = -0.1U_0$ (a-c). The case $U_2 = 0.1U_0$ is reported in panels (b) and (d). Image from [137].

U_2 disorder all sites have the same μ and $U_2 \in [-\Delta + \bar{U}_2, \Delta + \bar{U}_2]$ is contained within a single phase in the $J = 0$ phase diagram. If for particular $(\bar{U}_2/U_0, \mu/U_0)$ the segment intersects the phase boundary, then some lattice sites have different occupation and the remaining (and the state is a textbook example of the BG phase). The $2n$-particle to $2n + 1$-particle MI lobe border is characteristic as it is vertical itself in Figure 6.1. This means that as the chemical potential μ/U_0 is changed the vertical interval signifying lattice sites moves horizontally and crosses immediately into another phase. This means that all the sites go immediately from one phase to other and no disordered phase is present. As there are no horizontal boundaries, no such behaviour is possible for disorder in μ. The nontrivial question is whether this BG behaviour is $J = 0$ boundary effect, of a true phase which survives nonzero tunnelling. The numerical simulations support the latter. The data presented in Figure 6.6 clearly show nonzero density fluctuations and zero ρ_C in the relevant interlobe, finite J regions. Additionally for finite J no evidence of BG was detected close to the $2n$-particle to $2n + 1$-particle MI lobe border.

Chapter 7

Finite temperature, real time evolution of the BH Hamiltonian

Absolute zero temperature assumed in previous chapters is an idealization not achievable experimentally, although the temperature in experiments is ultra-low. The study of finite-temperature effects is a necessity both from theoretical and practical reasons. If the goal is to prepare a system in the thermal state, a natural question of thermalization in complex quantum system arises [17, 19, 153–155]. The consensus is that description of non-integrable closed quantum systems, such as interacting ultracold quantum gases in optical lattices with use of thermal density matrix is possible. The purpose of this section is to study dynamics of the Bose-Hubbard model in the finite temperature for realistic systems. To-date investigations focused on dynamics of small systems (in the full Hilbert space), containing at most between 10 and 30 lattice sites and similar number of particles [153] or statics of large systems (by means of Quantum Monte Carlo simulations) composed of up to hundreds of thousands of lattice sites and particles [169]. We have extended the method of Minimally Entangled Typical Thermal States (METTS) proposed in [156] to allow for the real time evolution and inhomogeneous systems.

Until now, to study finite temperature properties complex quantum systems, various mean-field methods have been used [127, 157, 158]. Exactly solvable hardcore-boson case has also been considered [159]. Computation of Helmholtz energy function for a 1D complex quantum system was possible by application of the DMRG [160, 161]. Some results on dynamics of large, experimental size systems were obtained by assuming that the evolution is adiabatic (and therefore conserving entropy) [162]. Using the Local Density Approximation and systematic QMC analysis some conclusions be drawn even for inhomogeneous systems [163].

7.1 BH Hamiltonian in canonical ensemble

The experiments with ultracold atoms are performed in vacuum with a gas trapped in an external potential. In such conditions the gas has little chance to exchange particles or energy with the environment (the external potential is static) provided we neglect spontaneous emission phenomenon, which may be reduced and controlled by a proper sample preparation. Therefore, if the system could be considered "thermal" in any sense, it should be described by the canonical ensemble and its density matrix should be $\rho = \exp(-\beta\mathcal{H})$.

This assumption goes over a serious problem of *thermalization* and *prethermalization* in a isolated ultracold quantum systems in the lattice. Thermalization, mathematically speaking, is not possible in an isolated system, described by a time-independent Hamiltonian. If the density matrix ρ is not thermal initially, the unitary evolution $\rho \to \exp(-i/\hbar Ht)\rho\exp(i/\hbar Ht)$ may not lead to the thermal matrix $\rho_{th} = \sum \exp(-\beta E_n)|n\rangle\langle n|$ after a finite time as this matrix is invariant under forward and backward real time evolution. Another problem may be the existence of nontrivial integrals of motion in case of integrable systems [164].

Typically thermalization in a closed complex quantum system is interpreted locally. The density matrix of the whole system $\rho(t)$ is first reduced to a small subsystem of length L' where $1 \ll L' \ll L$, $\rho^{L'} = \mathrm{Tr}_{L\setminus L'}\rho$. If the evolution time t is large enough, and the system is to be tested for being thermalized, $\rho^{L'}$ is compared to a thermal density matrix that is $\rho'^{L} \approx \exp(-\beta H_{L'})$. We neglect coupling of $H_{L'}$ to the to remaining sites as $1 \ll L'$ [165]. Equivalently, the "thermalized" quantum complex system should correctly predict averages of local observables (such as $\hat{n}_i, \hat{n}_i^2$) and almost local ones (such as $\langle n_i n_{i+1}\rangle$), but is expected to fail for long range correlators $\langle n_i n_j^\dagger\rangle$, for $|i-j|$ - large. Further effects have been reviewed in [166].

7.2 METTS

Quantum Monte Carlo algorithms allow for a very efficient computation of averages of local operators $\langle A\rangle = \mathrm{Tr}\rho A$ even for lattice systems consisting of thousands of particles in thousands of lattice sites, but yield no mathematical representation of the density matrix itself [65]. The evolution operator $U(t) = \exp(-iHt)$ is a highly nonlocal, nondiagonal (in any basis that may be used) operator. The time evolution of averages is described by $\langle A(t)\rangle = \mathrm{Tr}U(t)AU^\dagger(t)\rho$, where ρ is a density matrix of a state that is computable by means of the QMC. Calculating such an average is out of reach for the QMC.

The METTS method proposed in [156] goes beyond that as it enables to generate a sample $\mathcal{R}$ of wavevectors ψ_i which allow for computation of

thermal averages as:

$$\langle A\rangle_{th} \approx \langle A\rangle_{\mathcal{R}} = \sum_{\psi_i\in\mathcal{R}} \langle\psi_i|A|\psi_i\rangle. \tag{7.1}$$

Following [156], let us sketch how the set $\mathcal{R}$ is constructed. The trace formula for thermal average is:

$$\langle A\rangle_{th} = \sum_i \langle i|\exp\left(-\frac{\beta}{2}H\right) A \exp\left(-\frac{\beta}{2}H\right)|i\rangle, \tag{7.2}$$

where $|i\rangle$ go over set of all Fock states. Equivalently:

$$\begin{aligned}
\langle A\rangle_{th} &= \sum_i \frac{P(i)}{Z}\langle\phi(i)|A|\phi(i)\rangle, &(7.3)\\
Z &= \sum_i P(i), &(7.4)\\
|\psi(i)\rangle &= \frac{1}{\sqrt{P(i)}}|\exp\left(-\frac{\beta}{2}H\right)|i\rangle. &(7.5)
\end{aligned}$$

Thus it suffices to perform a Monte Carlo sampling of the last sum, and generate a subset $\mathcal{S}$ of all Fock states to which the above summation may be restricted. Then $\mathcal{R} = \exp(-\beta/2H)\mathcal{S}$. Notation $\beta/2H)\mathcal{S}$ is understood as elementwise application of the operator $\exp(-\beta/2H)$ on the set $\mathcal{S}$.

The only requirements for generating such a sample of vectors are: a) the ability to perform a short time evolution of any vector ψ in the imaginary time: $\psi(i\beta/2) = \exp(-\frac{\beta}{2}\mathcal{H})\psi(0)$; b) the ability to perform quantum measurement on the state $\psi(i\beta/2)$ i.e. a projection on some orthonormal basis (for example Fock states basis). It turns out that MPS states representation together with the TEBD algorithm satisfies both requirements as is shown in the Appendix 9.5. Moreover such a representation enables to compute $\langle\exp(iHt)A\exp(-iHt)\rangle_{\mathcal{R}}$ for any local enough operator A. Indeed $\langle A(t)\rangle_{\mathcal{R}} = \langle A\rangle_{\exp(-iHt)\mathcal{R}}$. Therefore, by evolving separately the constituents of $\mathcal{R}$, the METTS methods allows in theory to compute evolution of operator averages for large lattice systems.

The basic algorithm for preparing an ensemble of METTS vectors is:

The above algorithm is a MC random walk and as such it produces best approximation with fixed number of elements of the full ensemble if the random walk traverses efficiently the configuration space. For low J/U ratio, at unit filling, the Fock states are almost eigenstates. Thus in that regime the imaginary time evolution followed by the projection to a Fock state does not stray far from the identity operation. The inner loop in the METTS algorithm often does not change the state ψ thus reducing the efficiency of the random walk. If in addition to the small J, the inverse temperature β is large enough (i.e. the sample is cold enough) then the

Algorithm 1: Generate METTS ensemble of M vectors, sampling every K sweeps with initial I_0 thermalization sweeps, inverse temperature β and a Hamiltonian $\mathcal{H}$.

```
ψ → ground state if Hamiltonian H
for i = −I_0, M do
  if i > 0 then
    for j = 1, K do
      project ψ to a Fock state η with probability |⟨η|ψ⟩|^2
      ψ → exp(−(β/2)Ht)ψ
    end for
    enter ψ into the ensemble
  end if
end for
```

evolution by the imaginary time $\beta/2$ leads to the Fock eingenstate dressed in quantum fluctuations (amount of which is proportional to J^2 for small J/U). This is visualized in Figure 7.1. For small β the recurrence probability convergence to 1, for larger β the probability saturates to a value which is characterised by quantum fluctuations of the eigenstate. For ultralarge β every state evolved in the imaginary time for time $\beta/2$ converges to the ground state. Such hyperlow temperatures are of no interest to us.

In the beginning of the each step of the METTS ensemble generating algorithm the state is $\psi_{\vec{n}}^M = \exp(-\beta/2H)|\vec{n}\rangle$, where vector $\vec{n} = (n_1, \ldots, n_L)$ characterizes actual Fock state occupation. After several evolution and projection steps in the inner loop of Algorithm 1 the state $\psi_{\vec{n}}^M$ is updated and entered into the ensemble. For best efficiency, two subsequent vectors which have been entered into the ensemble $\psi_{\vec{n}}^M, \psi_{\vec{n}'}^M$ should be characterised by independent generating vectors $\vec{n}, \vec{n}'$. Thus, in case of the Bose-Hubbard model, large values of K have to be used. For thermodynamics of the MI phase for J of the order of $0.05 - 0.2$ and β in the range of $6 - 12$, we have estimated that choosing K between 150 and 500 is sufficient for generating vectors' decorrelation. In the low temperature, MI regime the generating vectors are characterised by vectors $\vec{n}$ with equal integer filling, except for a few sites where particle hole excitations are present.

The following sections are organized as follows. Section 7.3 presents a comparison of METTS and QMC algorithms for static thermal averages evaluations. Section 7.4 contains a discussion notion of inhomogeneous system preparation by both QMC and METTS algorithms. Section 7.6 deals with the real time evolution of such systems.

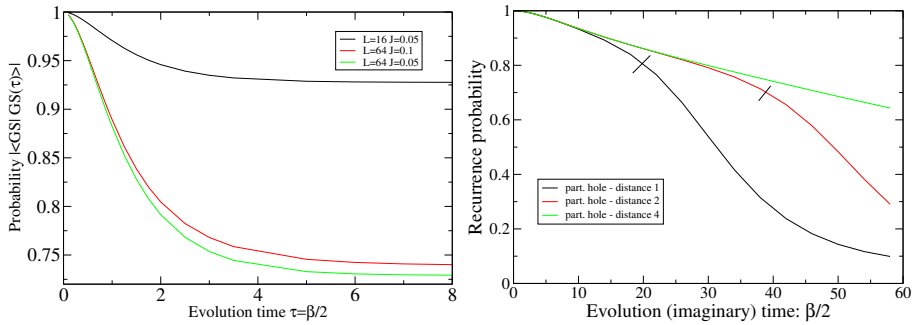

Figure 7.1: Left panel: the probability of projecting the state $\exp(-\beta/2H)\psi_0$, there ψ_0 is a unit-filled Fock state onto ψ_0 in the METTS algorithm. For different lattice sizes L and different J. The right panel shows the analogous probability of projection of a state $\exp(-\beta/2H)\psi_d$ to a state ψ_d, where ψ_d is a Fock state ψ_0 with particle excited from a site $L/2 - \lceil d/2 \rceil$ to a site $L/2 - \lceil d/2 \rceil + d$. The perpendicular short line denotes the approximate location of the inflection point, which marks transition to the hypercold regime when the projected state is close to the ground state.

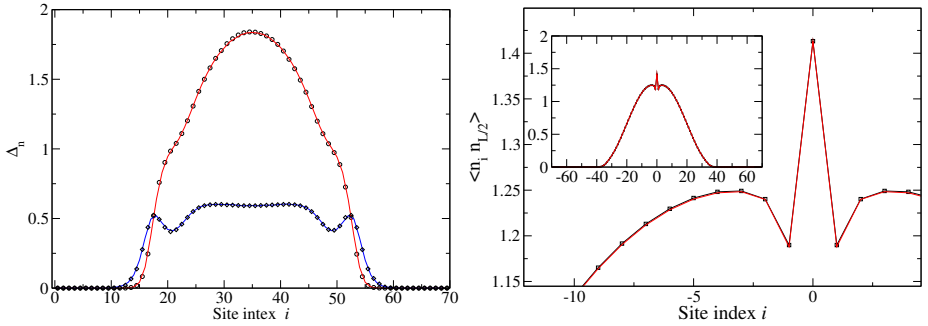

Figure 7.2: Left panel: density profiles and particle number variation Δ_n of gas of bosons in a harmonic trap. Parameters: $\beta = 10, J = 0.13, U = 1, N = 50, L = 70, \kappa = 0.004$. Color curves — QMC data, black circles: METTS data. Here ensemble of 10000 METTS was used, with $K = 1000$. The bond dimension used was $\chi = 8$. Right panel: correlation function $\langle n_i n_j \rangle$ for the same setup functions with fixed i at center of the trap.

7.3 METTS vs QMC

Both approaches: METTS and QMC describe the complex quantum system using the same Hilbert space. Still the two are very different. The QMC samples the formula for the partition function $Z = \mathrm{Tr}(\exp(-\beta H))$ by generating a large (typically 10^8 and more) sample of "worldlines"

$$\begin{aligned} Z = \mathrm{Tr}(\exp(-\beta H)) &= \mathrm{Tr}\mathcal{P}\exp\left(-\int_0^\beta T(\tau)d\tau\right) \\ &= \sum_{m=0}^{\infty}\sum_{i_1,\ldots,i_m}\int_0^\beta d\tau_1\ldots\int_{\tau_{m-1}}^\beta d\tau_m T(\tau_1)\ldots T(\tau_m) \\ &= \sum_{m=0}^{\infty}\sum_{i_1,\ldots,i_m} e^{-\beta E_{i_1}}\int_0^\beta d\tau_1\ldots\int_{\tau_{m-1}}^\beta d\tau_m \cdot \\ &\cdot(e^{-\tau_1 E_{i_1}}T_{i_1 i_2}e^{\tau_1 E_{i_2}})\ldots(e^{-\tau_m E_{i_m}}T_{i_m i_1}e^{\tau_m E_{i_1}}), \end{aligned} \tag{7.6}$$

where $\hat{T}$ is a nondiagonal part of the Hamiltonian (1.9). The last equation is obtained by inserting partitions of unity $1 = \sum |\psi_i^0\rangle\langle\psi_i^0|$. Here E_i's are eigenenergies and ψ_i^0's are eigenvectors of H_0 — the diagonal part of (1.9). All in all a "worldline" is a set of intermediate states $\psi_1^0, \ldots, \psi_m^0$ and times $\tau_1, \ldots, \tau_m$ which are used in the above summation. Using a classical Markov process to sample worldlines does not enable to sample over all configurations, as topological limitations apply to the MC random walk. The worm algorithm [167] enables to sample over all worldlines.

In contrast, the METTS samples consist of many-body vectors, elements of the full Hilbert space. Due to technical reasons and time constraints the largest size of the METTS ensemble that may be used consists of the order of 10000 vectors.

The ALPS enables to calculate expectations and correlations of diagonal operators. We have used it to calculate: $\langle\hat{n}_i\rangle, \langle\hat{n}_i^2\rangle, \langle\hat{n}_i\hat{n}_j\rangle$ for the trapped system. The detailed comparison with the same quantities obtained using METTS approach is presented in Figure 7.2. Clearly agreement of METTS and QMC predictions has been reached.

Figure 7.3 shows comparison of variances Δn_i computed by the METTS and QMC methods in the homogeneous case. Due to high CPU time cost, only a few METTS points have been calculated. This test has been performed using $L = 100$ sites with open boundary conditions. When calculating the single site occupation variance, the average was computed averaging both over METTS ensemble and the lattice sites. The latter is motivated by the fact that in the homogeneous systems $\langle n_i\rangle, \langle n_i^2\rangle$ should be largely site-independent (except for a few sites close to the boundary). In out example sites $1-5, 95-100$ have been neglected in estimating local observable values.

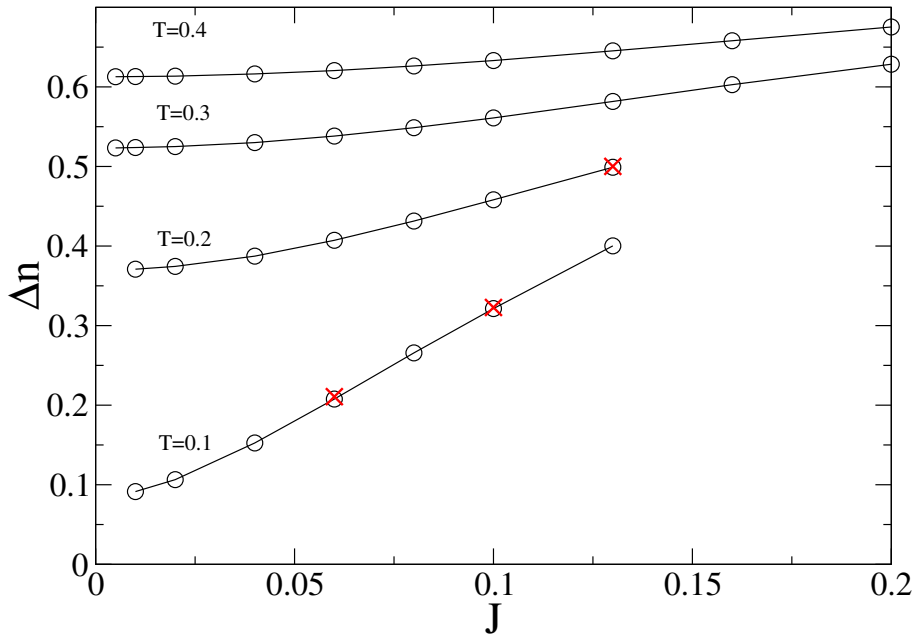

Figure 7.3: Variation of local number of particles Δn as a function of J for different temperatures T. Curves for several J- values are shown. Black line denotes QMC results in canonical ensemble ($N = 100, M = 1000, K = 1000$), red crosses denote METTS results. Homogeneous system was considered, the particle number fluctuation both in QMC and METTS is found out as an average over the whole lattice with exception of 5 sites close to borders.

7.4 T-inhomogeneous systems

In this section we deal with the notion and description of T-inhomogeneous systems. Here inhomogeneity does not mean anymore that the system's Hamiltonian is translationally invariant but that the system has an inhomogeneous initial temperature distribution. The Hamiltonian is assumed to be translationally invariant. We assume that the whole system has two (in general several) regions, here called A and B in which the reduced density matrices $\rho^A = \mathrm{Tr}_B\rho$ and $\rho^B = \mathrm{Tr}_A\rho$ are thermal but with different inverse temperatures — β_1 and β_2. Let us investigate possibilities for obtaining such a system in the standard QMC and METTS computations (in which the temperature is inherently uniform).

If we assume that parts A and B are uncoupled and consider a following Hamiltonian of the form:

$$H = H_A + H_B, \tag{7.7}$$

then its density matrix factorizes as $\rho = \exp(-\beta H) = \exp(-\beta H_A)\otimes\exp(-\beta H_B)$, and $\rho^A = \exp(-\beta H_A)$, $\rho^B = \exp(-\beta H_B)$. Now if we consider a Hamiltonian:

$$H = H_A + \frac{\beta_2}{\beta_1}H_B, \tag{7.8}$$

then the system prepared with such a Hamiltonian with uniform temperature β_1 is described by reduced density matrices is thermal with unequal temperatures, from Hamiltonian's $H_A + H_B$ point of view :

$$\rho^A = \exp(-\beta_1 H_A) \text{ and } \rho^B = \exp(-\beta_2 H_B). \tag{7.9}$$

This approach no longer works if regions A and B are coupled. However the coupling may be neglected if the system is large (and finite size intermediate region is not important in the thermodynamic limit). In the case of Bose-Hubbard model (1.9), if we work in a low tunnelling regime, at integer filling then the thermal state is approximately a product of single site density matrices: $\rho \approx \prod_{i=0}^{L}\exp(-\beta_i H_i)$. The correlation function $\langle a_i a_j^\dagger\rangle$ vanishes exponentially as $|i-j| \to \infty$.

Instead of brute-force merging of two regions (7.8), we chose a more subtle approach. In the case of the Bose-Hubbard Hamiltonian (1.9), we may write the Hamiltonian $\mathcal{H}_{BH}$ as:

$$\mathcal{H}_{BH} = \sum_i H(i) + \sum_i H(i, i+1). \tag{7.10}$$

Instead of (7.8) we define an auxiliary Hamiltonian:

$$f(\mathcal{H}_{BH}) := \sum_i f(i)H(i) + \sum_i \frac{f(i)+f(i+1)}{2}H(i,i+1) - \sum_i g(i)\mu n_i, \tag{7.11}$$

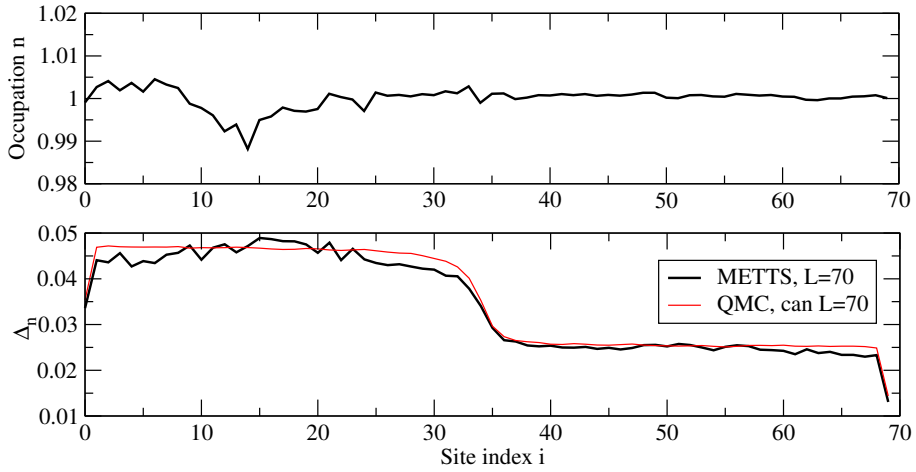

Figure 7.4: Comparison of fluctuations of local number of particles within QMC and METTS for $\beta_1 = 8, \beta_2 = 12, J = 0.05$. Note that the METTS data show significant spatial inhomogenity. This effect is due to finite ensemble size of 12000 METTS vectors.

where $f|_A \approx 1$, $f|_B \approx \frac{\beta_2}{\beta_1}$, $f|_C$ — should be a smooth interpolation between 1 and $\frac{\beta_2}{\beta_1}$, where C is a space between regions A and B.

We have used

$$f(i) = 1 + \left(\frac{\beta_2}{\beta_1} - 1\right) g(i), \quad g(i) = \frac{1}{2}\left(\tanh(is/L) + 1\right), \tag{7.12}$$

where parameter s controls the "steepness" of the gluing.

We expect property (7.9) to hold too, but to verify it, we have to resort to numerical computation. Instead of computing the density matrices of a subsystem and check whether they are thermal, we choose to check if several local observables agree with thermal predictions.

Of interest are primarily operators $\hat{n}, \hat{n}^2, \hat{a}_i\hat{a}_j^\dagger$ as these operators appear in Hamiltonian (and therefore govern the dynamics). Due to technical reasons thermal average of $\langle \hat{a}_i\hat{a}_j^\dagger \rangle$ may not be compared with QMC computation, unlike other operators.

If both inhomogeneous and reference systems are in the thermodynamical limit, the averages have to be equal (otherwise, the method is invalid). However if the analyzed T-inhomogeneous system is not in the thermodynamical limit, but has rather small length L, tt is unclear then how long the reference system should be. In particular we have observed that if half of a chain lattice is set up at particular inverse temperature β_1, then the average of $\langle n_i^2 \rangle$ noticeably depends on the inverse temperature of the chain in the other halve. Only in thermodynamical limit this long range correlation vanishes.

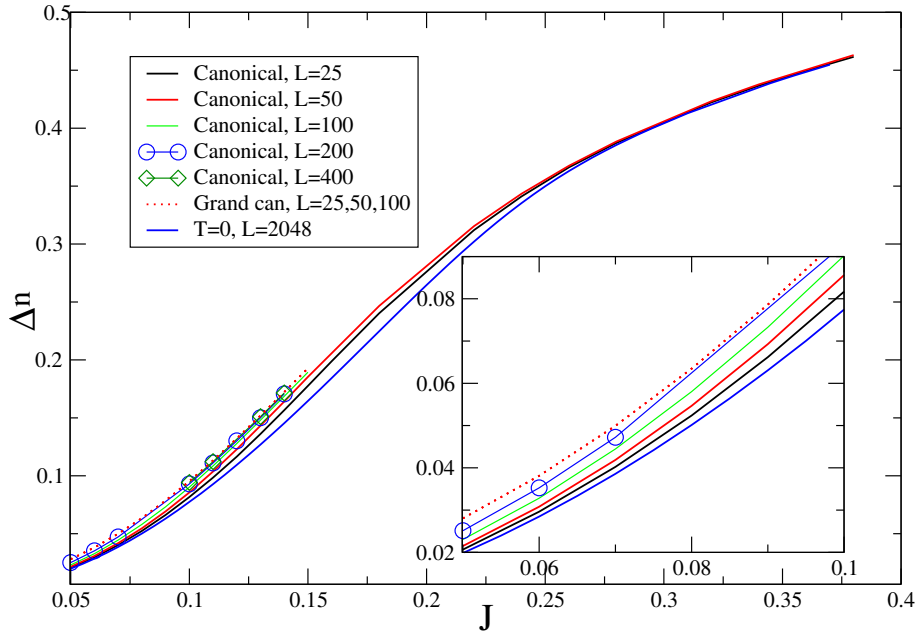

Figure 7.5: Comparison of predictions for variance of number of particles $\Delta n_i = \langle \hat{n}_i^2 \rangle - \langle \hat{n}_i \rangle^2$ calculated within canonical and grand canonical ensembles, by QMC, under periodic boundary conditions for inverse temperature $\beta = 12$.

Figures 7.5 and 7.6 shows a comparison of expected Var $n_{L/2}$ for a homogeneous system with temperature $\beta = 12$ or $\beta = 6$ for lattices of various lengths computed within the canonical and grand canonical ensembles under periodic boundary conditions. It is clear that for both temperatures the thermodynamical limit is reached for approximately $L = 200$ sites long lattice, and the grand canonical ensemble seems to very quickly converge to the thermodynamical limit, as the predictions very weakly depend on lattice length, and canonical ensemble results coincide only for $L > 200$.

7.5 Thermometry

In the following section we are interested in determining the local temperature of the METTS ensemble both at the initial time and for an evolved ensemble.

The initial states for our considerations are always thermal states prepared by the METTS procedure using the auxiliary Hamiltonian (7.11). As we have used the parameters $J = 0.05, U = 1$ it is expected that the local density approximation is applicable due to low tunnelling and the state's local temperature may be defined using the function $f(i)$ from Eq. (7.12) as $\beta_1 f(i)$.

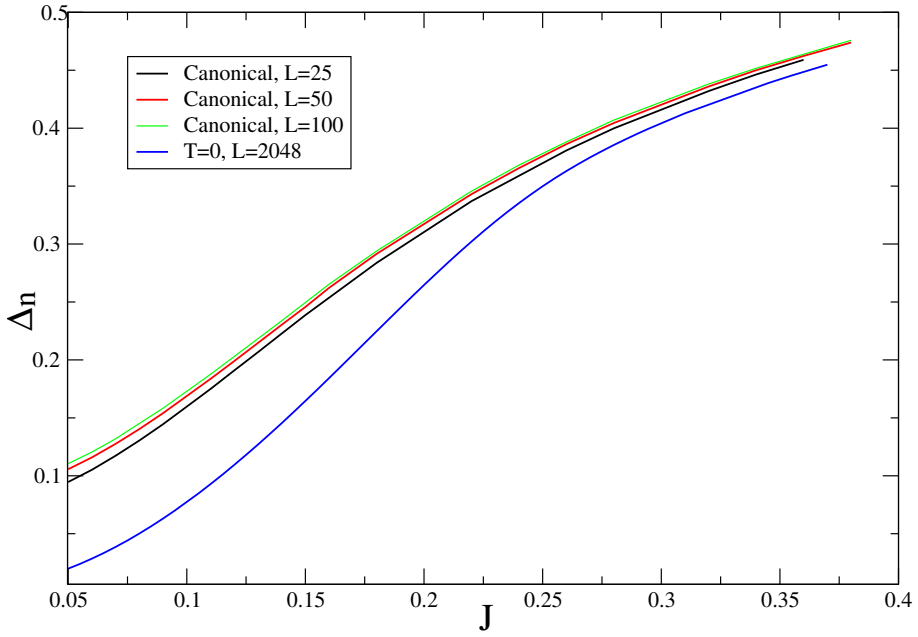

Figure 7.6: Comparison of predictions for variance of number of particles $\Delta n_i = \langle \hat{n}_i^2 \rangle - \langle \hat{n}_i \rangle^2$ calculated within canonical ensembles, by QMC, and TEBD (for $T = 0$ curve) under periodic boundary conditions for inverse temperature $\beta = 6$.

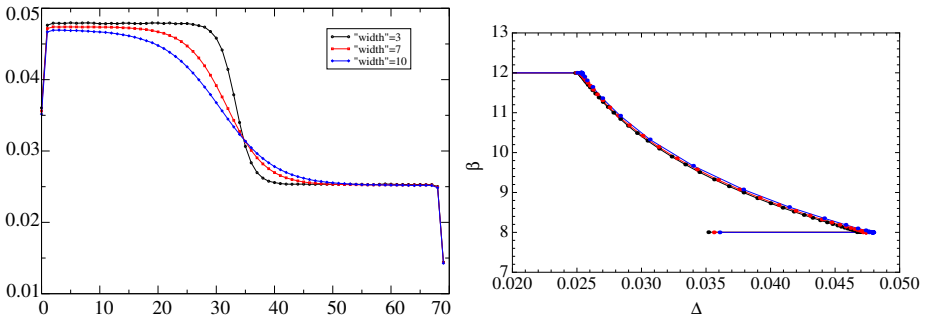

Figure 7.7: Comparison of thermometers defined by the comparison of QMC variation of number of particles Δ_n with the assumed local temperature $\beta(x) = f(x)\beta_1$ (see Eq. (7.12)) for $\beta_1 = 8, \beta_2 = 12$ for $L = 70$ sites for different widths of smoothing interface. As may be seen the LDA works very well.

If a mean of a local quantity $\langle A_i \rangle_{th}$ (note that A_i is not defined here to be an operator) is estimated over all sites of a T-inhomogeneous lattice, then one may map a local inverse temperature β_i to the appropriate average $\langle A_i \rangle_{th}$. This gives the function $\bar{A}(\beta_i)$. It also defines a thermometer — in any situation where we believe the system is "locally thermal" we may infer

the local temperature by the inverse map:

$$T_i = \frac{1}{\bar{A}^{-1}(\langle \hat{A}_i \rangle_{\mathcal{R}})}. \tag{7.13}$$

We have used the particle number variance $\langle A_i \rangle = \langle n_i^2 \rangle - \langle n_i \rangle^2$ as the local quantity defining the thermometer (note again that we do not require the existence of "variance operator"). The thermometer is shown in Figure 7.7 for the case of $\beta_1 = 8, \beta_2 = 12, J = 0.05, s = 60, N = L = 70$.

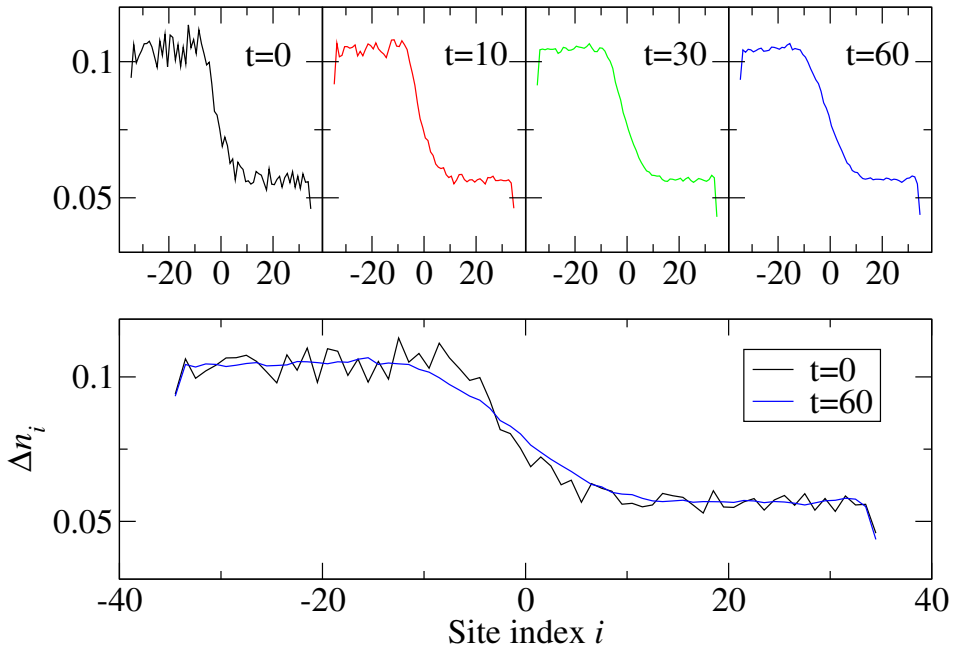

Figure 7.8: Variation of number of particles Δn_i per site evolved in the real time for $\beta_1 = 6$ and $\beta_2 = 8$. The snapshots have been taken at times $t = 0, 10, 30, 60\hbar/E_R$. The plots show smoothening of the variation of particles dependence on site and thermal relaxation in the central region. This dynamics is basis for estimating the diffusion constant for the gas described by the BH model.

7.6 Inhomogeneous out of equilibrium systems evolution

7.6.1 Classical heat equation

The dynamics of thermal conductance in the classical physics is described by a classical heat equation:

$$u_t = Du_{xx}, \quad u(x,t) = f(x), \tag{7.14}$$

where function $u(x,t)$ describes the temperature of medium at each point of space and at each time. The D is a diffusion constant. The heat equation has a remarkable property that for $t > 0$ the function $u(\cdot,t)$ is $\mathcal{C}^\infty(\mathbb{R})$ as a function of space coordinate. The solution of the heat equation is obtained by looking for a Green function of a real line:

$$u(x,t) = \int\limits_{\mathbb{R}} \frac{f(y)}{\sqrt{4Dt}} \exp\left(-\frac{(x-y)^2}{4Dt}\right) \mathrm{d}y. \tag{7.15}$$

Let $u(x,t)$ be a solution of Eq. (7.14) given by the above equation with a diffusion constant D. Let us notice that then $(x,t) \to u(x, \frac{D'}{D}t)$ is a solution of the heat equation with the diffusion constant D' and the same initial condition $x \to u(x,0)$. It means that rescaling time of a solution of the heat equation is equivalent to changing the values of the diffusion constant.

7.6.2 Quantum evolution

The real time evolution of the METTS ensemble is performed by time-evolution of the each of METTS vectors constituting the ensemble. The initial condition is set by the initial METTS ensemble consisting of two smoothly connected Mott Insulators as presented in Section 7.6. The METTS initial condition is characterised by noticeable spatial variation of predicted local particle number variance (see Fig. 7.8). This is due to much smaller number of METTS vectors than typical number of QMC trajectories. We use the function (7.13) to map the particle number variance to the local temperature. For the initial condition the local temperature is defined by the function $\beta_1 f(i)$ (with f being a smoothing function defined in Eq (7.12). Let us denote this numerical solution by $T^M(x,t)$.

For the METTS ensemble the local temperature is measured with the thermometer defined in Section 7.5. We compare the local temperature calculated for the METTS ensemble evolving in time with the solution of the heat equation $u(x,t)$ initialized with $u(x,0) = f(x)\beta_1$ with diffusion constant $D = 1$. That is we look for the time t such that $u(x,t')$ resembles $T^M(x,t)$ the most. The ratio t'/t gives an estimate for the diffusion constant that would have to be used in the heat equation to achieve coherent predictions for the local temperature in both methods. In such case no time rescaling should be necessary, in accordance to the remarks made at the end of the Section 7.6.1.

To define the diffusion constant, we have prepared four samples each consisting of two Mott Insulator glued together. One of insulators was prepared with the inverse temperature β_1 the other with β_2 for $(\beta_1,\beta_2) \in \{(6,8),(7,9),(8,10),(9,11)\}$. The chain length was $L = 70$, the tunnelling parameter was $J/U = 0.05$. We have evolved the system in the real time for $t_{fin} = 60\hbar/E_R$. We compared the time snapshots with the heat equation

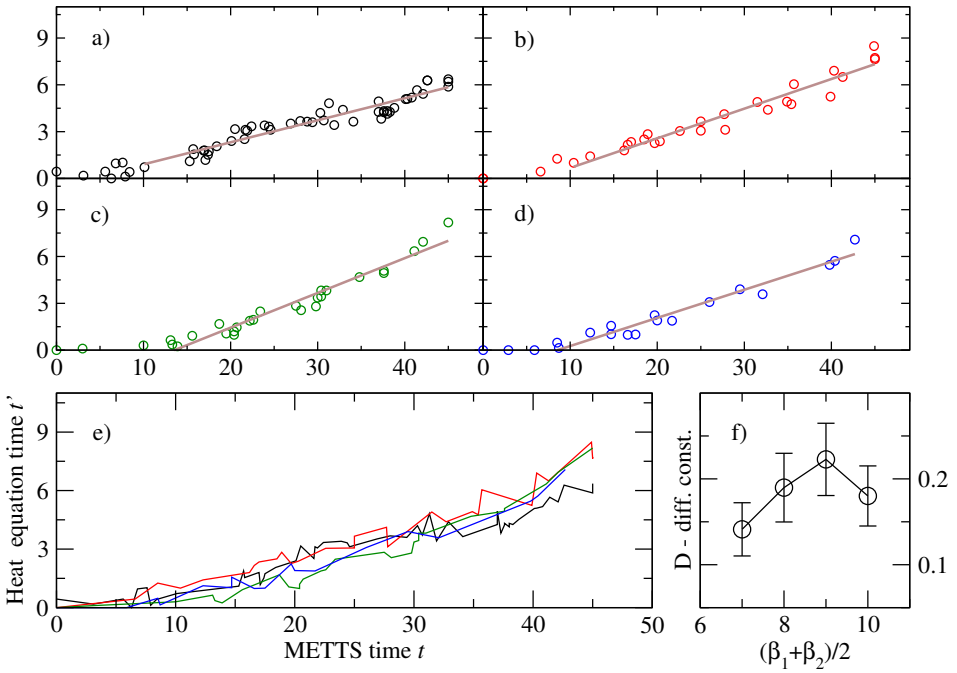

Figure 7.9: Dynamics of the T-inhomogeneous system for $J = 0.05$. Panels a)-d) show dependence of best match of heat equation time t' (axis Y) against real time METTS solution (axis X) for T-inhomogenous systems with $(\beta_1, \beta_2) \in \{(6,8),(7,9),(8,10),(9,11)\}$ respectively. Panel e) shows all the curves from panels a)-d) together. Slope of each curve gives the estimate for the dimensionless thermal conductivity parameter D, Eq. (7.14). For dimensionful version, see text.

solutions for each time t. We determine time t' in which heat equation solution $u(x,t)$ resembles the METTS solution T^M S most. For different times t we collect the point (t,t') for each sample and show them in one plot see Figure 7.9. If the real time evolution of the METTS samples is described well by the heat equation the, dependence of t' as a function of t should be linear. This is a case as one may observe in panels a)-d) of the Figure 7.9. The slope of the linear dependence of t' on t gives the D parameter, the dimensionless heat conductivity. The units in which one works assumes that the time unit is $\hbar/E_r$ and the length unit is the distance between nearest lattice sites (note that for the Wannier function calculation we use a different length unit).

The Figure 7.9 contains situations in which the both ends are in rather normal gas situation and the other end of another sample is in ultracold distance.The dependence of the dimensionless conductivity parameter D with the mid inverse temperature $\beta = (\beta_1+\beta_2)/2$ is nonexistent or slowly increasing as presented in panel f) of the Figure 7.9. The dimensionless parameter

D is related to the full dimensionful thermal conductivity parameter D_f by the relation

$$D_f = \frac{Da^2}{\hbar/E_r} = \frac{D\hbar\pi^2}{2m}, \tag{7.16}$$

where m is a mass of the atom of the considered species. For the transverse lattice of height $40E_r$ the ratio $J/U = 0.05$ corresponds to approximately $s_x \approx 9.5E_r$ for which the value of the U parameter is $U \approx 0.44$. The inverse temperature range 7-10 from Figure 7.9 in dimensionless units corresponds to the range of 6.8-10.8 nK. In this range the transition from ground state-dominated thermal system to a truly finite-temperature system occurs. Using Eq. (7.16) we arrive at $D_f/D = 3.58 \cdot 10^{-9}\mathrm{m}^2/\mathrm{s}$ for Hamiltonian which in recoil units has $J/U = 0.05$ taking into account the physical potential keeping the U/J ratio we arrive finally at:

$$D_f = D \times 1.55 \cdot 10^{-9}\mathrm{m}^2/\mathrm{s}, \tag{7.17}$$

where D is the dimensionless parameter found (Figure 7.9) in the convenient system of units given by energy recoil unit and $k_B = 1$.

We have also studied what is the dependence of the diffusion constant D on the tunnelling amplitude J. To this end we have again prepared a T-inhomogeneous system with the smoothing function f as in (Eqn. 7.12). We have chosen $\beta_1 = 8$ and $\beta_2 = 12$, and prepared the samples for two values of the tunnelling amplitude $J = 0.05, 0.12$. We used the thermometer defined by local particle number variance and determined the local temperature. Again we have compared diffusion of the local temperature determined by the METTS ensemble evolved in real time to the local temperature predicted by heat equation with diffusion constant $D = 1$. The Figure 7.10 shows the matching pairs (t, t') for both cases. The METTS evolution time for the $J = 0.12$ was rescaled by a factor $0.12/0.05 = 2.4$, which led to the overlap of both sets of points (t, t'). This signifies that diffusion coefficient for $J = 0.12$ is approximately 2.4 times larger than for $J = 0.05$. Obviously $D = 0$ if $J = 0$. This means that dependence of D on J is most probably linear in the Mott insulator phase. This conclusion should be scrutinised by additional simulations.

7.7 Final evolution remarks

The METTS method for generating ensembles which approximate the thermal density matrix enables to study complex quantum systems in finite temperature, compute averages of non-local operators. Our proposal to use it as a basis for real-time dynamics simulation has been relatively successful. However, the method is limited seriously by the rapid growth of entanglement while evolving the states in the MPS form by the TEBD or

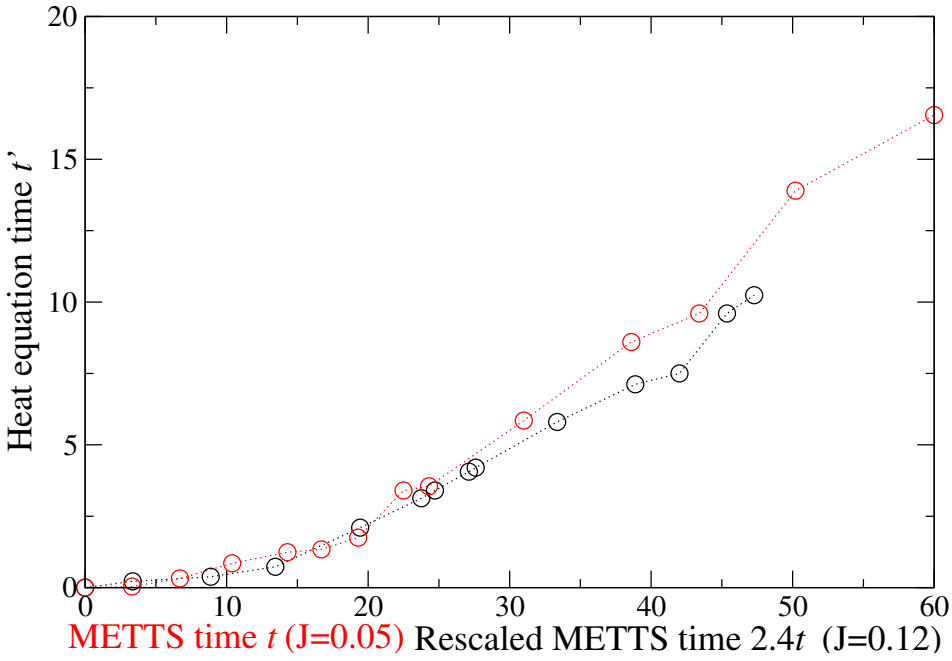

Figure 7.10: Analysis of dependence of the diffusion constant describing a thermal equilibration in the Bose-Hubbard model on the tunnelling parameter J. Both families of points denote sets of matching times (t, t') (one for $J = 0.05$ the other for $J = 0.12$). The member points signify that the METTS evolution time t reflects heat equation evolution with total duration t'. The slope of the line approximating the curves approximates the diffusion constant D. Clearly after rescaling the METTS evolution time for $J = 0.12$ by the ratio $0.12/0.05 = 2.4$ the slope is the same as of unscaled curve $J = 0.05$. This signifies that D depends approximately linearly on J (the third point is $D = 0$ for $J = 0$).

t-DMRG algorithm. The evolved states, constituents of the METTS ensemble, contain in general many excitations states and are therefore difficult to propagate using the TEBD algorithm.

Another, perhaps the most spectacular drawback of the method is heavy use of computational power. The single METTS ensemble consists of $\sim 10^5$ MPS vectors. The rising entanglement necessitated use of bond dimension up to $\chi = 80$ for the TEBD simulations (although the initial METTS ensemble represented with $\chi = 10 - 15$). All in all evolution of a single ensemble of length $L = 70$ cost approximately a week of computation of PL-Grid's Zeus supercomputer taking 160 Intel Xeon cores at the same time.

Although it may be reckoned that at high temperatures the quantum entanglement is limited by thermal effects, we found this claim not to be the case in the METTS systems simulations. The entanglement growth as the time progresses is profound for states forming the METTS ensembles

with higher temperatures. The main reason is that the states being evolved are in fact pure states, which form the thermal density matrix only after summing them up. The higher the temperature the closer the operator $\exp(-\beta/2H)$ is to the identity operator and the further the METTS state $\exp(-\beta/2H)|\text{Fock}\rangle$ from the eigenstate. This has a tendency to enhance difficulty of stable real time evolution problem.

It has been suggested [168] that as the METTS states are being evolved, the quality of approximation of the thermal density matrix by the METTS ensemble deteriorates. We have been unable to notice such effects. Moreover we have determined, while studying our T-inhomogeneous systems, that sites far from the inhomogeneous region have constant in time value of $\langle n_i^2 \rangle$ (see Figure 7.8). This backs the "thermality" of the Mott phases that are joined by the inhomogeneous region, also suggests that the hypothetical steady deterioration of the METTS ensemble description quality does not happen in the homogenous phase.

Chapter 8

Afterword

This thesis provides insight into basic physics of complex ultracold atom systems, in static situations, quasistatic as well as fast dynamics. Below is a list of most important contributions provided by this thesis:

- We have verified that choice of boundary conditions may alter significantly the analysis of Quantum Phase Transitions by means of so-called Fidelity function. We have determined that extrapolation of QPT position from finite length systems is far easier if periodic boundary conditions are used. We had little success with extrapolating from the open chain data and identified that the reason was that Fidelity function is dominated by odd behaviour of the ground states close to the phase boundaries. Tracing out the border area by means of a reduced density matrix was determined not to be a reliable alternative.

- An useful tool for analysis of complex quantum system has been developed. We have performed the Fourier Transform directly on Matrix Product State representation of a wavepacket being evolved unitarily. It allowed us to extract the eigenstates most significantly contributing to the wavepacket. The method allows for identifying and describing of excitations in a physical process. We have tested this method on a quasiadiabatic evolution of an ultracold atom gas in a harmonic trap and identified the source of lack of adiabaticity during ramping up the lattice potential. Application of that method to the wavepacket created during the simulation of the modulation spectroscopy allowed for describing what excitations contribute to particular peaks in the absorption spectrum.

- Effects of higher Bloch bands in a static situation were successfully incorporated into the Bose-Hubbard Hamiltonian. The problem was approached by a recent method of substituting the ordinary Fock space with effective model whose Hilbert space consists of interacting ground

states. We have contributed to increasing the accuracy of determination of the coefficients of the effective model. We have applied this approach to the analysis of various relevant problems. A prime example is successful locating the absorption peak in spectrum from modulation spectroscopy simulation and reaching an agreement with the experiment.

- If the optical lattice potential changes rapidly, the wavefuction may not have sufficient time to adapt. In such a case new terms appear in the Multiband Bose-Hubbard Hamiltonian. Their inclusion allowed to show that preparing excited states of the optical lattice through lattice height as predicted in [134] is indeed possible. Moreover, the efficiency of such a process is two times higher than one could expect from ordinary MBH Hamiltonian. We have also shown, that high frequency excitation spectrum through modulation is much richer than the ordinary MBH model predicts.

- We have studied the phase diagram of the Spin-1 Bose-Hubbard model. We have determined the presence of the Bose-Glass phase if the disorder is imposed in chemical potential or in the spin-dependent interaction parameter. We have studied spin properties of the Bose-Glass phases.

- Nonzero temperature effects have to be studied and understood despite ultracold temperatures in the experiments. We have performed a real-time evolution of the many-body quantum system in nonzero temperature and were able to draw conclusions on the diffusion constant describing the thermal equilibration. We show that it depends weakly or not at all on the temperature of the gas (in ultracold regime in Mott insulator regime) and it depends linearly on the quantum tunneling amplitude.

Chapter 9

Appendices

9.1 Wannier functions for finite systems

The discrete lattice in which the Bose-Hubbard Hamiltonian is set is obtained by means of a tight-binding approximation applied to the second-quantized Hamiltonian describing a gas of ultracold atoms in 1D optical lattice potential under periodic boundary conditions:

$$H = -\frac{\hbar^2}{2m}\frac{d^2}{dx^2} + V(x), \tag{9.1}$$

where $V(x) = V_0 \sin^2(kx), k = \frac{2\pi}{\lambda}$. Introducing energy scale by $E_R = \frac{\hbar^2 k^2}{2m}$ and a unit length of $\frac{\lambda}{2\pi}$ one obtains a dimensionless form of the equation (9.1) which is:

$$H = -\frac{d^2}{dx^2} + s_0 \sin^2 x, \tag{9.2}$$

where $s_0 E_R = V_0$.

We now reconsider the construction of Wannier functions especially taking into account all the particularities due to the finiteness of the lattice. In the new units one solves the single particle, 1D Schrödingier equation associated with the Hamiltonian (9.2) with the periodic boundary condition $\phi(x) = \phi(x+L)$, where now the lattice length is $M = L\pi$, where K is a total number of sites in the lattice. Functions satisfying a Schrödinger equation with the above hamiltonian are Bloch functions. They are assumed to be normalised over a natural inner product in $\mathcal{H}^1 = L^2\left(\mathbb{S}^1\right)$, where $\mathbb{S}^1$ is a circle of length L. As the Hamiltonian is invariant by a translation by a single site, the Bloch functions are chosen as eigenfunctions of this rotation. Thus eigenvalues of R_θ are good quantum numbers — they are modulus 1 complex numbers $\exp(i\theta_n)$, where $\theta_n = \frac{2\pi n}{L}, n \in \{-\lfloor\frac{L}{2}\rfloor, \ldots, \lfloor\frac{L-1}{2}\rfloor\}$ are typically denoted as quasimomenta. For each value of θ_n one may find plenty of eigenvectors $|\phi^\alpha_{\theta_n}\rangle$ — they are grouped into a series of Bloch bands.

Bloch functions are mutually orthogonal: $\langle \phi^{\alpha}_{\theta_n} | \phi^{\beta}_{\theta_m} \rangle = \delta_{nm}\delta_{\alpha\beta}$. Here α, β denote a number of Bloch band. The goal is to define a family of mutually orthogonal functions, Wannier functions ψ^{α}_i, satisfying in particular orthogonality relations: $\langle \psi^{\alpha}_i | \psi^{\beta}_j \rangle = \delta_{ij}\delta_{\alpha\beta}$. Index i denotes number of site over which a Wannier function is localised, α denotes a Bloch band to which a Wannier function belongs (the idea is that Wannier function belonging to band α should be composed of Bloch functions from band α). We additionally request Wannier functions to be real.

If number of sites is odd, that is $2 \nmid N$, then except for θ_0 quasimomenta come in pairs: $\theta_n = -\theta_{-n}$, moreover if $\phi_{\theta_n}(x)$ is a Bloch function to a quasimomentum θ_n, then $\phi_{\theta_{-n}} = \overline{\phi_{\theta_n}}$. For N odd, also $\lfloor \frac{N-1}{2} \rfloor = \lfloor \frac{N}{2} \rfloor$, and thus:

$$w^{\alpha}_0(x) = \mathcal{N} \sum_{i=-\lfloor \frac{N}{2} \rfloor}^{\lfloor \frac{N}{2} \rfloor} v_i \phi_{\theta_i}(x) \tag{9.3}$$

is real provided $v_i = v_{-i}$ for α even. For α odd one uses $v_i = -v_{-i}$ and multiplies the above sum by an imaginary unit i.

The Wannier functions for even bands are constructed from Bloch functions as to maximize value of $w_n(0)$, while those for odd bands $w'_n(0)$ is maximized (and $w_n(0) = 0$). This maximization is performed by maximizing values of $w_0\alpha(0)$ and $w_0^{\alpha\prime}(0)$ respectively. This means that in the sum (9.3) a contribution given by a summand $v_i\phi_{\theta_i}(0)$ is maximized by choosing $v_i = \phi_{\theta_i}(0)^*/|\phi_{\theta_i}(0)|$ or $v_i = \phi'_{\theta_i}(0)^*/\phi'_{\theta_i}(0)|$. The $\mathcal{N}$ is a global normalization factor.

The Bose-Hubbard parameters are defined as follows:

$$J_{\alpha} = -\int_0^{L\pi} w^{\alpha}(x) \left(-\frac{d^2}{dx^2} + s_0 \sin^2(x) \right) w^{\alpha}((x+\pi) \mod L\pi) \mathrm{d}x \tag{9.4}$$

and

$$U^{\alpha\beta\gamma\delta} = -\int_0^{L\pi} w^{\alpha}(x) w^{\beta}(x) w^{\gamma}(x) w^{\delta}(x) \mathrm{d}x. \tag{9.5}$$

In separable optical lattice potentials the 3D Wannier function is a product of 1D Wannier functions:

$$W^{\vec{\alpha}}_{\vec{i}}(\vec{r}) = w^{\alpha_x}_{i_x}(x, s_x) w^{\alpha_y}_{i_y}(y, s_y) w^{\alpha_z}_{i_z}(z, s_z). \tag{9.6}$$

Figure 9.1 shows the tunnelling parameters and interaction parameter $U^{\alpha\alpha\alpha\alpha}$ calculated taking into account finite L effects. It is clear that for excited bands. Finite L effects are rather pronounced

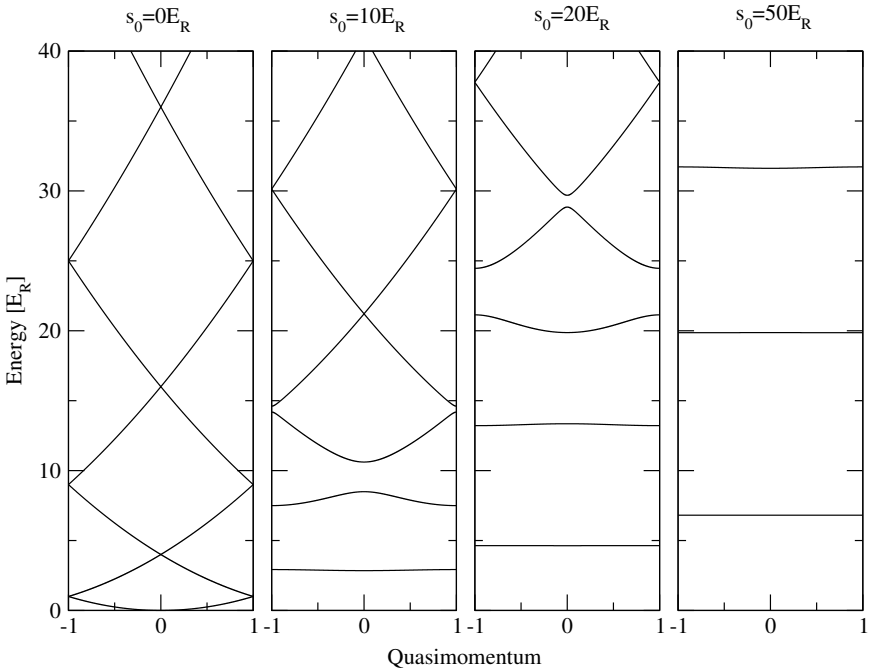

Figure 9.1: Bloch spectra for different lattice depths denoted above the graphs. The deeper the lattice potential, the more energy bands are almost completely flattened out (and energy band spacing becomes constant for confined bands — the potential well for low levels is well approximated by the harmonic oscillator).

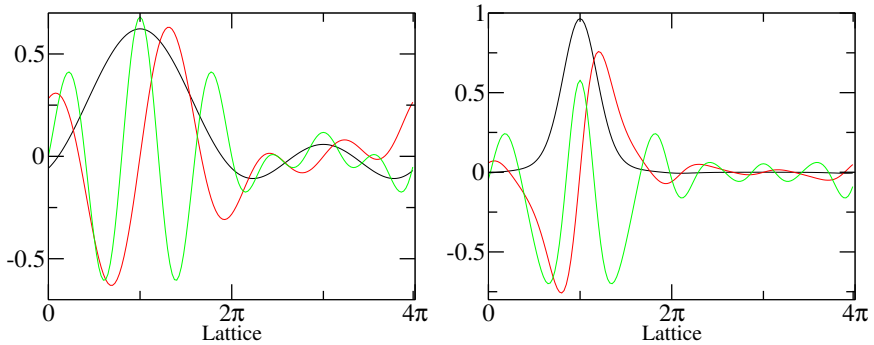

Figure 9.2: Exemplary Wannier functions for two lattice depths $s_0 = 0$ (left panel) and $s_0 = 10E_R$ (right panel). In these plots the lattice length is $L = 4$, ticks show positions of lattice sites.

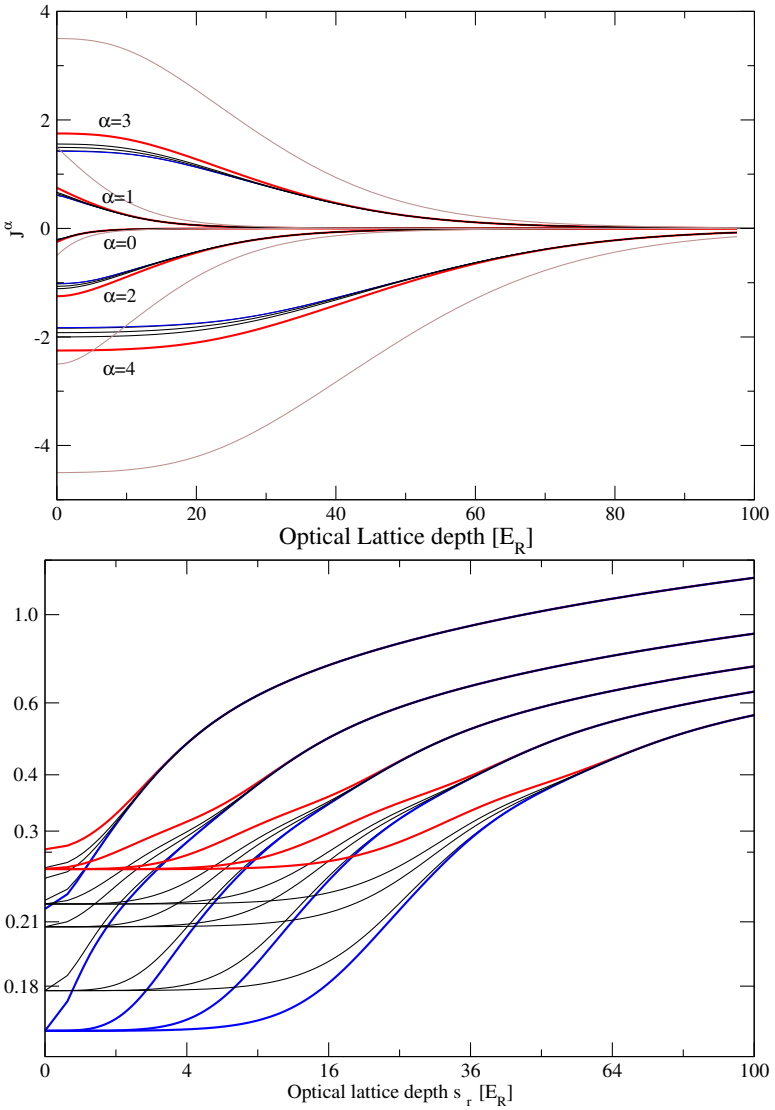

Figure 9.3: Top panel: tunnelling amplitudes J^α for first five Bloch bands: $\alpha = 0, \ldots, 4$ plotted for different lattice lengths L as a function of lattice depth s_r. Red curve shows tunnelling amplitudes for lattice length $L = 4$, blue for $L = 40$, while remaining blue curves show J^α for $L = 6, 8, 20$. Additionally, brown curves show the same for $L = 2$. One can see that values for $L = 20$ and $L = 40$ are almost indistinguishable in the plot, even for largest shown band number. Bottom panel: Parameters $U^{\alpha\alpha\alpha\alpha}$ for different lattice lengths L (values and colors identical as in the Figure in the top panel) and band index $\alpha = 0, \ldots, 4$. The higher the band index α the lower the values of $U^{\alpha\alpha\alpha\alpha}$.

A special case $s_0 = 0$

A general calculation of Wannier functions is performed by means of numerical methods, as solving for Bloch functions in a potential $V(x) = s_0 \sin^2 x$ is a nontrivial problem for which there are no closed form solutions except a special case $s_0 = 0$, and perhaps an asymptotic expansion for high-energy situation $\alpha \to \infty$. In the special case, when there is no lattice $s_0 = 0$ calculation of Bloch functions with a quasi momentum k is trivial: they are just $\exp(\frac{i}{\pi}k'x), k' = k + 2n$. This enables one to calculate Wannier functions for any band α and any lattice length $L \in \mathbb{N} \cup \{\infty\}$.

In the $L = \infty$ case, the general formula for a normalized Wannier function is:

$$w_{i=0}^{\alpha=n}(x) = \begin{cases} \frac{\sin((n+1)x)-\sin(nx)}{x\sqrt{\pi}} & \text{for } n \text{ even}, \\ \frac{\cos(nx)-\cos((n+1)x)}{x\sqrt{\pi}} & \text{for } n \text{ odd}. \end{cases} \tag{9.7}$$

Integration gives in particular that: $U^{0000} = \frac{2}{3\pi}$ and $U^{\alpha\alpha\alpha\alpha} = \frac{1}{2\pi}, \alpha > 0$. Moreover: $J^\alpha = -\frac{2(2\alpha+1)(-1)^\alpha}{\pi^2}$, as one may easily prove that $J^\alpha = \int_{-1}^{1} E^\alpha(k) \exp(ik\pi)\mathrm{d}k$, and more generally $J^\alpha_{|i'-j'|} = \int_{-1}^{1} E(k) \exp(i\pi k|i'-j'|\alpha)\mathrm{d}k$. The case of the finite L may be worked out analogously.

9.2 Derivation of additional terms in Hamiltonian present due to fast dynamics

The solution of the dynamical problem with time-dependent lattice depth $s = s(t), s(0) = s_0$ is described by the time-dependent wavefunction $\psi(t)$. In the numerical computation it is expressed in the basis generated by single particle modes $\mathcal{B}(t) = \{W_i^\alpha(\cdot, s(t))\}$. At time instant t' the expansion is performed in basis $\mathcal{B}(t')$. This basis spans basis function in real space functions. Here $W_i^\alpha(\cdot, s(t))$ is an appropriate dimensional Wannier function. For example for 3D separable optical potential it is

$$W_i^\alpha(\vec{r}, s) = w_i^{\alpha_x}(x, s_x) w_i^{\alpha_y}(y, s_y) w_i^{\alpha_z}(z, s_z). \tag{9.8}$$

For the 1D optical lattice (with a very tight transverse binding) we may assume for example:

$$W_i^\alpha(\vec{r}, s) = w_i^{\alpha_x}(x, s) H(y) H(z), \tag{9.9}$$

where H is an appropriate harmonic oscillator ground state.

Without any complication of notation we may assume that the time-dependence of the lattice is arbitrary: not necessarily through optical lattice depth alteration. Thus let us assume that s is some parameter describing alteration of the Wannier functions. For example if the lattice minima move periodically then $W_i^\alpha(s)(x) = W_i^\alpha(x - s), s(t) = s_m \cos \omega t$.

Just as shown in Section 1.2 using the basis $\mathcal{B}(t')$ leads to the MBH Hamiltonian (1.6). When $s = s(t)$ is time dependent so is the isometric basis transformation $\mathcal{U}(s(t))$ from the position representation to the lattice (Wannier functions) representation. Of course $\mathcal{H}_{MBH} = \mathcal{U}(s(t))\mathcal{H}_X\mathcal{U}^\dagger(s(t))$. Define via $\psi(t) = \mathcal{U}(s(t))\psi_X(t)$ (where $\psi_X(t)$ is the wavefunction in the position representation while $\psi(t)$ corresponds to the lattice representation). If the $\mathcal{U}(t)$ was in fact time independent, the dynamics of ψ would be governed by the (1.6). The proper new Hamiltonian in the time-dependent case, $\mathcal{H}_W$ is of the form:

$$\mathcal{H}_W = \mathcal{H} + i\hbar\left(\frac{d}{dt}\mathcal{U}(s(t))\right)\mathcal{U}^\dagger(s(t)) = \mathcal{H} + \mathcal{W}, \tag{9.10}$$

and the TDSE for $\psi(t)$: $i\hbar\partial_t\psi = \mathcal{H}_W\psi$.

The basis for the Hilbert space for a gas of N bosons consists of symmetrised (tensor) products of N single particle basis functions W_i^α. We denote such a basis for the N particle problem by $\mathcal{W}^N(s)$, the basis depends on the lattice depth by the value of s parameter through the set of single particle Wannier functions $\mathcal{W}(s) = \{W_i^\alpha(\cdot, s)\}_{i,\alpha}$.

Single particle states defined by Wannier functions and in the discrete lattice are enumerated by two indices α and i, from this point up to the end of the derivation, we introduce the multiindex $\iota = (\alpha, i)$ to simplify the notation.

Let us define a shortened notation. The lattice Fock state with occupation n_ι of mode ι will be denoted as $|\vec{n}_\mathcal{L}\rangle$. The corresponding state in the position representation for the lattice with height s will be abbreviated to: $|\vec{n}_X, s\rangle$. We always assume that $n_1 + \ldots n_\mathcal{L} = N$ (here, with slight abuse of the notation $\mathcal{L}$ denotes the total number of modes indexed by ι). The Hilbert space for the lattice system (in which the Bose-Hubbard Hamiltonian is usually expressed) has a time-independent basis (the Fock basis) $\mathcal{F}$. Action of the map $\mathcal{U}(s)$ from the continuous space with base $\mathcal{W}^N(s)$, to the Fock space with base $\mathcal{F}$ is rather trivial: in the chosen orthonormal bases it is the identity matrix at each time instant — it maps state $|\vec{n}_X, s(t)\rangle$ to a state $|\vec{n}_\mathcal{L}, s(t)\rangle$. The map is thus always an isometry (note that for 1D and 2D lattice it is only a partial isometry from a full continuous space; it the real space function in transverse directions if not defined by harmonic oscillator ground state, then the mapping is undefined). Despite the matrix elements of map $\mathcal{U}$ are constant, the map $s \to \mathcal{U}(s)$ as a function of s is not a constant function. Indeed the basis in which matrix of $\mathcal{U}$ is constant varies with s.

Using this notation we can express the map $\mathcal{U}$ as:

$$\mathcal{U}(s) = \sum_{\vec{n}} |\vec{m}_\mathcal{L}\rangle\langle\vec{m}_X, s|.$$

Now we expand the derivative of the $\mathcal{U}$ isometry as needed for Eq. 9.10. We use the fact that the basis of the Fock space $\mathcal{F}$ is time-independent,

contrary to single particle eigenfunctions in real space Hilbert space:

$$\left(\frac{d}{dt}\mathcal{U}(s(t))\right)|\psi\rangle_X = \sum_{\vec{m}} |\vec{m}_{\mathcal{L}}\rangle \left(\frac{d}{dt}\langle \vec{m}_X, s(t)|\right)|\psi\rangle_X.$$

Thus the $\mathcal{W}$ term is just:

$$\begin{aligned}\mathcal{W} &= i\hbar \sum_{\vec{n},\vec{m}} |\vec{m}_{\mathcal{L}}\rangle\langle \vec{n}_{\mathcal{L}}| \left(\frac{d}{dt}\langle \vec{m}_X, s(t)|\right)|\vec{n}_X, s(t)\rangle = \\ &= -i\hbar \sum_{\vec{n},\vec{m}} |\vec{m}_{\mathcal{L}}\rangle\langle \vec{n}_{\mathcal{L}}|\langle \vec{m}_X, s(t)| \left(\frac{d}{dt}|\vec{n}_X, s(t)\rangle\right). \end{aligned} \tag{9.11}$$

The relation which binds those $\vec{n}$ and $\vec{m}$ for which the summand may give a nonzero contribution to the above sum remains to be worked out as well as exact value of the summand. To do so, we expand the time derivative, by inserting an exact action of the symmetrization operator:

$$\begin{aligned}&\sqrt{N!n_1!n_2!\ldots n_{\iota_0}!}\frac{d}{dt}|\vec{n}_X, s(t)\rangle = \\ &\sum_{\pi\in S(N)} \frac{d}{dt}\left[W_1(x_{\pi(1)})W_1(x_{\pi(2)})\ldots W_1(x_{\pi(n_1)})\cdot\right. \\ &\left.\cdot W_2(x_{\pi(n_1+1)})\ldots W_2(x_{\pi(n_1+n_2)})\ldots W_{\iota_0}(x_{\pi(N)})\right] \\ &= \sum_{k=1}^{N}\sum_{\pi\in S(N)} \left[W_1(x_{\pi(1)})W_1(x_{\pi(2)})\ldots W_1(x_{\pi(n_1)})\cdot\right. \\ &\left.\cdot W_2(x_{\pi(n_1+1)})\ldots \dot{W}_\iota(x_{\pi(k)})\ldots W_{\iota_0}(x_{\pi(N)})\right] \end{aligned} \tag{9.12}$$

In the above line each of Wannier functions W_ι depends on J through $s(t)$. The formula is well-stated, because only a finite number of modes has nonzero occupation: for $\iota > \iota_0$ we have $n_\iota! = 1$ and no factors W_ι.

Next, we use the partition of unity $\sum_{\varkappa} |W_\varkappa\rangle\langle W_\varkappa|$, applying it to $\dot{W}_\iota$ we get:

$$\frac{d}{dt}W_\iota(x) = \sum_{\varkappa} T_\iota^\varkappa W_\varkappa(x), \tag{9.13}$$

where $T_\iota^\varkappa = \int W_\varkappa(x)\dot{W}_\iota(x)\mathrm{d}x$. Therefore, by combining together (9.11), (9.12) and (9.13) one obtains that the only $(\vec{n},\vec{m})$ giving nonzero contribution in (9.11) are those that correspond to changing the mode of only one particle from configuration $\vec{n}$ — the mode ι to $\varkappa$. Therefore:

$$\begin{cases} m_i = n_i & i \neq \iota, \varkappa \\ m_\iota = n_\iota - 1 & \\ m_\varkappa = n_\varkappa + 1 & \end{cases} \tag{9.14}$$

As $T^{\iota}_{\iota} = 0$ due to norm preservation, only $\iota \neq \varkappa$ terms contribute. Change of occupation is compatible with action of $a^{\dagger}_{\varkappa} a_{\iota}$ operator. We will show that also the numerical factor agrees. A mode to be differentiated (mode ι) may be chosen in (9.12) in n_{ι} ways, and:

$$\frac{n_{\iota}}{\sqrt{n_1! n_2! \ldots n_{\iota'}!}} = \frac{\sqrt{n_{\iota}(n_{\varkappa}+1)}}{\sqrt{n_1! \ldots (n_{\iota}-1)! \ldots (n_{\varkappa}+1)! \ldots n_{\iota'}!}}. \tag{9.15}$$

Thus from (9.11), (9.12) and (9.13):

$$\frac{d}{dt}|\vec{n}_X, s(t)\rangle = \sum_{\varkappa,\iota=1}^{\infty} T^{\varkappa}_{\iota} \sqrt{n_{\iota}(n_{\varkappa}+1)} |\vec{m}_X, s(t)\rangle. \tag{9.16}$$

Above $\vec{m}$ is assumed to satisfy relations (9.14). All in all, we obtain

$$\begin{aligned} \dot{\mathcal{U}}(t)\mathcal{U}^{\dagger}(t) = -\sum_{\iota,\varkappa} T^{\varkappa}_{\iota} |\vec{m}_{\mathcal{L}}\rangle\langle\vec{n}_{\mathcal{L}}| \sqrt{n_{\iota}(n_{\varkappa}+1)} = \\ = -\sum_{\iota,\varkappa} T^{\varkappa}_{\iota} a^{\dagger}_{\varkappa} a_{\iota}. \end{aligned} \tag{9.17}$$

We now go back to the original labeling by Bloch band number: $\iota = (\alpha, i), \varkappa = (\beta, j)$. We also specify the method how the lattice is modified s now denotes again the lattice depth which is time-dependent $s(t)$. Now $T^{\varkappa}_{\iota} = T^{\beta\alpha}_{j-i} = -T^{\alpha\beta}_{i-j}$. We obtain the form of $\mathcal{W}$ term used in the main article:

$$\begin{aligned} \mathcal{W} &= -i\hbar \sum_{\iota,\varkappa} T^{\alpha\beta}_{i-j} (a^{\alpha}_i)^{\dagger} a^{\beta}_j, \\ T^{\alpha\beta}_{i-j} &= \int \dot{W}^{\beta}_j(x) W^{\alpha}_i(x) \mathrm{d}^3 x. \end{aligned} \tag{9.18}$$

The term $T^{\varkappa}_{\iota}$ has to be worked out for the basis functions for the lattice in the appropriate dimension. In the 1D lattice, Wannier functions are of form (9.9), then: $T^{\varkappa}_{\iota} = \int \mathrm{d}y \mathrm{d}z H(y)^2 H(z)^2 \int \mathrm{d}x w^{\beta}_j(x) \dot{w}^{\alpha}_i(x)$. Due to normalization: $T^{\varkappa}_{\iota} = \int \mathrm{d}x w^{\beta}_j(x) \dot{w}^{\alpha}_i(x)$. For 3D lattice, from (9.8), we get: $T^{\varkappa}_{\iota} = \int \mathrm{d}x \mathrm{d}y \mathrm{d}z w^{\beta_x}_{j_x}(x) w^{\beta_y}_{j_y}(y) w^{\beta_z}_{j_z}(z) \frac{d}{dt} \left(w^{\alpha_x}_{i_x}(x) w^{\alpha_y}_{i_y}(y) w^{\alpha_z}_{i_z}(z) \right)$. Nonzero values may be obtained only if $i_x = j_x \wedge \alpha_x = \beta_x \wedge i_y = j_y \wedge \alpha_y = \beta_y$ or $i_y = j_y \wedge \alpha_y = \beta_y \wedge i_z = j_z \wedge \alpha_z = \beta_z$ or $i_z = j_z \wedge \alpha_z = \beta_z \wedge i_x = j_x \wedge \alpha_x = \beta_x$. Thus the $\mathcal{W}$ terms perform hopping of a particle in only one direction (reserving a possibility for the Bloch band change). The amplitude for hopping in direction $t \in \{x, y, z\}$ is: $\int \mathrm{d}t w^{\beta_t}_{j_t}(t) \dot{w}^{\alpha_t}_{i_t}(t)$.

If the lattice is defined by oscillatory movement of the potential minima, then the $\mathcal{W}$ has the form of (9.18), but the formula for the $T_{i-j}^{\alpha\beta}$ term is modified as:

$$T_{i-j}^{\alpha\beta} = \int \left(\frac{d}{dx} W_j^{\beta}(x) \right) W_i^{\alpha}(x) \mathrm{d}^3 x. \tag{9.19}$$

9.3 Excitations within $J = 0$ limit, EMO Hamiltonian

The Bose-Hubbard Hamiltonian (1.9) in $J \to 0$ limit has Fock states as eigenstates. Let us assume that inclusion of external potential reduces to inclusion of the site-dependent chemical potential μ_i to the Hamiltonian (1.9). In the case of external harmonic trapping, the eigenstates are as in Figure 3.2.

The energy of a Fock state is (here we switch to a more general Hamiltonian (4.6) which contains the BH Hamiltonian as a special case $U_n = U, J_{n_1,n_2} = J$):

$$E = \sum_{i=1}^{L} E_i(n_i), \quad E_i(n) = \frac{U_n}{2} n(n-1) - \mu_i n. \tag{9.20}$$

The excitation energy of moving a particle from site i to site j is thus:

$$\Delta E(n_i; n_j) = E_j(n_j + 1) - E_j(n_j) + E_i(n_i - 1) - E_i(n_i), \tag{9.21}$$

and all in all, disregarding local chemical potential influence,

$$\Delta E(n_i; n_j) = (n_j - n_i + 1)U_2 + \frac{3}{2}(n_i - n_j - 1)(n_i + n_j - 2)W, \tag{9.22}$$

where equality $U_n = U_2 - (n-2)W$ has been assumed. This property is well satisfied by gas of rubidium atoms, for values of n considered in this thesis ($n < 7$).

For the pure BH model we have that $W = 0$. If the excitation within the Mott Insulator takes place then $n_i = n_j$ and the excitation energy is $U_{BH} = U_2$. The excitation energy stemming from each Mott plateau (in Figs. 3.2 and 9.4 is different which is expected to create a split of the modulation spectroscopy spectrum of the excitation peaks.

9.4 Monte Carlo basis construction for multiband single-site problem

The single site multiband local Hamiltonian $\mathcal{H}_{loc.}$, consists just of a single particle and interaction term. Tunnelling term and interaction-induced density dependent tunnelling term are discarded as they couple different sites.

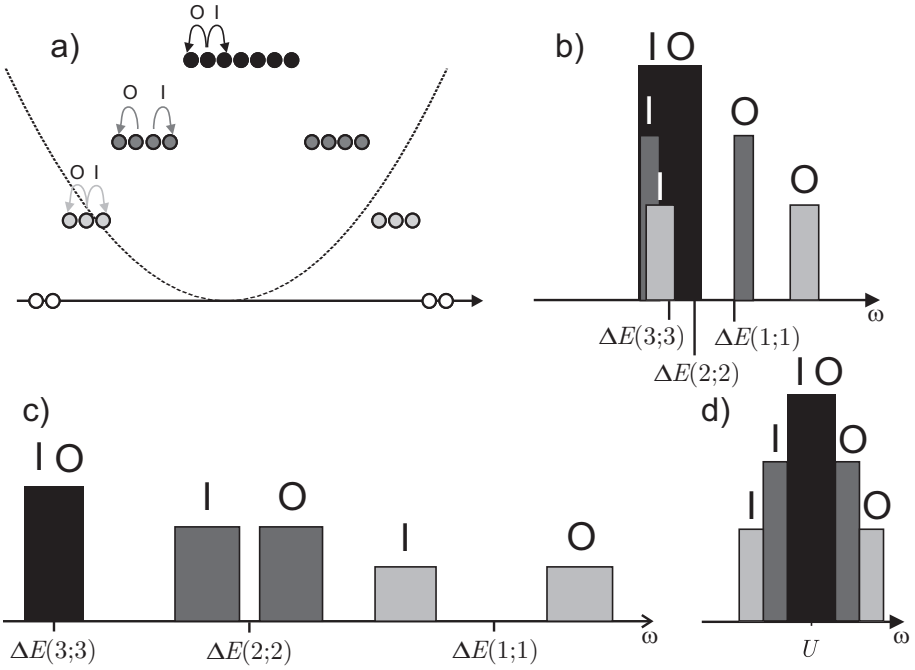

Figure 9.4: Effects of higher Bloch bands on absorption spectroscopy in the deep Mott (low J) regime, $s = 15,\ s_\perp = 40$. Panel (a) shows the well-known wedding cake structure with $n = 1, n = 2, n = 3$ Mott plateaus. Excitations within each plateau (colored respectively light gray, dark gray, black, for $n = 1, 2, 3$) have energies depending on the Mott plateau density and the trapping potential. Inward and Outward hopping lead to a splitting of the absorption structure, a partial splitting for moderate harmonic trap [(b), $\kappa = 0.001$] or a broad well resolved structure for a shallow trap [(c), $\kappa = 0.0001$] in contrast to the standard BH case (d). Image from [92].

In the Section 4.4 it was shown that it is desirable to choose a set $\mathcal{V}$ consisting of vectors that have largest "importance weight" Q defined in that section. Let us first introduce additional definitions.

By vectors reachable in k-th order perturbative expansion, we call those Fock states $|\psi_p\rangle$ for which $\langle\psi_0|H_U^k|\psi_p\rangle \neq 0$. In particular, a full basis can be generated with order $\lceil \frac{n}{2} \rceil$. Let us denote by $\mathcal{B}_k$ the set of vectors reachable in k-th order and unreachable in $k-1$-th order. The full variational basis of Fock states is $\mathcal{B} = \bigcup_k \mathcal{B}_k$, with $\mathcal{B}_k$ pairwise disjoint, and $\mathcal{B}_k = \emptyset,\ \text{for } k > \lceil \frac{n}{2} \rceil$.

For vectors $\psi \in \mathcal{B}_1$ we define the perturbative importance weights

$$f_1(\psi) = \ln \frac{|\langle\psi_0|\hat{H}_{loc}|\psi\rangle|}{E_{|\psi\rangle} - E_{|\psi_0\rangle}}. \tag{9.23}$$

Vectors $\psi \in \mathcal{B}_k$, for $k > 2$ may be reached using different chains of intermediate states $\psi_i \in \mathcal{B}_i, \langle\psi_i|\mathcal{H}|\psi_{i-1}\rangle \neq 0$. Hence the function f_k for

vectors from $\mathcal{B}_k$ shall be defined as follows

$$f_2(\psi) = \ln \sup_{|\psi_1\rangle \in \mathcal{B}_1} \frac{|\langle\psi_0|\hat{H}_{loc}|\psi_1\rangle\langle\psi_1|\hat{H}_{loc}|\psi\rangle|}{(E_{|\psi\rangle} - E_{|\psi_0\rangle})(E_{|\psi_1\rangle} - E_{|\psi_0\rangle})}. \tag{9.24}$$

$$g_k(\mathcal{V}) = \ln \frac{|\langle\psi_0|\hat{H}_{loc}|\psi_1\rangle\langle\psi_1|\hat{H}_{loc}|\psi_2\rangle| \ldots \langle\psi_{k-1}|\hat{H}_{loc}|\psi\rangle|}{(E_{|\psi\rangle} - E_{|\psi_0\rangle})(E_{|\psi_{k-1}\rangle} - E_{|\psi_0\rangle}) \ldots (E_{|\psi_1\rangle} - E_{|\psi_0\rangle})},$$
$$f_k(\psi) = \sup_{|\psi_1\rangle \in \mathcal{B}_1, \ldots, |\psi_{k-1}\rangle \in \mathcal{B}_{k-1}} g_k(\mathcal{V}). \tag{9.25}$$

The function f_k does inherit spirit of perturbative expansion, still it is not the full, most general perturbative expansion. In our considerations we have restricted ourselves to using basis vectors from sets $\mathcal{B}_1$ and $\mathcal{B}_2$ only for which we have encountered no zero in denominator problem.

The Metropolis algorithm is used to generate an ensemble of points x_n which importance is weighted by a function $f(x_n)$. Typically x_n are "states" and $f(x_n) = \exp(-\beta\text{"energy"})$ and the ensemble is thermal ensemble with inverse temperature β. To use this algorithm a modification procedure of the state x_n should be available. If the local update yields a new state x'_{n+1} then this is accepted ($x_{n+1} := x'_{n+1}$) if $f(x'_{n+1}) < f(x_n)$ otherwise it is accepted with probability $p = f(x_n)/f(x'_{n+1})$) and rejected ($x_{n+1} := x_n$) with probability $1 - p$.

In the Monte Carlo set $\mathcal{V} \subset \mathcal{B}_k$ generation the states are sequences $x = (\psi_1, \psi_2, \ldots, \psi_k)$. The weight function is $f = g_k$. The update procedure goes as follows: first we choose at random a Fock state $|\psi_l\rangle \in x$ to be updated. With equal probability, we update one or two particles of $|\psi_l\rangle$. One particle update is done according to $|\psi_l\rangle \to \hat{a}_{(i_x,i_y,i_z)}\hat{a}^\dagger_{(i_x,i'_y,i_z)}|\psi_l\rangle, i_y \equiv i'_y (\mathrm{mod}\ 2)$, while two-particle update is: $|\psi_l\rangle \to \hat{a}_{(i_x,i_y,i_z)}\hat{a}_{(j_x,j_y,j_z)}\hat{a}^\dagger_{(i_x,i'_y,i_z)}\hat{a}^\dagger_{(j_x,j'_y,j_z)}|\psi_l\rangle$ $i_y + j_y \equiv i'_y + j'_y (\mathrm{mod}\ 2)$. These updates preserve the total parity of the state. All vectors are normalized. Direction y is not special in any way: with equal probability any of x, y, z is chosen. After the update a proposition $\mathcal{V}'$ is prepared. We automatically reject updates for which $|\psi_l\rangle \notin \mathcal{B}_l$. If that is not the case, the acceptance probability is determined as in Metropolis algorithm: it is given by $\min\{1, \exp[\beta(g_k(\mathcal{V}') - g_k(\mathcal{V}))]\}$. The inverse temperature β is tuned to optimize sampling efficiency — we choose it by requiring the acceptance rate to be close to 0.3. After a successful update, the last element of the tuple $\mathcal{V}'$, state $|\psi_k\rangle$ is accepted into the solution set if its perturbative importance $g_k(\mathcal{V})$ is in the K lowest values recorded so far. The accepted vector $|\psi_k\rangle$ is memorised as well as the importance value $g_k(\mathcal{V}')$. If $|\psi_k\rangle$ had been generated before, the memorised value of g_k is updated (only if the new value of larger than the old one). If, in a subsequent few thousand sweeps (empirical value), no vector makes it into the solution set, nor g_k values are updated, then the procedure is restarted. The starting point is always

the low energy configuration. Altogether, we make 2×10^9 MC sweeps to generate basis of size 40000 (as used for the results presented in the main part of the paper).

If all Bloch bands were included, then the set of Fock states would be infinite. On the other hand, only a finite number of them could satisfy the inequality: $g_k > \varepsilon$. The values of g_k for the remaining states are very close to 0, and a singularity in density of states $\frac{\partial g_k}{\partial \vec{n}}$ arises. Logarithm is used to "smoothen" this singularity for numerical purposes. It does not affect the ordering, as ln is increasing injection.

9.5 Projection of METTS vector

The key requirement for the METTS algorithm used intensively in Section 7 is the ability to be able to perform the projective measurement in the computational basis. That is if $\{|e_i\rangle\}_i$ is the basis, then one should be able given a METTS vector $|\psi\rangle$ to pick randomly a basis vector $|e_i\rangle$ with probability $|\langle e_i|\psi\rangle|^2$. The METTS algorithm discussed in Section 7 has been implemented using the MPS ansatz (see Section 1.2). The projection may be performed using explicitly the form of the MPS vector (1.20), that is tensors λ and Γ in particular. For the Bose-Hubbard Hamiltonian (1.9), and the computational basis consisting of the Fock vectors: $|n_1, \ldots, n_L\rangle$, the projection is performed by determining the numbers n_i starting from n_1 and moving to the right up to n_L. At step k the so far projected vector has the form $|f_k\rangle = |n_1, n_2, \ldots, n_{k-1}\rangle|\psi_k\rangle$, where $|\psi_k\rangle$ is such that $|\langle f_k|\psi\rangle|$ is maximal. Knowing the $|f_k\rangle$ (for $k = 1$ it is just ψ) one may first compute the probabilities: $p_i = \langle\psi|(|n_1, n_2, \ldots, n_{k-1}, i\rangle \otimes |\psi^i_{k+1}\rangle)$, for maximal $(\langle n_1, n_2, \ldots, n_{k-1}, i|\otimes\langle\psi^i_{k+1}|)|\psi\rangle$. Finally one chooses $n_k = i$ with probability p_i and sets $|f_{k+1}\rangle = |n_1, n_2, \ldots, n_{k-1}, i\rangle|\psi^i_{k+1}\rangle$. The sought after projection result is $|f_{L+1}\rangle$.

Bibliography

[1]C. Pethick and H. Smith (Cambridge university press, 2002).

[2]A. Griffin, D. W. Snoke, and S. Stringari (Cambridge University Press, 1996).

[3]I. Bloch, J. Dalibard, and W. Zwerger, Reviews of Modern Physics **80**, 885 (2008).

[4]M. Lewenstein, A. Sanpera, and V. Ahufinger (Oxford University Press, 2012).

[5]C. C. Bradley, C. A. Sackett, J. J. Tollett, and R. G. Hulet, Physical Review Letters **75**, 1687–1690 (1995).

[6]K. B. Davis, M.-O. Mewes, M. R. v. Andrews, N. J. Van Druten, D. S. Durfee, D. M. Kurn, and W. Ketterle, Physical Review Letters **75**, 3969 (1995).

[7]M. Greiner, O. Mandel, T. Esslinger, T. W. Hänsch, and I. Bloch, Nature (London) **415**, 39 (2002).

[8]U. Bissbort and W. Hofstetter, Europhysics Letters **86**, 50007 (2009).

[9]B. Damski, J. Zakrzewski, L. Santos, P. Zoller, and M. Lewenstein, Physical Review Letters **91**, 080403 (2003).

[10]L. Fallani, J. E. Lye, V. Guarrera, C. Fort, and M. Inguscio, Physical Review Letters **98**, 130404 (2007).

[11]L. Sanchez-Palencia and M. Lewenstein, Nature Physics **6**, 87–95 (2010).

[12]M.-S. Chang et al., Physical Review Letters **92**, 140403 (2004).

[13]L.-M. Duan, E. Demler, and M. D. Lukin, Physical Review Letters **91**, 090402 (2003).

[14]T.-L. Ho, Physical Review Letters **81**, 742–745 (1998).

[15]Y. Kawaguchi and M. Ueda, Physics Reports **520**, 253–381 (2012).

[16]N. N. Klausen, J. L. Bohn, and C. H. Greene, Physical Review A **64**, 053602 (2001).

[17]M. A. Cazalilla and M. Rigol, New Journal of Physics **12**, 055006 (2010).

[18]C. Kollath, A. M. Läuchli, and E. Altman, Physical Review Letters **98**, 180601 (2007).

[19]M. Rigol, V. Dunjko, and M. Olshanii, Nature **452**, 854–858 (2008).

[20]A. S. Sørensen, E. Demler, and M. D. Lukin, Physical Review Letters **94**, 086803 (2005).

[21]M. Daghofer and M. Haque, Physics **6**, 49 (2013).

[22]J. Dalibard, F. Gerbier, G. Juzeli ūnas, and P. Öhberg, Reviews of Modern Physics **83**, 1523–1543 (2011).

[23]L. Cailletet, Science, 51–52 (1885).

[24]J. Dewar, Proceedings of the Royal Society of London **63**, 256–258 (1898).

[25]H. Kamerlingh Onnes, Koninklijke Nederlandse Akademie van Weteschappen Proceedings Series B Physical Sciences **11**, 168–185 (1908).

[26]J. F. Allen and A. D. Misener, Nature **141**, 75 (1938).

[27]D. J. Wineland, R. E. Drullinger, and F. L. Walls, Physical Review Letters **40**, 1639–1642 (1978).

[28]M. H. Anderson, J. R. Ensher, M. R. Matthews, C. E. Wieman, and E. A. Cornell, science **269**, 198–201 (1995).

[29]H. Friedrich (Springer, 2010).

[30]R. Grimm, M. Weidemuller, and Y. B. Ovchinnikov, Advances In Atomic Molecular, and Optical Physics **42**, 95 (2000).

[31]J. J. Sakurai and S. F. Tuan, Vol. 104 (Addison-Wesley Reading (Mass.), 1994).

[32]K. Huang and C. N. Yang, Physical Review **105**, 767 (1957).

[33]T. Busch, B.-G. Englert, K. Rzażewski, and M. Wilkens, Foundations of Physics **28**, 549–559 (1998).

[34]I. Reichenbach, A. Silberfarb, R. Stock, and I. H. Deutsch, Physical Review A **74**, 042724 (2006).

[35]Z. Idziaszek and T. Calarco, Physical Review Letters **96**, 013201 (2006).

[36]D. Jaksch, C. Bruder, J. I. Cirac, C. W. Gardiner, and P. Zoller, Physical Review Letters **81**, 3108–3111 (1998).

[37]M. Maik, P. Hauke, O. Dutta, M. Lewenstein, and J. Zakrzewski, New Journal of Physics **15**, 113041 (2013).

[38]D.-S. Lühmann, O. Jürgensen, and K. Sengstock, New Journal of Physics **14**, 033021 (2012).

[39]O. Dutta, M. Gajda, P. Hauke, M. Lewenstein, D.-S. Lühmann, B. A. Malomed, T. Sowiński, and J. Zakrzewski, arXiv preprint 1406.0181 (2014).

[40]P. Johnson, E. Tiesinga, J. Porto, and C. Williams, New Journal of Physics **11**, 093022 (2009).

[41]A. Mering and M. Fleischhauer, Physical Review A **83**, 063630 (2011).

[42]G. I. Taylor, Royal Society of London Proceedings Series A **145**, 362–387 (1934).

[43]P. W. Anderson, Physical Review **109**, 1492 (1958).

[44]T. Brandes and S. Kettemann, Vol. 630 (Springer, 2003).

[45]E. Abrahams, Vol. 24, 12-13 (World Scientific, 2010).

[46]M. Mézard, G. Parisi, and M. A. Virasoro, Vol. 9 (World scientific Singapore, 1987).

[47]D. Stauffer and A. Aharony (Taylor and Francis, 1994).

[48]H.-J. Stöckmann (Cambridge University Press, 2007).

[49]G. Casati and B. Chirikov (Cambridge University Press, 2006).

[50]P. Horak, J.-Y. Courtois, and G. Grynberg, Physical Review A **58**, 3953–3962 (1998).

[51]D. Boiron, C. Mennerat-Robilliard, J.-M. Fournier, L. Guidoni, C. Salomon, and G. Grynberg, English, The European Physical Journal D - Atomic, Molecular, Optical and Plasma Physics **7**, 373–377 (1999).

[52]R. Roth and K. Burnett, Physical Review A **67**, 031602 (2003).

[53]R. B. Diener, G. A. Georgakis, J. Zhong, M. Raizen, and Q. Niu, Physical Review A **64**, 033416 (2001).

[54]U. Gavish and Y. Castin, Physical Review Letters **95**, 020401 (2005).

[55]P. Massignan and Y. Castin, Physical Review A **74**, 013616 (2006).

[56]H. Gimperlein, S. Wessel, J. Schmiedmayer, and L. Santos, Physical Review Letters **95**, 170401 (2005).

[57]C. Chin, R. Grimm, P. Julienne, and E. Tiesinga, Reviews of Modern Physics **82**, 1225 (2010).

[58]G. Roux, T. Barthel, I. McCulloch, C. Kollath, U. Schollwöck, and T. Giamarchi, Physical Review A **78**, 023628 (2008).

[59]A. M. Rey, K. Burnett, R. Roth, M. Edwards, C. J. Williams, and C. W. Clark, Journal of Physics B: Atomic, Molecular and Optical Physics **36**, 825 (2003).

[60]D. Van Oosten, P. Van der Straten, and H. T. C. Stoof, Physical Review A **63**, 053601 (2001).

[61]J. K. Freericks and H. Monien, Physical Review B **53**, 2691 (1996).

[62]W. Krauth, Physical Review B **44**, 9772–9775 (1991).

[63]F. Alet, S. Wessel, and M. Troyer, Physical Review E **71**, 036706 (2005).

[64]S. Wessel, F. Alet, M. Troyer, and G. G. Batrouni, Physical Review A **70**, 053615 (2004).

[65]B. Bauer et al., Journal of Statistical Mechanics: Theory and Experiment **2011**, P05001 (2011).

[66]D. Perez-Garcia, F. Verstraete, M. M. Wolf, and J. I. Cirac, arXiv preprint quant-ph/0608197 (2006).

[67]J. Eisert, M. Cramer, and M. B. Plenio, Reviews of Modern Physics **82**, 277–306 (2010).

[68]M. Fannes, B. Nachtergaele, and R. F. Werner, Europhysics Letters **10**, 633 (1989).

[69]G. Vidal, J. I. Latorre, E. Rico, and A. Kitaev, Physical Review Letters **90**, 227902 (2003).

[70]M. B. Hastings, Journal of Statistical Mechanics: Theory and Experiment **2007**, P08024 (2007).

[71]A. Ekert and P. L. Knight, American Journal of Physics **63**, 415–423 (1995).

[72]Y.-Y. Shi, L.-M. Duan, and G. Vidal, Physical Review A **74**, 022320 (2006).

[73]G. Vidal, Physical Review Letters **93**, 040502 (2004).

[74]D. Gross, S. T. Flammia, and J. Eisert, Physical Review Letters **102**, 190501 (2009).

[75]J. Haegeman, T. J. Osborne, and F. Verstraete, Physical Review B **88**, 075133 (2013).

[76]U. Schollwöck, Annals of Physics **326**, 96–192 (2011).

[77]A. J. Daley, C. Kollath, U. Schollwöck, and G. Vidal, Journal of Statistical Mechanics: Theory and Experiment, P04005 (2004).

[78]S. R. White and A. E. Feiguin, Physical Review Letters **93**, 076401 (2004).

[79]M. L. Wall and L. D. Carr, *Open Source TEBD* (2009).

[80]M. P. A. Fisher et al., Physical Review B **40**, 546–570 (1989).

[81]T. D. Kühner and H. Monien, Physical Review B **58**, R14741–R14744 (1998).

[82]D. B. M. Dickerscheid, U. Al Khawaja, D. van Oosten, and H. T. C. Stoof, Physical Review A **71**, 043604 (2005).

[83]A. J. Leggett, Reviews of Modern Physics **71**, S318–S323 (1999).

[84]E. L. Pollock and D. M. Ceperley, Physical Review B **36**, 8343–8352 (1987).

[85]J. Carrasquilla, F. Becca, A. Trombettoni, and M. Fabrizio, Physical Review B **81**, 195129 (2010).

[86]L. Pollet, N. V. Prokofev, B. V. Svistunov, and M. Troyer, Physical Review Letters **103**, 140402 (2009).

[87]G. G. Batrouni, R. T. Scalettar, and A. P. Zimanyi, G. T.and Kampf, Physical Review Letters **74**, 2527 (1995).

[88]J. K. Freericks and H. Monien, Europhysics Letters **26**, 545 (1994).

[89]A. Kauch, K. Byczuk, and D. Vollhardt, Physical Review B **85**, 205115 (2012).

[90]T. P. Polak and T. K. Kopeć, Physical Review B **76**, 094503 (2007).

[91]J. Zakrzewski and D. Delande, Proceedings of LFCTN 7th international summer school and conference, Vol. 1076, 1 (AIP Publishing, 2008), pp. 292–300.

[92]M. Łącki, D. Delande, and J. Zakrzewski, New Journal of Physics **15**, 013062 (2013).

[93]M. Łącki, B. Damski, and J. Zakrzewski, Physical Review A **89**, 033625 (2014).

[94]S.-J. Gu, International Journal of Modern Physics B **24**, 4371–4458 (2010).

[95]P. W. Anderson, Physical Review Letters **18**, 1049–1051 (1967).

[96]H. Quan, Z Song, X. Liu, P Zanardi, and C. Sun, Physical Review Letters **96**, 140604 (2006).

[97]A. F. Albuquerque, F. Alet, C. Sire, and S. Capponi, Physical Review B **81**, 064418 (2010).

[98]V. Gritsev and A. Polkovnikov, in *Understanding in Quantum Phase Transitions* edited by L. Carr (Taylor & Francis, Boca Raton, 2010); arXiv:0910.3692.

[99]M. M. Rams and B. Damski, Physical Review Letters **106**, 055701 (2011).

[100]H.-Q. Zhou, J.-H. Zhao, and B. Li, J. Phys. A **41**, 492002 (2008).

[101]M. M. Rams and B. Damski, Physical Review A **84**, 032324 (2011).

[102]R. V. Pai, R. Pandit, H. R. Krishnamurthy, and S. Ramasesha, Phys. Rev. Lett. **76**, 2937 (1996).

[103]V. F. Elesin, V. A. Kashurnikov, and L. A. Openov, JETP letters **60**, 177–177 (1994).

[104]N. Elstner and H. Monien, arXiv preprint cond-mat/9905367 (1999).

[105]V. A. Kashurnikov, A. V. Krasavin, and B. V. Svistunov, JETP Letters **64**, 99 (1996).

[106]V. A. Kashurnikov and B. V. Svistunov, Physical Review B **53**, 11776 (1996).

[107]T. D. Kühner, S. R. White, and H. Monien, Physical Review B **61**, 12474–12489 (2000).

[108]R. V. Pai, R. Pandit, H. R. Krishnamurthy, and S. Ramasesha, Physical Review Letters **76**, 2937 (1996).

[109]S. Rapsch, U. Schollwöck, and W. Zwerger, Europhysics Letters **46**, 559 (1999).

[110]P. Buonsante and A. Vezzani, Physical Review Letters **98**, 110601 (2007).

[111]J. Carrasquilla, S. R. Manmana, and M. Rigol, Physical Review A **87**, 043606 (2013).

[112]P. Pippan, S. R. White, and H. G. Evertz, Physical Review B **81**, 081103 (2010).

[113]F. Verstraete, D. Porras, and J. I. Cirac, arXiv preprint cond-mat/0404706 (2004).

[114]M. Vekić and S. R. White, Physical Review Letters **71**, 4283–4286 (1993).

[115]M. Stoudenmire, http://itensor.org/docs.cgi?page=periodic (2014).

[116]M. M. Rams and B. Damski, Physical Review A **84**, 032324 (2011).

[117]B. Damski, **87**, 052131 (2013).

[118]H.-Q. Zhou, J.-H. Zhao, and B. Li, Journal of Physics A: Mathematical and Theoretical **41**, 492002 (2008).

[119]M. Łącki, D. Delande, and J. Zakrzewski, Physical Review A **86**, 013602 (2012).

[120]M. Łącki, D. Delande, and J. Zakrzewski, Acta Physica Polonica A **120**, A–178 (2011).

[121]J.-F. Schaff, P. Capuzzi, G. Labeyrie, and P. Vignolo, New Journal of Physics **13**, 113017 (2011).

[122]J. Zakrzewski and D. Delande, Physical Review A **80**, 013602 (2009).

[123]P. E. Dargel, A. Wöllert, A. Honecker, I. P. McCulloch, U. Schollwöck, and T. Pruschke, Physical Review B **85**, 205119 (2012).

[124]S. R. White, Physical Review Letters **69**, 2863–2866 (1992).

[125]M. Born and V. Fock, Zeitschrift für Physik **51**, 165–180 (1928).

[126]F. Gerbier, A. Widera, S. Fölling, O. Mandel, T. Gericke, and I. Bloch, Physical Review A **72**, 053606 (2005).

[127]F. Gerbier, Physical Review Letters **99**, 120405 (2007).

[128]C. Kollath, A. Iucci, et al., Physical Review Letters **97**, 50402 (2006).

[129]T. Stöferle, H. Moritz, C. Schori, M. Köhl, and T. Esslinger, Physical Review Letters **92**, 130403 (2004).

[130]J. Major, M. Łącki, and J. Zakrzewski, Physical Review A **89**, 043626 (2014).

[131]T. Sowiński, Physical Review Letters **108**, 165301 (2012).

[132]G. Vidal, Physical Review Letters **99**, 220405 (2007).

[133]J.-W. Huo, F.-C. Zhang, W. Chen, M Troyer, and U Schollwöck, Physical Review A **84**, 043608 (2011).

[134]M. Łącki and J. Zakrzewski, Physical Review Letters **110**, 065301 (2013).

[135]H. Pichler, J. Schachenmayer, A. J. Daley, and P. Zoller, Physical Review A **87**, 033606 (2013).

[136]A. Eckardt, C. Weiss, and M. Holthaus, Physical Review Letters **95**, 260404 (2005).

[137]M. Łącki et al., Physical Review A **83**, 013605 (2011).

[138]S. Paganelli, M Łącki, V. Ahufinger, J. Zakrzewski, and A. Sanpera, Journal of Low Temperature Physics **165**, 227–238 (2011).

[139]A. Imambekov, M. Lukin, and E. Demler, Physical Review A **68**, 063602 (2003).

[140]T. Ohmi and K. Machida, Journal of the Physical Society of Japan **67**, 1822–1825 (1998).

[141]C. K. Law, H. Pu, and N. P. Bigelow, Physical Review Letters **81**, 5257–5261 (1998).

[142]M. Koashi and M. Ueda, Physical Review Letters **84**, 1066–1069 (2000).

[143]S. Tsuchiya, S. Kurihara, and T. Kimura, Physical Review A **70**, 043628 (2004).

[144]E. Demler and F. Zhou, Physical Review Letters **88**, 163001 (2002).

[145]T. Kimura, S. Tsuchiya, and S. Kurihara, Physical Review Letters **94**, 110403 (2005).

[146]G. G. Batrouni, V. G. Rousseau, and R. T. Scalettar, Physical Review Letters **102**, 140402 (2009).

[147]P. O. Fedichev, Y. Kagan, G. V. Shlyapnikov, and J. T. M. Walraven, Physical Review Letters **77**, 2913–2916 (1996).

[148]J. L. Bohn and P. S. Julienne, Physical Review A **56**, 1486–1491 (1997).

[149]M. Theis, G. Thalhammer, K. Winkler, M. Hellwig, G. Ruff, R. Grimm, and J. H. Denschlag, Physical Review Letters **93**, 123001 (2004).

[150]D. J. Papoular, G. V. Shlyapnikov, and J. Dalibard, Physical Review A **81**, 041603 (2010).

[151]T. M. Hanna, E. Tiesinga, and P. S. Julienne, New Journal of Physics **12**, 083031 (2010).

[152]S. V. Alyabyshev and R. V. Krems, Physical Review A **80**, 033419 (2009).

[153]M. Rigol, Physical Review Letters **103**, 100403 (2009).

[154]J. Berges, S. Borsányi, and C. Wetterich, Physical Review Letters **93**, 142002 (2004).

[155]M. C. Bañuls, J. I. Cirac, and M. B. Hastings, Physical Review Letters **106**, 050405 (2011).

[156]S. R. White, Physical Review Letters **102**, 190601 (2009).

[157]C. Schroll, F. Marquardt, and C. Bruder, Physical Review A **70**, 053609 (2004).

[158]B. DeMarco, C. Lannert, S. Vishveshwara, and T.-C. Wei, Physical Review A **71**, 063601 (2005).

[159]M. Rigol, Physical Review A **72**, 063607 (2005).

[160]R. J. Bursill, T. Xiang, and G. A. Gehring, Journal of Physics: Condensed Matter **8**, L583 (1996).

[161]L. I. Plimak, M. K. Olsen, and M. Fleischhauer, Physical Review A **70**, 013611 (2004).

[162]T.-L. Ho and Q. Zhou, Physical Review Letters **99**, 120404 (2007).

[163]L. Pollet, C. Kollath, K. Van Houcke, and M. Troyer, New Journal of Physics **10**, 065001 (2008).

[164]M. Kollar, F. A. Wolf, and M. Eckstein, Physical Review B **84**, 054304 (2011).

[165]T. Barthel and U. Schollwöck, Physical Review Letters **100**, 100601 (2008).

[166]A. Polkovnikov, K. Sengupta, A. Silva, and M. Vengalattore, Reviews of Modern Physics **83**, 863 (2011).

[167]N. V. Prokofev, B. V. Svistunov, and I. S. Tupitsyn, Journal of Experimental and Theoretical Physics **87**, 310–321 (1998).

[168]U. Schollwöck, Physics **2**, 39 (2009).

[169]B Capogrosso-Sansone, N. Prokof'ev, and B. Svistunov, Physical Review B **75**, 134302 (2007).